What Matters for the Charge Transport of Two-Dimensional Perovskites?

Yixin Zhang [a,b], Mojtaba Abdi-Jalebi [c], Bryon W. Larson [d,], Fei Zhang [a,b,*]*

Y. X. Zhang, Prof. F. Zhang

School of Chemical Engineering and Technology, Tianjin University, Tianjin, 300072, China.

E-mail: fei_zhang@tju.edu.cn

Y. X. Zhang, Prof. F. Zhang

Collaborative Innovation Center of Chemical Science and Engineering (Tianjin), Tianjin, 300072, China.

Prof. M. A. Jalebi,

Institute for Materials Discovery, University College London, London, WC1E 7JE, UK

Dr. B. W. Larson

Chemistry and Nanoscience Center, National Renewable Energy Laboratory, Golden, CO 80401, USA.

E-mail: Bryon.Larson@nrel.gov

Keywords: 2D perovskites, interlayer cations, structure, charge transport

Compared to three-dimensional (3D) perovskites, two-dimensional (2D) perovskites exhibit excellent stability, structural diversity, and tunable bandgaps, making them highly promising for applications in solar cells, light-emitting diodes and photodetectors. However, the trade-off for worse charge transport is a critical issue that needs to be addressed. This comprehensive review first discusses the structure of 3D and 2D metal halide perovskites, then summarizes the significant factors influencing charge transport in detail and provides a brief overview of the testing methods. Subsequently, various strategies to improve the charge transport are presented, including tuning A'-site organic spacer cations, A-site cations, B-site metal cations, and X-site halide ions. Finally, an outlook on the future development of improving the 2D perovskites' charge transport is discussed.

1. Introduction

Halide perovskites possess remarkable optical and electrical properties, including a high absorption coefficient, high carrier mobility, long carrier diffusion length, and excellent defect tolerance,[1] widely used in the research and application of optoelectronic devices such as perovskite solar cells (PSCs),[2] light-emitting diodes (LEDs),[3] photodetectors (PDs),[4] field-effect transistors (FETs),[5] and lasers.[6] Particularly in the field of PSCs, as of 2023, the power conversion efficiency (PCE) of single-junction cells has surpassed 26%,[7] unprecedented among all thin-film photovoltaic (PV) technologies.

However, three-dimensional (3D) perovskite instability under environmental conditions remains a significant obstacle to its commercialization in various application areas.[8] Due to a soft ionic lattice, the organic cations within the structure, such as methylammonium (MA^+) and formamidinium (FA^+), interact with the inorganic framework via weak non-covalent bonds, making them susceptible to detachment from the crystalline structure under the influence of water.[9] Moreover, the transformation of additional halogen atoms into acid halides under the influence of water can also accelerate this decomposition process.[10] To facilitate the commercialization of perovskite materials, addressing the issue of operational durability is of utmost importance and should be tackled as soon as possible.[11] Researchers have employed various strategies, including compositional engineering,[12] interface engineering,[13] additive engineering,[14] and encapsulation techniques,[15] to ensure the long-term stable operation of perovskite devices.[9d] However, these measures have not fundamentally altered the structure of 3D perovskites, and the instability issues still need to be fundamentally resolved. The optimal solution for stability issues lies in improving the inherent chemical stability of halide perovskites themselves. One approach is moving from 3D perovskites to lower dimensional structures without sacrificing highly desirable optoelectronic properties.

Unlike small A-site cations that can fit inside the corner sharing Pb-X to form 3D octahedral matrices, larger organic cations force the octahedra apart, creating a two-dimensional (2D) layered structure.[16] The ability to tune many interactions of the organic cations (through molecular design) with the metal halide lattice opens up so much diversity and opportunity to impart the intended properties on the 2D material. Compared to 3D perovskites, the large cations in 2D perovskites can effectively "lock in" the inorganic framework and resist water and oxygen permeation, imparting higher environmental stability. Additionally, the introduction of discrete organic layers and the asymmetric lattice structure in 2D perovskites provide additional degrees of freedom to adjust their intrinsic physical properties, including optical bandgaps, exciton binding energies, and dielectric constants (ε_r),[1g, 9c, 17] enabling more

options for customizing the performance of devices such as PSCs and LEDs. Nevertheless, 2D perovskites are not without imperfections. Although greater flexibility in tuning the optoelectronic properties of 2D perovskites is enabled by increasing the bulk of the A-site cation, compositional and structural design benefits come with tradeoffs; the carrier transport performance of 2D perovskites is far inferior to that of 3D perovskites, inherently increasing the bandgap and diminishing their photoelectric properties.[17a] Composition engineering,[18] interface optimization,[13] and the introduction of external dopants[19] have been actively employed to mitigate these tradeoffs at a device level. What is currently lacking is the mechanistic understanding of the fundamental structural factors influencing the carrier transport performance in 2D perovskites.

A comprehensive understanding of the crystal structure features of perovskites and the relationship between structure and performance is crucial for the future design of novel 2D perovskite materials to combine the best of stability and performance. To date, comprehensive reviews are scarce to analyze the structure and performance of 2D perovskites. Most of them have primarily focused on analyzing interlayer cations.[20] While synthesizing 2D perovskites, researchers have lacked a clear theoretical foundation regarding the deliberate modulation of perovskite structures and improving their performance through an intentional composition selection. To address this issue comprehensively, this review first delves into a more wholistic analysis of the factors influencing the charge transport properties of 2D perovskites from four key aspects: (1) Pb-I-Pb bond angle and spin-orbit coupling (SOC), (2) interlayer distance and the thickness of the inorganic layers, (3) dielectric contrast and dipole moment, the (4) orientation and phases distribution. It then consolidates and compares the standard transport testing methods for 2D perovskites, followed by exploring measures to enhance charge transport properties from a compositional approach. The objective is to uncover the underlying mechanisms affecting the charge transport performance of 2D perovskites, thereby providing fundamental insights to enhance the synthesis strategies for these materials.

2. Where Does 2D End and 3D Begin?
2.1. Structure of 3D Perovskite
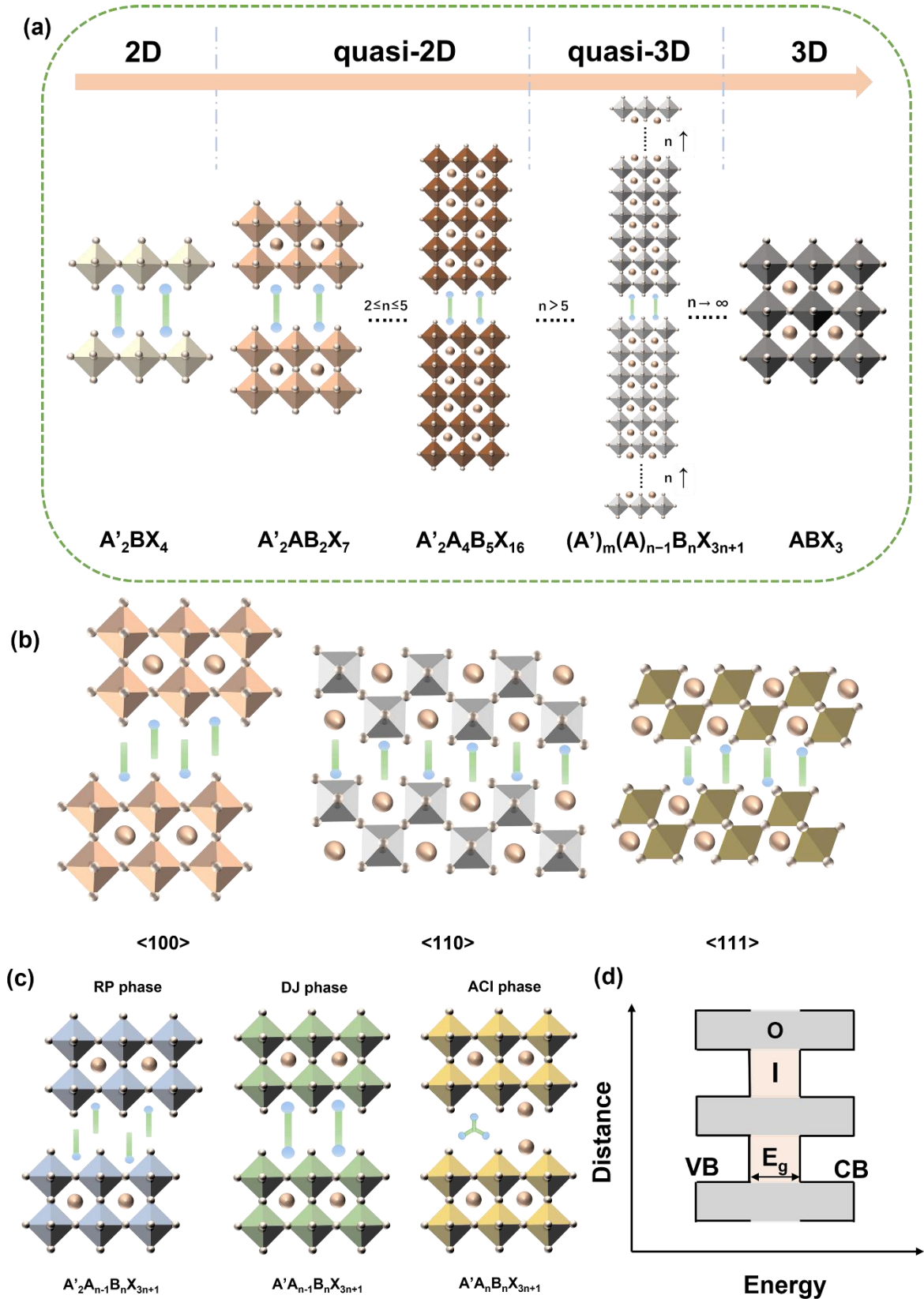
Figure 1. Schematic diagram of 2D perovskites with (a) different n values and (b) different crystal plane orientations. (c) 2D perovskite structure of RP phase, DJ phase, and ACI phase. (d) Schematic diagram of a QW, where "O" and "I" represent organic and inorganic layers in 2D perovskites.

The term "perovskite" originally referred to the mineral form $CaTiO_3$, named by Gustav Rose in 1839. It comprises a corner-sharing TiO_6^{3-} octahedra crystal structure, with Ca^{2+} occupying the cubic octahedral cavities in each unit cell. This structure was used by Victor Goldschmidt in 1926 as a general term for crystal structure groups. The focus of this review is primarily on metal halide perovskites, whose origins trace back to 1893 with Wells' research on $CsPbX_3$,[21] with greatly re-invigorated interest over the last few decades as optoelectronic materials.

The crystal structure of 3D halide perovskites is depicted in **Figure 1a**, wherein the structure is considered a 3D perovskite when the value of "n" approaches infinity, and thus a chemical formula of ABX_3. It comprises $[BX_6]^{4-}$ -units composed of metal and halide ions connected through corner-sharing octahedra in all directions, forming the 3D inorganic framework. The smaller monovalent A-site cations (+1 charge) occupy the interstitial pockets between the octahedra; common cations found at the A-site are Cs^+, MA^+, or FA^+. The B-site usually accommodates divalent cations such as Pb^{2+} and Sn^{2+}. The X-site represents halide ions, primarily I^-, Br^-, or Cl^-. I^- is the most commonly used in PSCs, with small amounts of bromide or chloride as doping agents to fine-tune the photoelectric properties.[22]

In 3D perovskites, selecting A, B, and X ions is crucial to forming a highly symmetric and perfect crystal structure for the inorganic octahedra. Considering that the A-site cations occupy the interstitial sites between the corner-sharing octahedra, their volume depends on the size of the inorganic octahedra. Hence, appropriate A-site cations are critical factors for the structural stability of perovskite. For the B-site and X-site ions, their sizes and electronegativities determine the size of the octahedral cage and the volume of the octahedral cavity that A-site cations can occupy. Therefore, selecting A-, B-, and X-site ions are interdependent. When larger or smaller A-site cations are introduced into the perovskite lattice, the "soft" inorganic octahedral layers undergo lattice distortions, tilting and twisting to accommodate the size of the A-site cations. The tilting and stacking of perovskite octahedra give rise to different phase structures and transitions. The Goldschmidt tolerance factor (t) can assess whether selecting A, B, and X ions will form a viable 3D perovskite structure and its corresponding crystal phase. The formula for the Goldschmidt tolerance factor is as follows:[23]

$$t = \frac{r_A + r_X}{\sqrt{2}(r_B + r_X)} \tag{1}$$

Where r_A, r_B, and r_X represent the ionic radii of the A, B, and X ions. Typically, the t within the range of 0.8 to 1.0 generates a structurally stable perovskite. When the tolerance factor is approximately 1, the ideal cubic phase (α) perovskite is formed. As the tolerance factor gradually decreases towards 0.8, the B-X-B bond angles in the perovskite deviate from the ideal

180°, resulting in octahedral tilting and inducing carrier anisotropy.[24] This often leads to the tetragonal phase (β) and orthorhombic phase (γ) perovskites with reduced symmetry. Furthermore, suppose the A-site cation is excessively small, leading to a significantly decreased tolerance factor (t much smaller than 1). In that case, severe distortion occurs in the $[BX_6]^{4-}$ octahedra, causing the B-X bonds to break. As a result, the material transitions from a corner-sharing 3D perovskite to a face-sharing non-perovskite structure (δ).[20d, 25]

2.2. Structure of 2D Perovskite

The earliest research on 2D metal halide perovskites was conducted by Maruyama et al. in 1986.[26] In contrast to the narrow compositional range of 3D metal halide perovskites (i.e., those capable of conforming to t limits), introducing larger organic A'-site cations (organic spacers) weakens the constraints imposed on forming viable 2D perovskites.

2D perovskites comprise two distinct components: an organic interlayer and an inorganic octahedral layer. The introduction of interlayer cations brings not only a novel compositional dimension denoted as A' but also unprecedented structural complexity and, by extension, tunability of optoelectronic properties. The dimensional reduction process can be envisioned as cleaving a 3D perovskite along a specific crystalline plane, forming numerous inorganic nanosheets (refer to Figure 1). These nanosheets are then assembled by intercalating interlayer cations between them, alternating the arrangement of organic and inorganic layers, and ultimately constructing a 2D perovskite in a bottom-up manner.[27] Analogous to 3D perovskites, the octahedra within the same inorganic layer (within the range of inorganic layer thickness) of most 2D perovskites are interconnected by sharing angles. Interlayer cations separate the adjacent inorganic octahedral layers, and the inorganic layer interacts with the organic interlayer through various hydrogen bonding, ionic bonding, or van der Waals forces.

The chemical formula of 2D perovskites is represented as $(A')_m(A)_{n-1}B_nX_{3n+1}$, where m represents the number of interlayer cations, typically 1 or 2, and n corresponds to the number of inorganic layers.[28] The value of n can be controlled by adjusting the stoichiometric ratio between A' site cations and A site cations. Generally, in 2D perovskites, as the thickness (number of layers) of the inorganic layer increases, the bandgap and exciton binding energy (E_b) of the material decreases.[29] When n equals 1, it is commonly considered a pure 2D perovskite with excessively high E_b, making it unsuitable for use in solar cells. On the other hand, when $2 \leq n \leq 5$, it is referred to as quasi-2D perovskites, and n > 5, it is referred to as quasi-3D perovskites. As n approaches infinity, we can consider the dimensionality of the perovskite to have been restored to the 3D state (**Figure 1a**). It is important to note that in

making quasi-2D films through rapid crystallization processes such as spin-coating, obtaining a film with pure n values is challenging due to different formation energies and polycrystallinity.[30]

Based on the crystallographic planes used to cleave the 3D perovskite, 2D perovskites can be categorized into different types: <100>, <110>, and <111> oriented layered perovskites (**Figure 1b**). Among these, the <100> orientation dominates the classification. Introducing most interlayer cations results in <100> oriented structures, making it the most common 2D perovskite structural motif. Interlayer cations can be categorized as monovalent (+1) or divalent (+2) based on their charge. The different geometries of these cations have distinct impacts on the crystal structure of 2D perovskites since ionic bonding may be with a single inorganic sheet versus two, respectively, across the organic interlayer gap. Therefore, building upon the <100> orientation, 2D perovskites can be further divided into three types: Ruddlesden-Popper (RP) phase, Dion-Jacobson (DJ) phase, and Alternating Cations in the Interlayer (ACI) phase, based on different molecular structures of the organic cations.[31] In most cases, the RP and DJ phases correspond to the previously mentioned A' site cation parameters, m = 2 or 1, respectively. For the ACI phase, current research primarily focuses on guanidinium (GA^+) as the interlayer cation, with relatively limited studies on the screening of intercalating cations.[32] Therefore, the discussion mainly focuses on perovskite's RP and DJ phases.

It's worth noting that the spatial offset of the inorganic layers determines whether it is an RP or DJ phase 2D perovskite. It was mentioned that "in most cases," RP corresponds to monovalent cations. However, some specific monovalent cations can also allow for eclipsed stacking between adjacent inorganic layers, exhibiting the characteristics of the DJ phase 2D perovskite.[33] Similarly, instances within divalent cations lead to the RP structure in 2D perovskites.[34] For these two particular types of 2D perovskites, simply categorizing them into RP and DJ phases may not be entirely appropriate and could confuse beginners, especially in the absence of reading the metal oxide perovskite literature (i.e., a significant body of work before metal halide perovskites).[35] The definition that lies between the two effectively resolves this dilemma. Marder *et al.* defined four structural types: monocation-DJ, dication-RP, near-DJ, and near-RP.[36] These additional structural classifications effectively refine the assignment of 2D perovskite structures to different cations. In conclusion, solely relying on the charge of the spacer cations is insufficient for accurately determining the structural classification of 2D perovskites, and differentiation based on the spatial arrangement is essential to discern the differences between various structures. We emphasize this point since nuanced structural difference impacts charge transport and optoelectronics.

2.2.1. RP Phase Perovskite

Figure 2. Summary of monoammonium organic spacer cations for 2D perovskite. 1, ethylammonium (EA, n = 1),[37] propan-1-ammonium (PA, n = 2),[37-38] butan-1-ammonium(BA, n = 3),[27, 37, 39] pentan-1-ammonium(PeA, n = 4),[37, 39c, 40] hexane-1-ammonium (HA, n = 5),[37, 39c, 40-41] heptan-1-ammonium (HeA, n = 6),[42] octan-1-ammonium (OA, n = 7),[42-43] nonan-1-ammonium (NA, n = 8),[42] decan-1-ammonium (DA, n = 9),[42, 43b] dodecan-1-ammonium (DoA, n = 11),[43b, 44] 1-tetradecanammonium (n = 13),[44] 1-hexadecylammonium (n = 15),[44]

1-octadecylammonium (n = 17);[43b, 44-45] 2, alkyl ammonium with different substituents;[39b, 46] 3, 3-carboxypropan-1-aminium (n = 3),[39b] 4-carboxybutan-1-aminium (n = 4),[47] 7-carboxyheptan-1-aminium (n = 7);[48] 4, 6-iodohexan-1-aminium;[49] 5, 2-fluoroethan-1-aminium;[50] 6, 2,2-difluoroethan-1-aminium;[50] 7, 2,2,2-trifluoroethan-1-aminium;[50-51] 8, 2-cyanoethan-1-aminium;[39b] 9, 3-bromopropan-1-aminium;[49] 10, 2-(methylthio)ethan-1-aminium;[52] 11, propan-2-aminium;[53] 12, 2-methylpropan-1-aminium (n = 1),[39a] 3-methylbutan-1-aminium (n = 2);[54] 13, prop-2-en-1-aminium;[55] 14, but-3-en-1-aminium;[56] 15, prop-2-yn-1-aminium (n = 1),[57] but-3-yn-1-aminium (n = 2);[56] 16, 1-methylhydrazin-1-ium;[58] 17, 2-ethylhexan-1-aminium;[59] 18, heptan-2-aminium;[59] 19, 3-((1,1,1,3,3,3-hexafluoro-2-(trifluoromethyl)propan-2-yl)oxy)propan-1-aminium;[60] 20, cyclopropanaminium;[61] 21, cyclobutanaminium;[62] 22, cyclopentanaminium;[62] 23, cyclohexanaminium;[62] 24, 4,4-difluorocyclohexan-1-aminium;[63] 25, cyclohexylmethanaminium (n = 1),[64] 2-cyclohexylethan-1-aminium (n = 2);[65] 26, (4-carboxycyclohexyl)methanaminium;[66] 27, 2-(cyclohex-1-en-1-yl)ethan-1-aminium;[67] 28, benzenaminium;[68] 29, N-methylbenzenaminium;[68a] 30, N,N-dimethylbenzenaminium;[68a] 31, N,N,N-trimethylbenzenaminium;[68a] 32, 1-phenylethan-1-aminium;[69] 33, 1-(4-chlorophenyl)ethan-1-aminium;[70] 34, 2-(3,5-dibromophenyl)ethan-1-aminium;[71] 35, 2-(3,5-dichlorophenyl)ethan-1-aminium;[71] 36, benzylammonium (n = 1),[39d, 72] phenylethylammonium (n = 2),[39d, 73] 3-phenylpropan-1-aminium (n = 3);[74] 37, (4-(trifluoromethyl)phenyl)methanaminium (X = CF$_3$),[46b] (4-vinylphenyl)methanaminium (X = -CH=CH$_2$),[75] Para-benzylamine replaced by halogens (X = F, Cl, Br, I);[46b, 72a, 76] 38, meta-phenylmethanamine replaced by halogens (X = F, Br);[76] 39, Para-phenylethylamine replaced by halogens (X = F, Cl, Br, -OCH$_3$, -CH$_3$);[46b, 73a-d, 77] 40, Ortho-replaced phenethylamine by halogens (X = F, Cl, Br);[78] 41, 2-(3-fluorophenyl)ethan-1-aminium;[78a] 42, 2-(perfluorophenyl)ethan-1-aminium;[79] 43, 3-(perchlorophenoxy)propan-1-aminium;[80] 44, 2-(4-methoxyphenyl)ethan-1-aminium;[73d] 45, 2-phenoxyethan-1-aminium;[81] 46, 5-((5-methoxynaphthalen-1-yl)oxy)pentan-1-aminium;[80] 47, (E)-3-phenylprop-2-en-1-aminium;[82] 48, (E)-2-(4-styrylphenyl)ethan-1-aminium;[83] 49, (E)-2-(4-(3-fluorostyryl)phenyl)ethan-1-aminium;[83] 50, (E)-2-(4-(phenyldiazenyl)phenoxy)ethan-1-aminium (n = 2), (E)-4-(4-(phenyldiazenyl)phenoxy)butan-1-aminium (n = 4), (E)-6-(4-(phenyldiazenyl)phenoxy)hexan-1-aminium (n = 6);[84] 51, 2-(2'',3'-dimethyl-[1,1':4',1''-terphenyl]-4-yl)ethan-1-aminium;[85] 52, 2-(5-(2,2'-dimethyl-[1,1'-biphenyl]-4-yl)thiophen-2-yl)ethan-1-aminium;[85] 53, naphthalen-1-aminium;[86] 54, naphthalen-1-ylmethanaminium;[87] 55, 1-(2-naphthyl)methanammonium (n = 1),[88] 2-(2-naphthyl)ethanammonium (n = 2);[88] 56, 2-(naphthalen-1-yloxy)ethan-1-aminium (n = 2),[89] 3-(naphthalen-1-yloxy)propan-1-aminium (n = 3),[89] 4-(naphthalen-1-yloxy)butan-1-aminium (n = 4),[80] 5-(naphthalen-1-yloxy)pentan-1-aminium (n = 5);[80] 57, anthracen-9-ylmethanaminium;[87b] 58, 2-(pyren-1-yloxy)ethan-1-aminium (n = 2),[89] 3-(pyren-1-yloxy)propan-1-aminium (n =3),[89] 4-(pyren-1-yloxy)butan-1-aminium (n = 4);[89] 59, pyren-1-ylmethanaminium (n = 1),[90] 4-(pyren-1-yl)butan-1-aminium (n = 4);[91] 60, 2-(perylen-3-yloxy)ethan-1-aminium;[89] 61, amino(phenyl)methaniminium;[92] 62, amino(4-fluorophenyl)methaniminium;[92] 63, selenophen-2-ylmethanaminium;[93] 64, amino(thiophen-

2-yl)methaniminium;[94] 65, 2-thienylmethylammonium (n = 1),[25, 39d, 73e, 95] 2-(2-thienyl)ethanaminium (n = 2);[73e] 66, 1H-benzo[d]imidazol-3-ium;[96] 67, 1-butyl-3-methyl-1H-imidazol-3-ium; 68, 2-(methylthio)-4,5-dihydro-1H-imidazol-1-ium;[97] 69, 1-butyl-3-methyl-1H-imidazol-3-ium;[98] 70, 3-iodopyridin-1-ium;[66] 71, 2-(pyridin-4-yl)ethan-1-aminium;[99] 72, 3-(9H-carbazol-9-yl)propan-1-aminium (n = 3),[100] 4-(9H-carbazol-9-yl)butan-1-aminium (n = 4),[100-101] 5-(9H-carbazol-9-yl)pentan-1-aminium (n = 5);[100] 73, 2-(1,3-dioxo-1,3-dihydro-2H-benzo[f]isoindol-2-yl)ethan-1-aminium;[102] 74, amino(thieno[3,2-b]thiophen-2-yl)methaniminium;[103] 75, [2,2'-bithiophen]-5-yl(amino)methaniminium;[103] 76, 2-([2,2'-bithiophen]-5-yl)ethan-1-aminium;[104] 77, 2-(3''',4'-dimethyl-[2,2':5',2'':5'',2'''-quaterthiophen]-5-yl)ethan-1-aminium;[104] 78, 2-(4'-methyl-5'-(7-(3-methylthiophen-2-yl)-4,5,6,7-tetrahydrobenzo[c][1,2,5]thiadiazol-4-yl)-[2,2'-bithiophen]-5-yl)ethan-1-aminium;[104] 79, 2-(4'-methyl-5'-(5-(3-methylthiophen-2-yl)selenophen-2-yl)-[2,2'-bithiophen]-5-yl)ethan-1-aminium;[105] 80, 2-(1,3,6,8-tetraoxo-7-propyl-3,6,7,8-tetrahydrobenzo[lmn][3,8]phenanthrolin-2(1H)-yl)ethan-1-aminium (n = 1),[106] 4-(1,3,6,8-tetraoxo-7-propyl-3,6,7,8-tetrahydrobenzo[lmn][3,8]phenanthrolin-2(1H)-yl)butan-1-aminium (n = 3),[106] 6-(1,3,6,8-tetraoxo-7-propyl-3,6,7,8-tetrahydrobenzo[lmn][3,8]phenanthrolin-2(1H)-yl)hexan-1-aminium (n = 5).[106]

In most cases, the chemical formula of the RP phase perovskite is $A'_2A_{n-1}B_nX_{3n+1}$. The interlayer cation " A' " is a monoammonium cation arranged staggered between adjacent inorganic octahedral layers (**Figure 2** provides an overview of the prevalent monoammonium organic spacer cations for RP-type perovskite). The interlayer cations form the interlayer of the RP phase perovskite (**Figure 1c**), along with the inorganic layers, creating a quantum well (QW) structure (**Figure 1d**). Within the interlayer, there are weak van der Waals forces between the two layers of interlayer cations. On the outer side of the interlayer, the interlayer cations are connected to the halide ions through hydrogen bonding and electrostatic interactions facilitated by the terminal ammonium groups.[9d, 25, 107] From a crystal structure perspective, the adjacent inorganic layers in RP phase perovskites exhibit a relatively sizeable interlayer distance due to bilayered organic cations within the interlayer; additionally, due to the staggered arrangement of interlayer cations, the adjacent inorganic layers in the RP phase perovskite exhibit a staggered configuration. When observed along the stacking axis, the inorganic layers show an offset of (1/2, 1/2) within the plane.[108]

RP phase perovskite is the most extensively studied class of perovskites, characterized by the diversity of interlayer cations, which enables constructing a vast perovskite network. Since 2014, a quasi-2D RP phase perovskite utilizing phenylethylammonium as the organic interlayer cation was employed as the light-absorbing layer in PSCs, achieving an impressive PCE of 4.73%.[109] Over the past decade, the PCE based on quasi-2D/3D perovskites has surpassed

20%.[110] This remarkable advancement is a testament to the immense potential of RP phase PSCs.

2.2.2. DJ Phase Perovskite
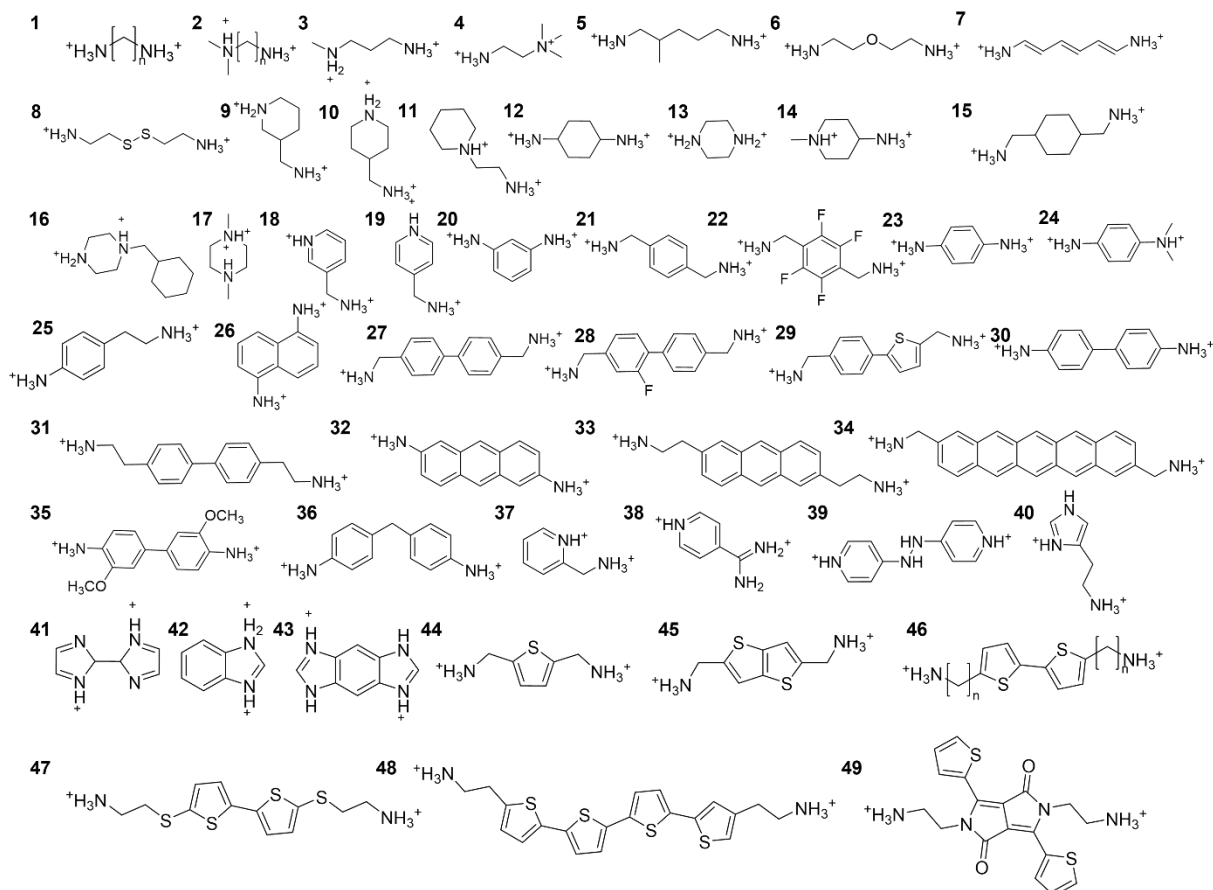
Figure 3. Summary of diammonium organic spacer cations for 2D perovskites. 1, ethane-1,2-diaminium (n = 2),[111] propyldiammonium (n = 3),[38b, 112] butyldiammonium (n = 4),[8c, 112a, 112b, 113] pentyldiammonium (n = 5), hexyldiammonium (n = 6),[112a, 113a, 114] heptyldiammonium (n = 7),[115] octyldiammonium (n = 8),[113a] nonyldiammonium (n = 9),[115] decyldiammonium (n = 10),[116] dodecyldiammonium (n = 12);[116] 2, 3-(dimethylamino)-1-propylamine (n = 3),[8c, 117] 4-dimethylaminobutylamine (n = 4);[117a] 3, N1-methylpropane-1,3-diaminium;[118] 4, N1,N1,N1-trimethylethane-1,2-diaminium;[119] 5, 2-methylpentane-1,5-diaminium;[120] 6, 2,2'-oxybis(ethan-1-aminium);[121] 7, (1E,3E,5E)-hexa-1,3,5-triene-1,6-diaminium;[122] 8, 2,2'-disulfanediylbis(ethan-1-aminium);[49, 123] 9, 3-(ammoniomethyl)piperidin-1-ium;[28b, 124] 10, 4-(ammoniomethyl)piperidin-1-ium;[28b, 124a, 125] 11, 1-(2-ammonioethyl)piperidin-1-ium;[66] 12, cyclohexane-1,4-diaminium;[114c] 13, piperazine-1,4-diium;[126] 14, 4-ammonio-1-methylpiperidin-1-ium;[127] 15, cyclohexane-1,4-diyldimethanaminium;[114a] 16, 1-(cyclohexylmethyl)piperazine-1,4-diium;[126] 17, 1,4-dimethylpiperazine-1,4-diium;[126] 18, 3-

(ammoniomethyl)pyridin-1-ium;[128] 19, 4-(ammoniomethyl)pyridin-1-ium;[128] 20, benzene-1,3-diaminium;[129] 21, 1,4-phenylenedimethanaminium;[22, 31b, 72b] 22, (perfluoro-1,4-phenylene)dimethanaminium;[130] 23, benzene-1,4-diaminium;[112b] 24, N1,N1-dimethylbenzene-1,4-diaminium;[131] 25, 4-(2-ammonioethyl)benzenaminium;[132] 26, naphthalene-1,5-diaminium;[133] 27, [1,1'-biphenyl]-4,4'-diyldimethanaminium;[114a, 134] 28, (2-fluoro-[1,1'-biphenyl]-4,4'-diyl)dimethanaminium;[134] 29, (5-(4-(ammoniomethyl)phenyl)thiophen-2-yl)methanaminium;[134] 30, [1,1'-biphenyl]-4,4'-diaminium;[122b] 31, 2,2'-([1,1'-biphenyl]-4,4'-diyl)bis(ethan-1-aminium);[122b] 32, anthracene-2,6-diaminium;[122b] 33, 2,2'-(anthracene-2,6-diyl)bis(ethan-1-aminium);[122b] 34, pentacene-2,9-diyldimethanaminium;[122b] 35, 3,3'-dimethoxy-[1,1'-biphenyl]-4,4'-diaminium;[122a] 36, 4,4'-methylenedibenzenaminium; 37, 2-(ammoniomethyl)pyridin-1-ium;[135] 38, 4-(amino(iminio)methyl)pyridin-1-ium;[136] 39, 4,4'-(hydrazine-1,2-diyl)bis(pyridin-1-ium);[34] 40, 4-(2-ammonioethyl)-1H-imidazol-3-ium;[137] 41, 2H,2'H-[2,2'-biimidazole]-1,1'-diium;[138] 42, 1H-benzo[d]imidazole-1,3-diium;[96] 43, 3,7-dihydrobenzo[1,2-d:4,5-d']diimidazole-1,5-diium;[139] 44, thiophene-2,5-diyldimethanaminium;[28a] 45, thieno[3,2-b]thiophene-2,5-diyldimethanaminium;[140] 46, [2,2'-bithiophene]-5,5'-diyldimethanaminium (n = 1),[141] 2,2'-([2,2'-bithiophene]-5,5'-diyl)bis(ethan-1-aminium) (n = 2);[142] 47, 2,2'-([2,2'-bithiophene]-5,5'-diylbis(sulfanediyl))bis(ethan-1-aminium);[143] 48, 2,2'-([2,2':5',2'':5'',2'''-quaterthiophene]-4,5'''-diyl)bis(ethan-1-aminium);[144] 49, 2,2'-(1,4-dioxo-3,6-di(thiophen-2-yl)pyrrolo[3,4-c]pyrrole-2,5(1H,4H)-diyl)bis(ethan-1-aminium).[145]

When the organic interlayer cations lead to a situation where the adjacent inorganic layers exhibit perfect overlap, aka eclipsed octahedra, this structure is called the DJ phase structure. Typically, this type of structure forms from diammonium cations, although there are cases where monoammonium cations can also form DJ phase structures.[134] **Figure 3** provides an overview of prevalent diammonium organic spacer cations, with a chemical formula of $A'A_{n-1}B_nX_{3n+1}$ in most instances. The interlayer cations " A' " are connected to neighboring inorganic layers through hydrogen bonding and electrostatic interactions. In contrast to the typical RP phase featuring monoammonium cations, as shown in **Figure 1c**, the DJ phase only consists of a single layer of interlayer cations, lacking the weaker intralayer van der Waals interactions in RP phases. These van der Waals forces are replaced by stronger chemical bonds, thereby mitigating quantum confinement effects and significantly enhancing the structural stability between the organic and inorganic layers.[17b, 146]

Furthermore, compared to the RP phase, in the crystal structure of DJ phase perovskites, when viewed along the stacking axis, adjacent inorganic layers can perfectly stack together, exhibiting an offset of (0, 0) within the inorganic layer plane.[147] This arrangement is due to the tight packing of single-layer interlayer cations with shorter chain lengths between neighboring inorganic layers. The single-layer interlayer cations significantly reduce the interlayer distance in the inorganic layers, making them comparable to or even smaller than the van der Waals radius of the halide atoms.[148] This leads to stronger electronic coupling and interlayer interactions between adjacent inorganic layers.[28a, 149] These characteristics contribute to the enhanced charge transfer of the DJ phase perovskite, thereby fostering the potential for higher device performance.

2.2.3. ACI Phase Perovskite

ACI phase perovskite is another type of 2D perovskite with the chemical formula of $A'A_nB_nX_{3n+1}$.[150] Unlike RP and DJ phase 2D perovskites, the choice of A' is limited for the ACI phase, with only a few cations reported, such as GA^+.[151] Additionally, in the crystal structure, two interlayer cations (A' and A) alternate between the inorganic layers.[152] The adjacent inorganic layers offset along the A'/A alternating direction while appearing perfectly stacked along another direction, exhibiting an overall offset of (1/2, 0) within the inorganic layer plane. It should be noted that only structures meeting these spatial arrangements and having a clear crystal structure can be referred to as ACI phase 2D perovskites.

The unique structure also results in different physicochemical properties. Compared to RP phase 2D perovskites, in the ACI phase, smaller interlayer cations and tight stacking between inorganic layers significantly reduce both the van der Waals gap between interlayer cations and the distance between inorganic layers.[153] Specifically, the shorter distance between inorganic layers and partial overlap of axial halide atomic orbitals enable it to weaken the challenge of out-of-plane carrier transport while maintaining excellent chemical stability, making it a promising 2D perovskite material.[154]

3. Charge Transport in Halide Perovskites

3.1. Charge Transport in 3D Perovskite

In 3D halide perovskites, the $[BX_6]^{4-}$ octahedra serves as the perovskite's structural scaffold and the carrier's transport framework. The bond length (B-X) and bond angle (B-X-B) between the metal and halide ions determine the orbital hybridization between these two elements, which in turn influences the energy level structure and optoelectronic properties of

the photo-generated carriers.[155] In the octahedral $[PbX_6]^{4-}$ unit, the σ-anti-bonding overlap of Pb 6s and I 5p orbitals determines the valence band maximum (VBM) of the 3D perovskite. In contrast, the conduction band minimum (CBM) is mainly determined by the Pb 6p and I 5p orbitals. The better the orbital overlap between the metal and halide ions, the smaller the corresponding bandgap. Furthermore, the orbital overlap is greatly influenced by the crystal structure, and thus, the lattice structure of perovskites plays a crucial role in their optoelectronic performance. An ideal cubic-phase perovskite exhibits superior optoelectronic properties.[156] It is worth noting that the A-site cation's contribution to the band structure is far from the band edges. Therefore, in 3D perovskite crystals, the electronic structure is primarily governed by the octahedra formed by the metal and halide ions. However, the A-site cation remains an essential factor influencing the optoelectronic properties of perovskites. It indirectly affects the bandgap by controlling the degree of distortion in the B-X-B octahedra and introducing a small amount of crystallographic plane anisotropy.[24]

As previously stated, the structure and chemical composition of 3D perovskites significantly influence their optoelectronic performance. The introduction of the tolerance factor also greatly aids in determining the suitable chemical composition for stabilizing the perovskite structure and predicting the resulting crystalline phases. A diminutive A-site cation forms the δ-phase, weakening the coupling of the s−p orbital between B and X, resulting in a larger bandgap. Conversely, introducing a larger A-site cation causes the 3D perovskite to undergo molecular-level dimensional reduction, forming 2D perovskites when t exceeds 1. Even for a broad range of 3D-forming compositions and, by extension, nuanced 3D structural variety, carrier transport dynamics also span a wide range.[157]

3.2. Charge Transport in 2D Perovskite

Compared to 3D perovskite, 2D perovskite exhibits inferior charge transport performance as anisotropy of the inorganic framework forms. There are several reasons for this phenomenon. Firstly, due to the structural symmetry, there is nearly zero dispersion along the direction perpendicular to the inorganic layers in 2D perovskite materials, indicating weak coupling.[158] The motion of electrons in the direction perpendicular to the perovskite crystal plane is restricted, resulting in a localized narrow band. Additionally, electronic structure distortions arising from the electron-phonon interaction in the Jahn-Teller effect further narrow the localized energy bands.[159] Consequently, 2D perovskites exhibit a wider bandgap compared to their 3D counterparts. Secondly, the unique physicochemical properties of organic spacer cation ligands significantly influence the photoelectric performance of 2D perovskites.

Hydrophobic organic spacer cations can separate the conducting inorganic layers, forming a QW structure (**Figure 1**).[22, 27, 31b] The inorganic layers and organic spacers act as potential wells and barriers, respectively. Organic spacers disrupt the orbital hybridization between adjacent inorganic layers, confining the photo-generated charge carriers within the inorganic layers and severely impeding the external charge transport.[160] Moreover, the ε_r of the organic spacer cations in 2D perovskites is much smaller than that of the inorganic octahedral layers, resulting in dielectric solid confinement effects. The organic spacers provide poor charge screening for excitons, enhancing the Coulomb interaction between photo-generated electrons and holes. The pronounced quantum confinement and dielectric confinement effects contribute to a higher E_b in 2D perovskites, forming excitons rather than free electrons and holes, resulting in limited charge transport capability and lower PCE.[17a, 31a] Thirdly, introducing organic spacer cations leads to changes in the stacking of inorganic octahedral layers and distortion of the bond angles and lengths between metals and halides. These changes significantly impact the orbital overlap between metal and halide ions, ultimately influencing the bandgap. Fourthly, 2D perovskite films by solution methods often consist of a mixture of multiple QWs with a random distribution of well widths (n-values) and respective orientations. This leads to lower charge carrier mobility and diffusion length from a bulk material perspective.[73c, 107a] Consequently, while 2D perovskites exhibit good stability, these mixed QWs pose challenges in attaining superior photoelectric performance.

While it is true that 2D perovskite lags behind 3D perovskite in terms of charge transport performance, the charge transport in 2D perovskite is also inextricably linked to its crystal structure. The orbitals of the metal and halide atoms in the inorganic layers determine the band edges of 2D perovskites. At the same time, the A' site interlayer cations and A-site cations do not directly contribute to the band structure.[28b, 124c] In semiconductor materials, the VBM and CBM play a crucial role in determining the electronic structure and properties of the material. The shape of the band structure and the distance between the band edges are essential indicators for light absorption, emission capability, and charge carrier mobility. Perovskites exhibit soft lattice characteristics, wherein atomic positions within the lattice fluctuate, leading to bond angles and length variations within the inorganic framework. Changes in the CBM and VBM reflect these structural fluctuations. Therefore, understanding and managing the energy positions of the VBM and CBM are crucial for designing and optimizing the charge transport performance of 2D perovskite materials. This article will explore the factors influencing the charge transport performance of 2D perovskite from the following perspectives (**Figure 4**).
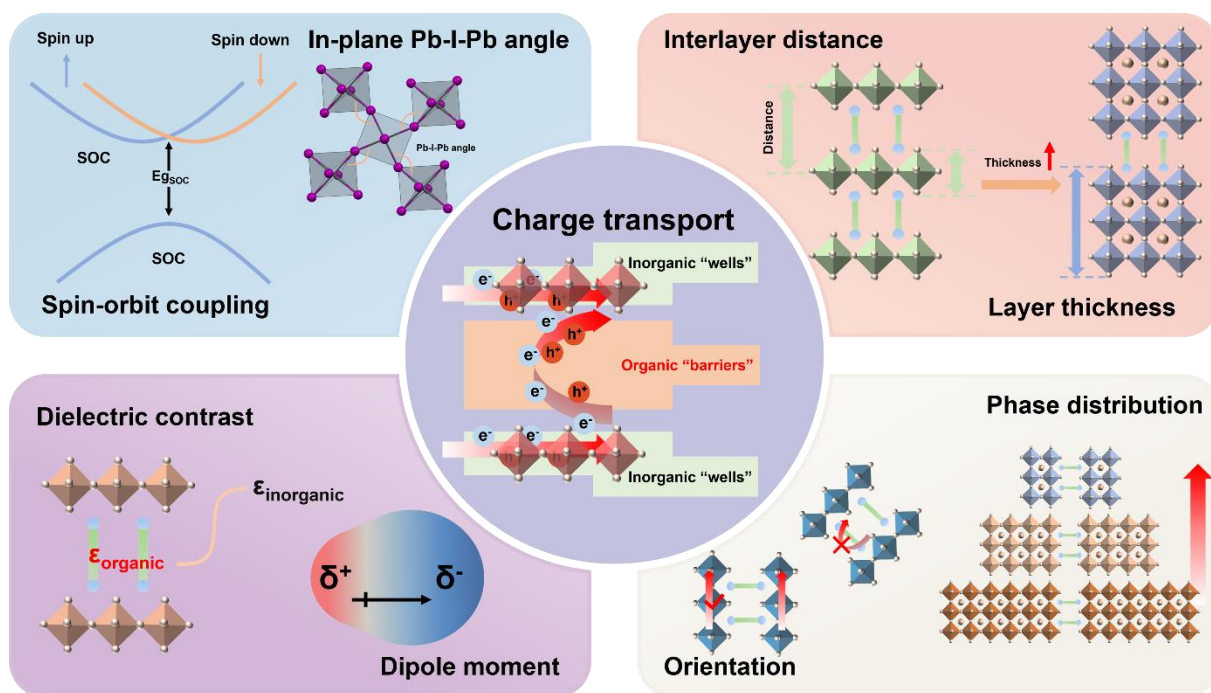
Figure 4. Summary of Factors Influencing Charge Transport Performance in 2D Perovskites

3.2.1. The Angle of the Pb-I-Pb Bond and the Spin-Orbit Coupling

For 2D perovskites, the VBM primarily arises from the antibonding overlap of the metal and halide orbitals. At the same time, the orbitals of the metal mainly contribute to the CBM at the B site.[114a] **Table 1** and **Figure 5** depict the relationship between the average in-plane Pb-I-Pb bond angle and bandgap of 2D perovskites with monoammonium and diammonium spacer cations (n = 1). Although the bond angle range corresponding to the same bandgap is relatively large, the overall trend of the bandgap variation between the two phases decreases with the increase of the average in-plane Pb-I-Pb bond angle. The relatively subtle correlation highlights the diversity and complexity of factors influencing the bandgap. However, from the Pb-I-Pb bond angle's perspective, the bandgap variation trend can be explained by the enhanced linearity of the B-X-B bond angle in the more symmetric crystal structure of 2D perovskites. This results in increased overlap between the metallic and halogen s-p orbitals. Consequently, there is a more significant dispersion of the VBM, causing an upward shift of the conduction band, ultimately contributing to a reduced bandgap. When the crystal structure starts to distort, the aforementioned orbital overlap weakens, resulting in a decrease in valence bandwidth and an increase in the band gap. Hence, the crystal structure of 2D perovskites, particularly the Pb-I-Pb bond angle, is a crucial factor influencing its bandgap. Furthermore, heavy metals at the B site in 2D perovskites introduce SOC, significantly impacting the electronic structure.[161] SOC can modify the band structure of electrons, leading to band splitting and the formation of new

band structures, such as spin-split bands and band gaps, which influence the optoelectronic properties of the material. In summary, the configuration and composition of the inorganic octahedra in 2D perovskites continue to play a crucial role in fundamental optoelectronic properties such as bandgap, charge carrier mobility, and light absorption.
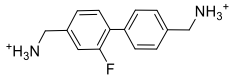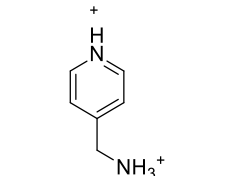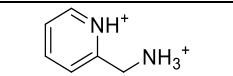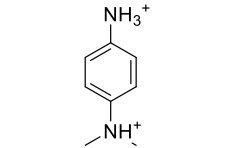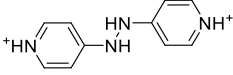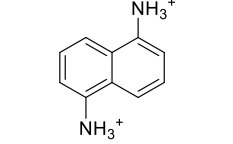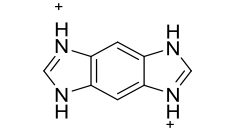
Table 1. Summary of the structural and optical properties of 2D perovskites with monoammonium and diammonium spacer cations (n = 1)
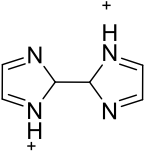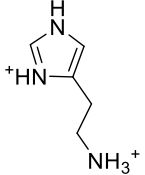
		Spacer cation	Compound	Space group	Bandgap (eV)	Average in-plane Pb-I-Pb (°)
Monoammonium	1[55a]		$[CH_3(CH_2)_2NH_3]_2PbI_4$	$P21/c$	2.29	148.16
	2[162]		$[CH_3CH(CH_3)CH_2NH_3]_2PbI_4$	$P21/c$	2.28	156.50
	3[49]		$[HO(CH_2)_2NH_3]_2PbI_4$	$P21/c$	2.16	159.10
	4[49]		$[HO(CH_2)_3NH_3]_2PbI_4$	$P21/c$	2.14	163.68
	5[49]		$[I(CH_2)_2NH_3]_2PbI_4$	$P21/c$	2.37	147.25
	6[49]		$[I(CH_2)_3NH_3]_2PbI_4$	$P21/c$	2.29	148.76
	7[49]		$[I(CH_2)_4NH_3]_2PbI_4$	$P21/c$	2.28	147.02
	8[163]		$[CH_3(CH_2)_3NH_3]_2PbI_4$	$Pbca$	2.27	155.08
	9[163]		$[CH_3(CH_2)_4NH_3]_2PbI_4$	$Pbca$	2.29	155.65
	10[163]		$[CH_3(CH_2)_5NH_3]_2PbI_4$	$Pbca$	2.29	155.65
	12[42]		$[CH_3(CH_2)_6NH_3]_2PbI_4$	$Pbca$	2.27	156.06
	13[42]		$[CH_3(CH_2)_7NH_3]_2PbI_4$	$Pbca$	2.28	156.06
	14[42]		$[CH_3(CH_2)_9NH_3]_2PbI_4$	$Pbca$	2.39	149.60
	15[42]		$[CH_3(CH_2)_{10}NH_3]_2PbI_4$	$P21/c$	2.39	149.98
	16[49]		$[I(CH_2)_6NH_3]_2PbI_4$	$Pbca$	2.22	160.98
	17[59]		$[CH_3(CH_2)_3CH(C_2H_5)CH_2NH_3]_2PbI_4$	$P21/c$	2.31	153.98
	18[59]		$[CH_3(CH_2)_4CH(CH_3)NH_3]_2PbI_4$	$P21/c$	2.28	153.87
	19[164]		$[HOOC(CH_2)_3NH_3]_2PbI_4$	$Pbca$	2.16	159.12

	Structure	Formula	Space group		
20[48]	HO–(C=O)–(CH₂)₇–NH₃⁺	(COOH(CH₂)₇NH₃)₂PbI₄	*P21/c*	2.29	147.48
21[63]	F₂–cyclohexyl–NH₃⁺	[F₂C₆H₉NH₃]₂PbI₄	*Cmc21*	2.38	151.35
22[65]	cyclohexenyl–(CH₂)₂–NH₃⁺	[C₆H₉(CH₂)₂NH₃]₂PbI₄	*P-1*	2.25	149.81
23[165]	C₆H₅–CH(CH₃)–NH₃⁺	[C₆H₅CH(CH₃)NH₃]₂PbI₄	*P21/c*	2.3	155.43
24[70]	Cl–C₆H₄–CH(CH₃)–NH₃⁺	[ClC₆H₄CH(CH₃)NH₃]₂PbI₄	*P1*	2.38	153.17
25[166]	C₆H₅–CH₂–NH₃⁺	[C₇H₁₀N]₂PbI₄	*Pbca*	2.27	157.80
26[36, 166]	F–C₆H₄–CH₂–NH₃⁺	[FC₆H₅CH₂NH₃]₂PbI₄	*P21/n*	2.25	158.35
				2.24	158.80
27[36, 166]	Cl–C₆H₄–CH₂–NH₃⁺	[ClC₆H₅CH₂NH₃]₂PbI₄	*P21*	2.31	154.49
				2.34	154.05
28[36, 166]	Br–C₆H₄–CH₂–NH₃⁺	[BrC₆H₅CH₂NH₃]₂PbI₄	*P21*	2.33	153.05
				2.33	154.02
29[36]	I–C₆H₄–CH₂–NH₃⁺	[IC₆H₅CH₂NH₃]₂PbI₄	*P21/c*	2.22	156.11
30[167]	Br–C₆H₄–(CH₂)₂–NH₃⁺	[BrC₆H₄(CH₂)₂NH₃]₂PbI₄	*C2/c*	2.31	152.15
31[167-168]	Cl–C₆H₄–(CH₂)₂–NH₃⁺	[ClC₆H₄(CH₂)₂NH₃]₂PbI₄	*C2/c*	2.31	152.48
				2.32	153.64
32[168]	F–C₆H₄–(CH₂)₂–NH₃⁺	[FC₆H₄(CH₂)₂NH₃]₂PbI₄	*P21/c*	2.23	152.94

	33[169]		[C8H11BrN]2PbI4	*P21*	2.34	144.54
	34[71]		[C8H10Br2N]2PbI4	*P21/c*	2.32	158.2
	35[170]		[C9H14ON]2PbI4	*P-1*	2.23	151.94
	36[89]		[C10H7O(CH2)2NH3]2PbI4	*Cc*	2.32	156.00
	37[89]		[C10H7O(CH2)3NH3]2PbI4	*P21/c*	2.42	146.87
	38[80]		[C14H18NO]2PbI4	*Pca21*	2.33	152.93
	39[80]		[C16H22NO]2PbI4	*P21/c*	2.34	147.93
	40[89]		[C16H9O(CH2)2NH3]2PbI4	*Cc*	2.32	154.69
	41[89]		[C16H9O(CH2)4NH3]2PbI4	*C2/c*	2.27	154.58
	42[91]		[C16H9(CH2)2NH3]2PbI4	*P21/c*	2.36	149.26
	43[89]		[C20H11O(CH2)2NH3]2PbI4	*P21/c*	2.35	155.23
	44[171]		[C4H3SCH2NH3]2PbI4	*Pbca*	2.2	153.47
	45[172]		[C22H20N3S4]2PbI4	*P-1*	2.3	151.27
Diammonium	1[116]		[NH3(CH2)4NH3]PbI4	*C2/c*	2.2	147.18
	2[113a]		[NH3(CH2)6NH3]PbI4	*P21/c*	2.28	148.31

3[116]	+H₃N⁤[chain]₈NH₃⁺	[NH₃(CH₂)₈NH₃]PbI₄	*P21/c*	2.37	147.62
4[115]	+H₃N[chain]₉NH₃⁺	[NH₃(CH₂)₉NH₃]PbI₄	*Cc*	2.29	153.75
5[116]	+H₃N[chain]₁₂NH₃⁺	[H₃N(CH₂)₁₂NH₃]PbI₄	*P21/c*	2.36	148.30
6[49]	+H₃N–S–S–NH₃⁺	[H₃N(CH₂)₂SS(CH₂)₂NH₃]PbI₄	*P21/c*	2.17	162.22
7[173]	+H₃N cyclohexane NH₃⁺	[NH₃CH₂C₆H₁₀CH₂NH₃]PbI₄	*P21/c*	2.31	153.14
8[28b]	+H₂N piperidine NH₃⁺	[C₅H₁₁NCH₂NH₃]PbI₄	*P21/c*	2.23	165.15
9[28b]	+H₂N piperidine NH₃⁺	[C₅H₁₁NCH₂NH₃]PbI₄	*Pc*	2.38	154.38
10[127]	—NH⁺ ring NH₃⁺	[C₆H₁₆N₂]PbI₄	*P21/c*	2.17	158.37
11[174]	piperidine NH⁺ NH₃⁺	[C₅H₁₀N(CH₂)₂NH₃]PbI₄	*P21/c*	2.17	170.63
12[175]	+H₃N benzene NH₃⁺	[NH₃CH₂C₆H₄CH₂NH₃]PbI₄	*P21/c*	2.3	150.88

13[134]		[H₃NCH₂C₆H₃FC₆H₄CH₂NH₃]PbI₄	*Pcca*	2.12	159.51
14[130]		[NH₃CH₂C₆F₄CH₂NH₃]₂PbI₄	*P21/c*	2.28	144.42
15[128]		[C₅H₄NCH₂NH₃]PbI₄	*Pc (Pn)*	2.17	149.15
16[176]		[C₅H₄NH(CH₂)NH₃]PbI₄	*Pbca*	2.14	167.76
17[131]		[(CH₃)₂NHC₆H₄NH₃]PbI₄	*P21/c*	2.17	171.85
18[34]		[C₁₀N₄H₁₂]PbI₄	*P2/c*	-	180.00
19[116]		[H₃NC₁₀H₆NH₃]PbI₄	*P21/c*	2.29	150.67
20[139]		[C₈H₈N₄]PbI₄	*C2/m*	2.04	180.00

22

21[138]		$[C_6H_8N_4]PbI_4$	C2/c	2.11	173.69
22[137]		$[C_3H_4N_2(CH_2)_2NH_3]PbI_4$	P21/c	2.04	167.27
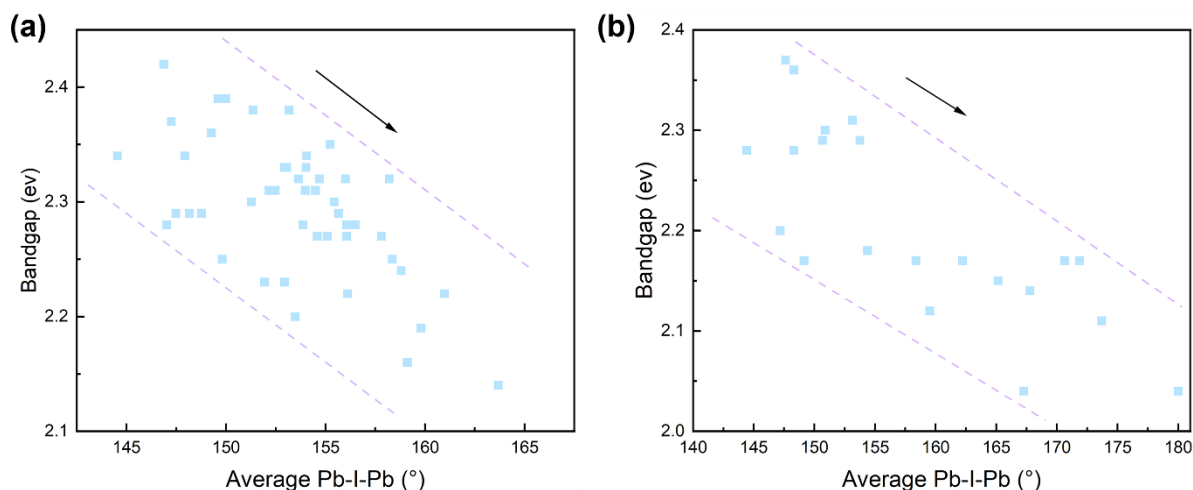
Figure 5. Trend diagram of bond angle and bandgap change of 2D perovskites with (a) monoammonium and (b) diammonium spacer cations.

3.2.2. The Interlayer Distance and the Thickness of the Inorganic Layers

Unlike 3D perovskites, introducing interlayer cations adds the structural parameter of interlayer spacing to perovskite materials. In addition to dynamic lattice distortions causing fluctuations in the CB and VB energies,[177] the interlayer spacing is also an important parameter affecting the electronic band structure of 2D perovskites. As analyzed earlier, the magnitude of the interlayer spacing largely depends on the type of interlayer cations. In most cases, compared to the RP phase 2D perovskite, the DJ phase significantly reduces interlayer spacing due to single-layer diammonium cations. The strengthening interlayer electronic coupling between inorganic layers helps mitigate the impact of quantum confinement effects, reduce the bandgap of 2D perovskites, enhance charge carrier migration efficiency, and improve their optoelectronic properties.[178]

In addition to the distance between layers, the inorganic layer/slab thickness (value of n) also plays a crucial role in the optoelectronic properties of 2D perovskites. In 2D perovskites, the interlayer cations influence the lattice structure of perovskites through hydrogen bonding and electrostatic interactions with the halide atoms in the inorganic layers, ultimately impacting the optoelectronic properties. Increasing the thickness of the inorganic layers significantly weakens the influence of interlayer cations.[179] Furthermore, the quantum confinement and dielectric confinement effects in 2D perovskites result in excessively large exciton binding energies, which are disadvantageous for generating photoexcited charge carriers. However, increasing the thickness of the inorganic layers helps alleviate these adverse effects. Therefore, the thickness of the inorganic layers plays a crucial role in mitigating the detrimental effects of

quantum and dielectric confinement, improving the generation of photoexcited charge carriers, and ultimately enhancing the optoelectronic performance of 2D perovskites.

3.2.3. Dielectric Contrast and Dipole Moment
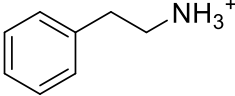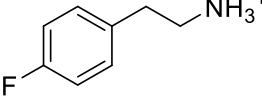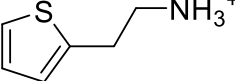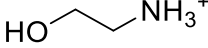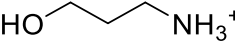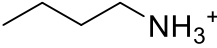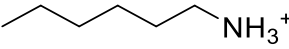
Efficient carrier transport is crucial for improving the optoelectronic performance of 2D perovskites. In 2D perovskites, interlayer cations are not limited to regulating carrier transport efficiency solely by affecting interlayer distance. Modulating E_b can also be achieved by altering the dielectric constant of the spacer cations.[180]
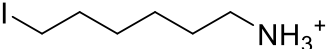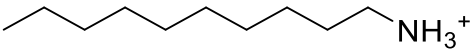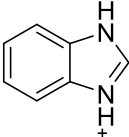
E_b is crucial for evaluating semiconductor materials' optical and photophysical properties. Compared to 3D perovskites, the enhanced E_b in 2D perovskites originates from the material's pronounced quantum and dielectric confinement effects.[181] The spatial range of the exciton wavefunction in the out-of-plane direction is constrained by quantum confinement,[182] leading to enhanced electron-hole interactions within the exciton. A higher E_b not only suppresses the optical generation efficiency of charge carriers but also limits the exciton diffusion length,[179, 183] unfavorable for charge transport efficiency in devices.

The significant difference in ε_r between the inorganic and organic spacer layers in 2D perovskites leads to a large E_b. On the one hand, the impact of this heterogeneous dielectric environment can be mitigated by increasing the thickness of the QWs.[184] On the other hand, by selecting interlayer cations with a higher ε_r, the dielectric mismatch between the inorganic and organic layers can be reduced, decreasing the E_b and facilitating the generation of photoexcited charge carriers.[128] Additionally, organic interlayer cations with higher ε_r can form ionic dipoles in the perovskite material, providing additional energy pathways that promote charge transfer. The formation of these ionic dipoles enhances the convenience of charge transfer, reducing charge scattering and losses. **Table 2** summarizes the dielectric constants of different spacer cations.

Regarding the difference in dipole moments between interlayer cations, a more significant dipole moment can effectively enhance the interaction between the interlayer and the inorganic layer, reduce the exciton binding energy, and promote charge dissociation in 2D perovskites.[51, 76, 185] Furthermore, the magnitude of the dipole moment can also influence the work function and energy levels of perovskites, which can be utilized to modulate the performance of devices.[186]

Table 2. Summary of the dielectric constants of space cations in different compounds. 'ε_b' represents the dielectric constant of the interlayer.

Compound	Spacer cation	ε_b	Ref.
(PEA)$_2$PbI$_4$		3.3	[187]
		2.34	[188]
(PEA)$_2$PbBr$_4$		3.81	[189]
(PEA)$_2$SnI$_4$		1.648	[190]
(PEA)$_2$(MA)Pb$_2$I$_7$		3.197	[191]
		2.34	[188]
(PEA)$_2$(MA)$_{m-1}$Pb$_m$I$_{3m+1}$ (m = 1-2)		2.34	[192]
(PEA)$_2$(MA)$_4$Pb$_5$I$_{16}$		3.314	[193]
(F-PEA)$_2$SnI$_4$		1.616	[190]
(TEA)$_2$SnI$_4$		1.645	[190]
(EA)$_2$PbI$_4$		37.7	[187, 194]
(AP)$_2$PbI$_4$		28	[187a]
(BA)$_2$PbI$_4$		~4	[195]
		2.1	[196]
(BA)$_2$PbBr$_4$		2.1	[197]
(BA)$_2$(MA)Pb$_2$I$_7$		1.753	[191]
(BA)$_2$(MA)$_3$Pb$_4$I$_{13}$		2.23	[188]
(BA)$_2$(MA)$_4$Pb$_5$I$_{16}$		1.9	[198]
(BA)$_2$(MA)$_{m-1}$Pb$_m$I$_{3m+1}$ (m = 2-5)		2.1	[199]
(HA)$_2$PbI$_4$		2.1	[197, 200]

Compound	Structure	Value	Ref.
(I-HA)$_2$PbI$_4$		~4	[201]
(DA)$_2$PbI$_4$		2.1	[188]
		2.9	[196c]
		2.2	[202]
		2.4	[203]
(BM)$_2$PbBr$_4$		3.28	[189]

3.2.4. The Orientation and Phases Distribution in Thin Films

In addition to the impacts above, organic cation design influences the perovskite thin film material's orientation, phase purity, and phase distribution. The spacer cations' size, shape, and charge characteristics can affect lattice distortion and matching, influencing the stability and formation of specific phases, crystallite growth size, and phase distribution in a polycrystalline film. Therefore, the appropriate selection and control of spacer cations can promote the formation of desired phases, prevent the occurrence of impurities, and improve phase purity. The phase composition of 2D perovskites plays a significant role in the decay kinetics of charge carriers. Random phase distribution increases energy disorder and charge recombination losses, resulting in faster decay kinetics. In contrast, a uniform and long-range ordered phase distribution facilitates the dissociation of excitons and dramatically reduces energy losses between different phases.[204]

The anisotropic transport of photoexcited charge carriers within the film influences the ideal orientation required for a functional perovskite device. In 2D perovskites, due to quantum and dielectric confinement effects, the transport of electrons and holes mainly occurs within the inorganic layers, resulting in lower charge transfer efficiency across layers through organic spacers.[123b, 205] Since achieving efficient carrier transport is crucial for enhancing optoelectronic performance, obtaining vertically (relative to electrodes) oriented 2D perovskite films plays a vital role. The spacer cations' size and shape directly impact the crystals' stacking arrangement. Larger spacer cations can increase the intercrystalline space, promoting a cubic stacking of the film and thereby leading to better orientation and crystalline properties. Furthermore, spacer cations with specific shapes can also regulate crystal orientation through spatial confinement and steric effects.[206] Therefore, by optimizing the selection of spacer cations, improved crystal orientation and crystalline properties can be achieved, ultimately enhancing the materials' optoelectronic and device performance.

Near the end of this section, it is essential to emphasize that despite the separate discussion of numerous influencing factors earlier, the transport mechanism of 2D perovskites remains highly complex. Generally, shorter interlayer distances imply better charge transport performance,[207] but exceptions exist.[129] Undeniably, the transport performance of 2D perovskites is influenced by multiple factors simultaneously. To further differentiate "good" vs. "bad" transport properties, it is crucial also to consider whether the carrier transport properties were measured by methods used for a single crystal or a polycrystalline material, as well as whether the direction of transport was measured concerning structural anisotropy. When considering the modulation of 2D perovskite performance, it is essential not to focus solely on

a single parameter, as this may lead to overlooking other essential factors and unexpected outcomes.

In summary, this section discusses the effects of the structure and interlayer spacing, inorganic layer thickness, differences in dielectric properties between different layers, film orientation, and phase distribution on the electronic structure and optical properties of 2D perovskites. The metal-halide-metal bond angle within the inorganic layers and the interlayer spacing influence the electronic structure and interlayer charge transport in 2D perovskites. Nevertheless, organic spacer cations can interact with halide atoms in the inorganic layers, altering the crystal structure of 2D perovskites and indirectly affecting the material's optical properties. The inorganic layer thickness can be controlled by varying the stoichiometric ratio between A' and A-site cations. Changing the thickness influences the quantum and dielectric confinement effects in 2D perovskites, thereby affecting the E_b. Therefore, the design of the composition and selection of inorganic layer thickness in 2D perovskites provide feasible approaches to optimize the optoelectronic performance of the device. Further details regarding these aspects will be elaborated in subsequent sections.

3.3. Characterization of Highly Anisotropic Carrier Transport

As introduced above, the process of charge conduction primarily relies on the inorganic lattice of the perovskite, even though the organic cations also have an impact,[179] especially with structural and carrier transport anisotropy in 2D perovskites. This complexity in the design of and influence on charge transport behavior distinguishes 2D perovskite materials from traditional organic and inorganic semiconductors. Many experimental techniques have been used to study carrier transport in perovskites, but not all techniques measure the exact contributing figure of merit to "mobility." Some methods rely on devices built around the material; contacts are applied directly to a single crystal, and pulsed contactless methods are used to sample photo-induced carrier dynamics directly. In the same vein that multiple "probe-style" techniques exist, there is a great deal of time- and length-scale dependence on the extracted carrier transport properties. For example, many contact-based measurements rely on long-range transport (up to microns or millimeters and seconds to minutes timescale) across the entire material (multiple grains and interfacial boundaries, etc.). In contrast, contactless spectroscopies may only probe carrier dynamics at the femto-time and nano-length scales. To focus on the composition-structure-carrier transport relationship at the fundamental and mechanical level, this discussion focuses on n = 1 composition and a select group of contact and non-contact techniques for which carrier anisotropy have been evaluated. **Figure 6** shows

the measurement principle of the Space Charge Limited Current (SCLC) Technique,[208] Time-Resolved Terahertz Spectroscopy (TRTS),[39a] Time-Resolved Microwave Conductivity (TRMC) Method,[178, 209] Optical Pump-THz Probe Spectroscopy (OPTPS).[210] Due to mechanism variations, the testing methods for different mobilities can dramatically yield different mobility data for the same material (**Table 3**). Taking the comparison between steady-state and transient testing methods as an example, the transient methods often yield mobility values several times higher than the steady-state method due to the relaxation of charge carriers.[211] The differences in measured mobility caused by different methods can pose significant challenges in summarizing the underlying trends, a point that will be reiterated in the outlook section.

Mirroring the structural anisotropy in 2D perovskites, the anisotropic conductivity and carrier mobility vary along different crystallographic directions. When measured along the plane of the inorganic sheet, the conductivity and mobility are much better than that measured perpendicular to the sheets. Although x-ray diffraction methods can assist in indexing the phase orientations of a perovskite sample (i.e., knowing how to orient the structural anisotropy relative to the measurement direction), there can be significant challenges for measuring charge transport with contacted methods in non-oriented single crystals and films, especially when contacts and application of large bias voltages are required. Due to the dual nature of perovskite materials as electronic and ionic conductors, the movement of ions within the perovskite strongly influences the current-voltage characteristics of single-charge carrier devices.[212] Therefore, when considering techniques such as SCLC, the impact of ions on charge transport must be considered, which adds complexity to the analysis. **Figure 6a** shows the contact orientation relative to the perovskite layering structure to probe in and out-of-plane conductivities.[213] TRTS can selectively monitor photo-generated charge carriers and concurrently measure their mobility. Besides, it can be achieved by varying the material's different tilt angles relative to the terahertz field to measure in-plane/out-of-plane mobility (**Figure 6b**).[39a] TRMC is suitable for studying charge carrier dynamics in perovskite films. Mobility in different directions can be measured by orienting the film parallel or perpendicular to the electric field of the microwaves (**Figure 6c**). The advantage of OPTPS lies in its heightened sensitivity to free charge carriers, diminishing the impact of charge trapping and excitons on mobility measurements, thereby endowing it with superior accuracy.[214]
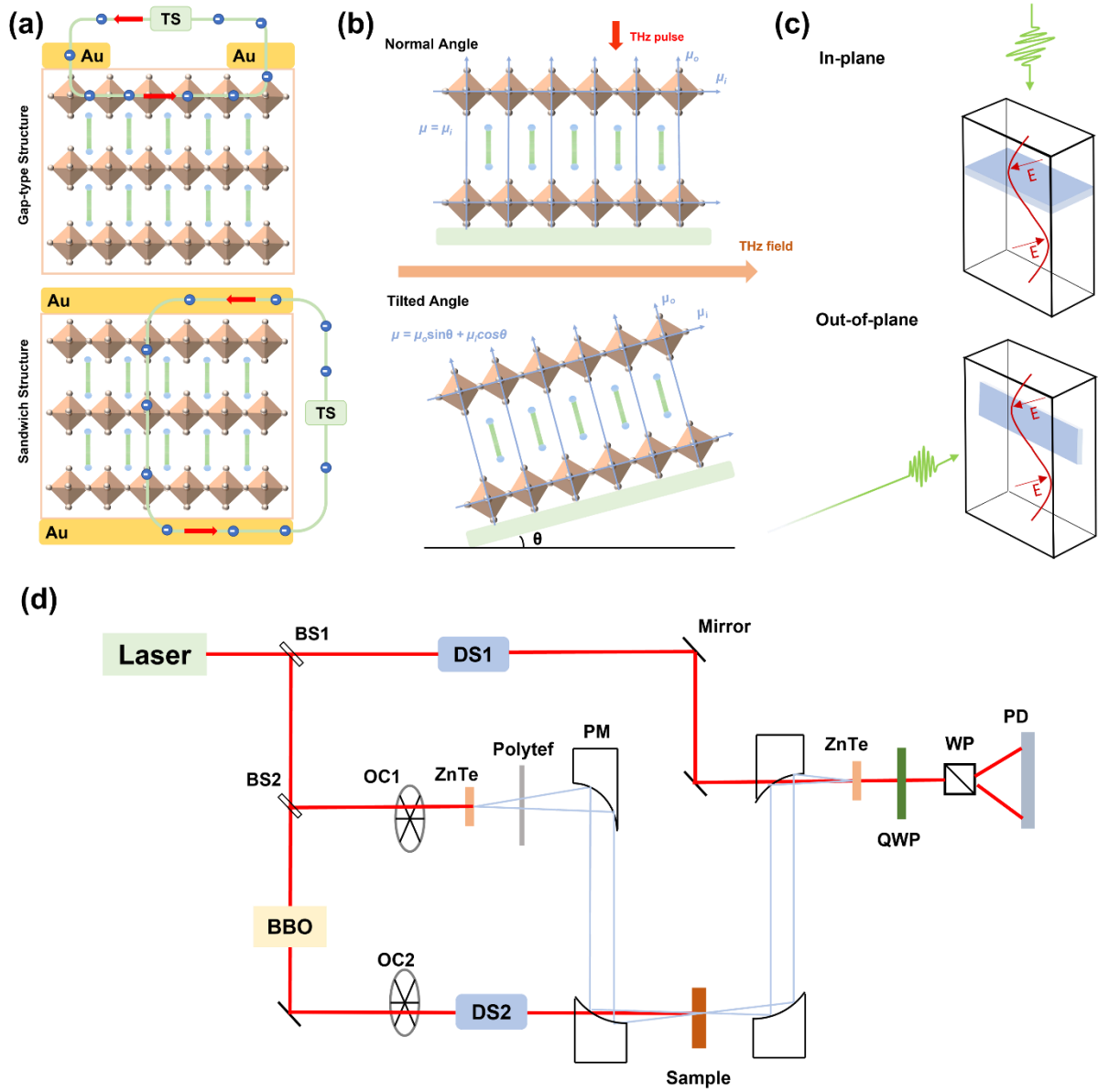
Figure 6. (a) Two device structures used for SCLC testing, the gap-type and the sandwich structures, correspondingly associated with in-plane/out-of-plane mobility measurements. (b) During TRTS testing, by tilting the device and aligning it with the THz pulse at a certain angle, in-plane/out-of-plane charge mobility is measured respectively. (c) In TRMC, two distinct testing modes correspond to the measurement of in-plane/out-of-plane charge mobility when 2D perovskite grows parallel to the substrate, where the microwave field distribution is depicted in red, the sample device in blue, and the photoexcitation in green. (d) A simplified optical schematic of the OPTPS testing system. BS: beam splitter, DS: delay stage, OC: optical chopper, PM: parabolic mirror, QWP: quarter wave plate, WP: Wollaston prism, PD: photodetector, BBO: Beta-Barium Borate crystal.

Table 3. Various methods for testing charge carrier mobility are applied in perovskite materials, where 'e' and 'h' represent electron and hole mobilities, respectively, and 'i' and 'o' denote in-plane and out-of-plane mobilities, respectively.

Composition	Architecture	Technique	Mobility $(cm^2 \cdot V^{-1} \cdot s^{-1})$	Ref.
MAPbI$_3$	Films	SCLC	$\mu_h = 2.89 \times 10^{-3}$	[215]
		TRTS	$\mu_e = 12.5$ $\mu_h = 7.5$	[216]
		OPTPS	35	[217]
			25	[179]
	Single crystal	SCLC	$\mu_{e,\,i} = 1.16$	[218]
			$\mu_h = 410$	[219]
			$\mu_e \approx \mu_h = 67.2$	[220]
FAPbI$_3$	Films	SCLC	1.3	[221]
		OPTPS	27 ± 2	[222]
	Single crystal	SCLC	$\mu_h = 35 \pm 7$	[223]
			4.4	[224]
(BA)$_2$PbI$_4$	Films	SCLC	$\mu_o = 4.7 \times 10^{-3}$ $\mu_i = 8.2 \times 10^{-2}$	[225]
		OPTPS	$\mu_o = 1.4 \times 10^{-4}$ $\mu_i = 0.54$	[226]
		TRMC	$\mu_o = (1 \sim 40) \times 10^{-4}$	[227]
(PEA)$_2$PbI$_4$	Films	TRMC	$\mu_o = (1 \sim 2000) \times 10^{-5}$ $\mu_i = 0.04 \sim 0.2$	[227]
		TRTS	5.8	[228]
		OPTPS	$\mu_{in} = 1$	[179]

$(F\text{-}PEA)_2PbI_4$	Films	TRMC	$\mu_o = (1 \sim 3000) \times 10^{-5}$ $\mu_i = 0.02 \sim 0.04$	[227]
$BDAPbI_4$	Single crystal	SCLC	$\mu_h = 17$	[229]
HA_2PbI_4	Films	SCLC	$\mu_o = 2.7 \times 10^{-4}$	[226]
		OPTPS	$\mu_i = 1.49$	
OA_2PbI_4		SCLC	$\mu_o = 2.2 \times 10^{-4}$	
		OPTPS	$\mu_i = 1.1$	
DA_2PbI_4		SCLC	$\mu_o = 8.3 \times 10^{-5}$	
		OPTPS	$\mu_i = 0.89$	
DDA_2PbI_4		SCLC	$\mu_o = 6.1 \times 10^{-5}$	
		OPTPS	$\mu_i = 0.82$	
ODA_2PbI_4		SCLC	$\mu_o = 7.2 \times 10^{-6}$	
		OPTPS	$\mu_i = 0.45$	
$(DSDEA)MA_4Pb_5I_{16}$	Films	SCLC	$\mu_h = 1.37 \times 10^{-5}$	[215]
$(HDA)MA_4Pb_5I_{16}$	Films	SCLC	$\mu_h = 2.09 \times 10^{-6}$	[215]
$BA_2(MA)_3Pb_4I_{13}$	Films	SCLC	$\mu_e = 5.64 \times 10^{-2}$ $\mu_h = 5.31 \times 10^{-2}$	[230]
			$\mu_e = (4.44 \sim 6.68) \times 10^{-2}$ $\mu_h = (0.66 \sim 5.09) \times 10^{-2}$	[231]
			$\mu_e \approx \mu_h = 1.2 \times 10^{-4}$	[207]
		TRTS	$\mu_o < 0.01$ $\mu_i = 1.88$	[232]
$BA_2MA_2Pb_3I_{10}$	Single crystal	SCLC	$\mu_o = 3.2 \times 10^{-5}$ $\mu_i = 9.6 \times 10^{-3}$	[233]

$(BA)_2(MA)_4Pb_5I_{16}$	Films	SCLC	$\mu_o = 6.6$ $\mu_i = 15.3$	[225]
$(iso\text{-}BA)_2(MA)_3Pb_4I_{13}$	Films	TRTS	$\mu_o = 1.35$ $\mu_i = 0.38$	[232]
$PEA_2MA_2Pb_3I_{10}$	Single crystal	SCLC	$\mu_o = 1.2 \times 10^{-5}$ $\mu_i = 4.4 \times 10^{-2}$	[233]
			8.23×10^{-3}	[234]
$(PEA)_2MA_3Pb_4I_{13}$	Single crystal	SCLC	3.61×10^{-2}	[234]
	Films	OPTPS	6	[179]
		SCLC	$\mu_h = 7.76 \times 10^{-3}$	[235]
$(PEA)_2MA_4Pb_5I_{16}$	Films	TRMC	7	[227]
	Single crystal	SCLC	8.56×10^{-3}	[234]
$(PEA)_2MA_{n-1}Pb_nI_{3n+1}(n = 2 \sim 3)$	Films	OPTPS	$\mu_i = 6 \sim 11$	[179]
$PEA_2MAPb_2I_7$	Single crystal	SCLC	4.59×10^{-3}	[234]
$(F\text{-}PEA)_2MA_4Pb_5I_{16}$	Films	TRMC	9	[227]
$(PDA)MA_3Pb_4I_{13}$	Films	SCLC	$\mu_e \approx \mu_h = 3.8 \times 10^{-4}$	[207]
$ALA_2MA_2Pb_3I_{10}$	Single crystal	SCLC	$\mu_o = 1.3 \times 10^{-5}$ $\mu_i = 2.4 \times 10^{-2}$	[233]

4. Strategies to Improve the Charge of Transport

The previous description of factors influencing transport performance reveals that each component of 2D perovskite plays a significant role in transport charge. Specifically, by selecting different A'-site organic spacer cations, A-site cations, B-site metal cations, and X-site halide ions, it is possible to effectively tune the bandgap of 2D perovskite, thereby influencing the light absorption range and ultimately improving the charge transport properties.

4.1. A'-Site Organic Spacer Cations

The impact of organic spacer cations on the crystal and electronic structure of 2D perovskites is significant and should not be overlooked. So far, the vast majority of research devoted to structure-property relationships in 2D perovskites has focused on correlating band gap with octahedral tilt and disorder factors,[114a] in addition to Pb-I bond lengths and especially through-space distances between I atoms in the out-of-plane direction.[236] Besides, the quantum well barrier width reduction, also known as interlayer spacing between metal-halide sheets, has been proposed theoretically and demonstrated experimentally to improve charge extraction.[124c]

The influence of spacer cations on 2D perovskites mainly stems from differences in geometric shape, structural rigidity, conjugation properties, and ε_r. These differences correspond to the inorganic layer structure, interlayer spacing, interactions, and quantum confinement and dielectric confinement effects in 2D perovskites. All these factors have implications on the generation, transport, and extraction efficiency of charges in photovoltaic devices, thereby playing a crucial role in the optoelectronic performance of these devices. In the following discussion, we will discuss the impact of the spacer cations molecular design on the charge transport properties.

4.1.1. Functional Groups and Heteroatoms

The variety of functional groups contributes to the diversity of interlayer cations in 2D perovskites, as different functional groups exert distinct influences on the structure and performance of these materials. Specific functional groups can modulate the interlayer spacing in 2D perovskites, enhancing interlayer charge transfer. They can also form unique intramolecular interactions with the interlayer cations, affecting the crystalline structure of the perovskite. In addition to different types of functional groups, the position of the functional group (ammonium moiety) within the interlayer cation significantly impacts the photoelectric properties of the perovskite. The diverse spatial effects resulting from different positions of the

ammonium moiety give rise to varying interactions between the interlayer cations and the inorganic layers, consequently influencing the crystal structure of the perovskite. The heteroatoms in the interlayer cations often strengthen intermolecular interactions, thereby improving the photoelectric performance of 2D perovskites.
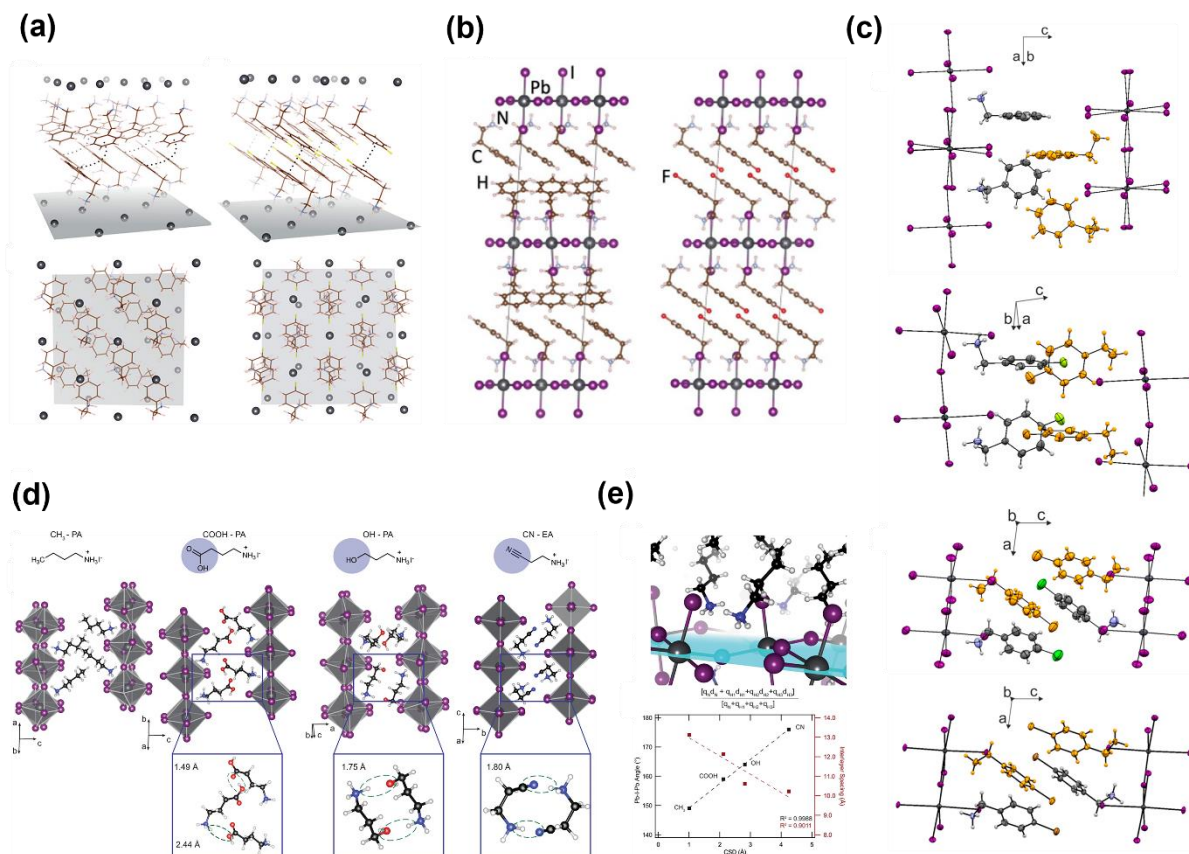
Figure 7. (a, b) The single-crystal structures and optimized atomic structures of (PEA)$_2$PbI$_4$ and (F-PEA)$_2$PbI$_4$. Reproduced with permission.[178] Copyright 2019, American Chemical Society. (c) Effect of halogen substituents on cation arrangement within the spacer. Reproduced with permission.[166] Copyright 2020, American Chemical Society. (d) Schematic crystal structures of four organic spacer cations and the corresponding perovskites. (e) Schematic diagram of calculated CSD and variation of average Pb-I-Pb bond angle and layer spacing with CSD. Reproduced under terms of the CC-BY license.[39b] Copyright 2022, Xiaoming Zhao et al., published by Springer Nature.

Due to the exclusion of the inorganic layer's influence on the intrinsic properties of 2D perovskite, 2D perovskites with n = 1 are often employed for mechanistic studies on the impact of spacer cations on the transport performance of perovskites. Zhang *et al*. introduced fluorine atoms as substituents at the para position of phenethylammonium (PEA$^+$).[178] Compared to (PEA)$_2$PbI$_4$, (F-PEA)$_2$PbI$_4$ exhibited faster charge transfer, longer carrier lifetimes, and lower trap density. In (F-PEA)$_2$PbI$_4$, the phenyl rings in the interlayer were stacked face-on, whereas

in (PEA)$_2$PbI$_4$, the phenyl rings were face-to-edge stacked (**Figure 7a, b**). The distinct stacking modes led to a shorter distance between interlayer cations, resulting in positional differences in the inorganic layers. In PEA, the ammonium moieties on both ends of the organic layer were offset due to the face-to-edge stacking. As a result, the Pb centers in the adjacent inorganic layers also staggered. In contrast, the terminal ammonium moieties overlapped approximately in the vertical direction for F-PEA, leading to almost overlapping lead atoms in the adjacent inorganic layers. This configuration in F-PEA facilitated better interlayer electronic coupling, thus improving carrier transport.

Schmitt *et al*. investigated the influence of halogen substituents in intercalated cations on the crystal structure of corresponding perovskites.[166] The results indicated that introducing halide ions reduced the crystal symmetry, with the extent of the changes depending on the differences in interactions between the intercalated cations. As shown in **Figure 7c**, in (BzA)$_2$PbI$_4$, the benzylammonium cations oriented themselves perpendicular to each other, forming edge-to-face C-H$\cdots\pi$ interactions. (4-FBzA)$_2$PbI$_4$ exhibited a similar edge-to-face arrangement as (BzA)$_2$PbI$_4$, but with different orientations in the interlayer. However, for (4-ClBzA)$_2$PbI$_4$ and (4-BrBzA)$_2$PbI$_4$, the intercalated cations did not align perpendicularly to accommodate Cl/Br$-\pi$ interactions, resulting in the loss of centrosymmetric crystal structures in the corresponding perovskites. Compared to the previous two cases, these structural differences were influenced by the size and electronegativity of the halogen substituents. In addition to the changes in crystal symmetry, the different orientations of halogens in the intercalated cations also caused subtle variations in the positions and orientations of the ammonium groups, leading to distortions in the inorganic layer framework. Compared to the previous two cases, the latter exhibited greater in-plane distortion, resulting in larger band gaps and poor charge carrier transport performance.

Zhao *et al*. conducted a study to investigate the effects of different functional groups on intercalated cations.[39b] (OH-PA)$_2$PbI$_4$ and (CN-EA)$_2$PbI$_4$ formed dimers within the interlayer region, while COOH-PA$^+$ did not form dimers due to its larger size and instead exhibited a "molecular zipper" arrangement (**Figure 7d**). As previously discussed, the electronic band structure and charge transport properties of 2D perovskites were closely related to the Pb-I-Pb bond angles and interlayer distances within the inorganic framework. The formation of dimers originated from the strong intermolecular interactions between the interlayer cations' non-amine and amine ends, resulting in unique in-plane coupling. The non-amine end pulled the amine end out of the inorganic layers, effectively reducing the interaction between the amine end and equatorial iodides and minimizing distortion in the Pb-I-Pb bond angles. This

phenomenon ultimately led to improved optoelectronic performance. Furthermore, the Charge Separation Descriptor (CSD) was utilized to quantify the degree of separation between the Bader charge centers of the ammonium cations and the inorganic plane. There was a strong correlation between CSD and the structure and performance of the 2D perovskite (**Figure 7e**). The highest CSD corresponded to the least distorted Pb-I-Pb bond angles and the smallest interlayer distance. The largest Pb-I-Pb bond angles and the smallest interlayer distance contributed to reduced bandgap and enhanced charge carrier mobility. Hence, a higher CSD value indicated better photoelectric performance of the 2D perovskite.
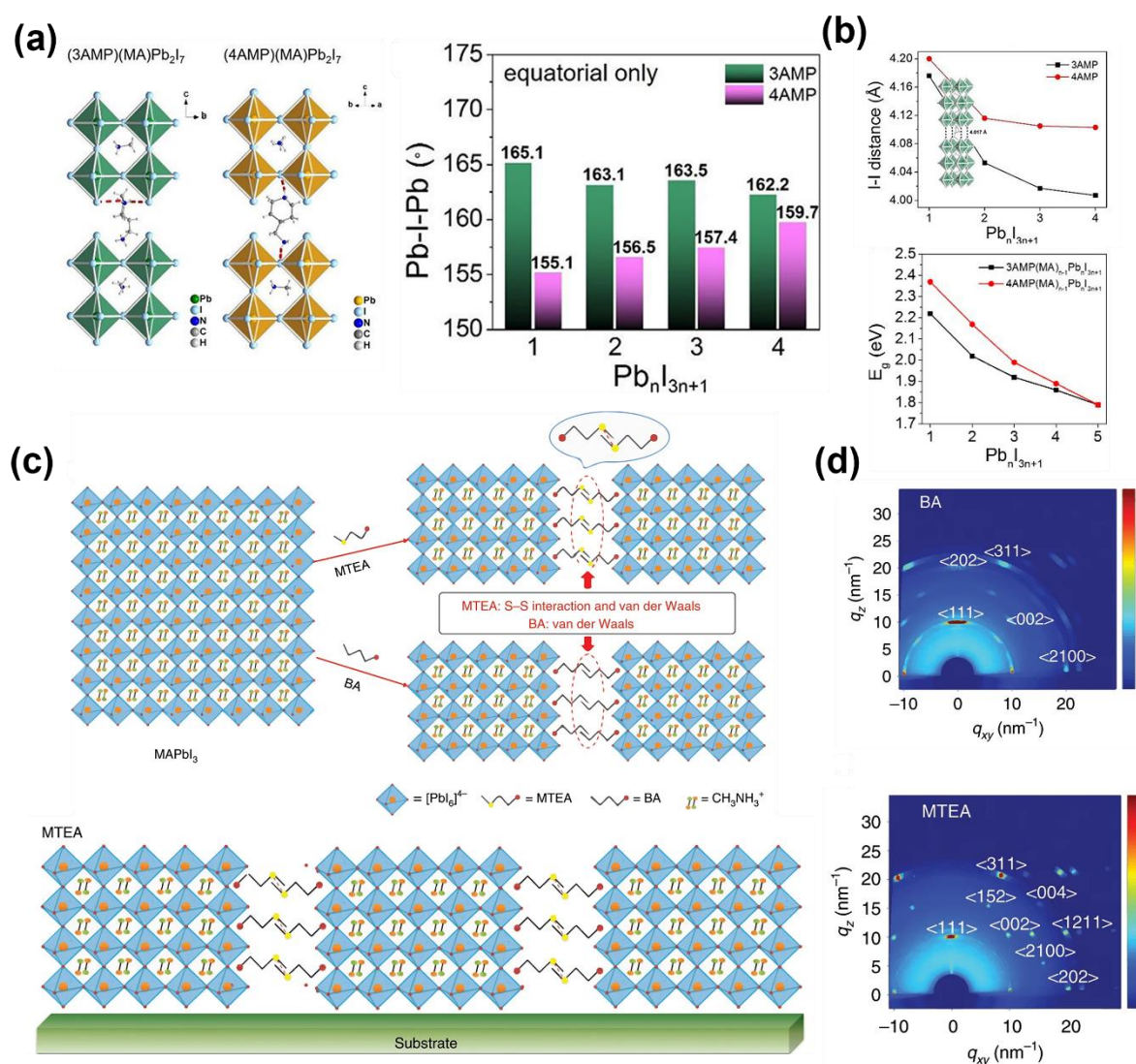
Figure 8. (a) Effect of functional group position of spaced cations on crystal structure and average equatorial Pb-I-Pb angle. (b) Line graph of I···I distance and bandgap energy as a function of the value of n. Reproduced with permission.[28b] Copyright 2018, American Chemical Society. (c) Effect of S-S interactions in spaced cations on film growth. (d) GIWAXS patterns of 2D perovskite films. Reproduced under terms of the CC-BY license.[52] Copyright 2020, Hui Ren et al., published by Springer Nature.

Interlayer cations also influence quasi-2D perovskites (1 < n < 5). Mao *et al.* investigated the impact of the functional group's position on the interlayer cations on the structure and performance of 2D perovskites.[28b] The crystal structure diagram of the perovskite revealed that 3-(aminomethyl)piperidinium (3AMP) cations primarily form hydrogen bonds with the terminal I atoms of the inorganic layers. In contrast, 4-(aminomethyl)piperidinium (4AMP) cations form hydrogen bonds with the bridging I atoms (**Figure 8a**). Since the variation in bridging I atoms was the primary cause of distortion within the inorganic octahedral layers, the 4AMP perovskite exhibited a more distorted octahedral lattice and smaller equatorial Pb-I-Pb bond angles. Furthermore, the different interaction sites between interlayer cations and the inorganic layers resulted in variations in the arrangement of cations within the interlayer, likely contributing to forming a smaller interlayer distance in the 3AMP perovskite (**Figure 8b**). Karabag *et al.* investigated the influence of different substituents at various positions on the benzene ring on the lattice of 2D perovskites.[237] Ortho-substituents and para-substituents elongated the inorganic layer's Pb-I bonds and partially broke Pb-I bonds. In the case of meta-substitution, the distribution of Pb-I bonds was the most uniform, leading to optimal polarization migration and conductivity.

The impact of heteroatoms in interlayer cations should not be overlooked. Ren *et al.* synthesized 2D perovskites using 2-(methylthio)ethylammonium ($MTEA^+$) and BA^+ as interlayer cations.[52] It could be observed that, compared to BA^+, in the interlayer, there were additional S-S interactions between the two layers of $MTEA^+$ alongside van der Waals forces (**Figure 8c**). The MTEA-based perovskite film exhibited sharper and more distinct Bragg peaks (**Figure 8d**), and the inorganic sheet growth in the film was perpendicular to the substrate, a characteristic that aided in the formation of continuous charge transport pathways and enhanced carrier mobility perpendicular to the plane of the substrate. The superior vertical orientation could be attributed to the additional S-S interactions in MTEA, which contributed to stabilizing and tightening the perovskite framework, thereby enabling the vertical growth of the film.

4.1.2. Aromatic and Other Unsaturated Structures

Quantum and dielectric confinement effects significantly impact the optoelectronic properties of 2D perovskites. Intercalated cations with aromatic groups exhibit a higher ε_r, reducing the dielectric mismatch between the inorganic and organic layers. This mitigates the influence of dielectric confinement, leading to a decrease in the electronic bandgap and E_b of 2D perovskites. Additionally, intercalated cations with aromatic groups often possess higher structural rigidity, which alters the lattice stiffness of 2D perovskites. This change can affect

the vibrational frequency and modes of the lattice, thereby impacting the interaction between electrons and lattice vibrations. Electron-phonon coupling influences the bands' shape and energy level distribution, thereby altering the energy gap between the conduction and valence bands. Moreover, electron-phonon coupling also affects energy transfer and scattering processes between electrons and phonons, further influencing the transport properties of charge carriers.
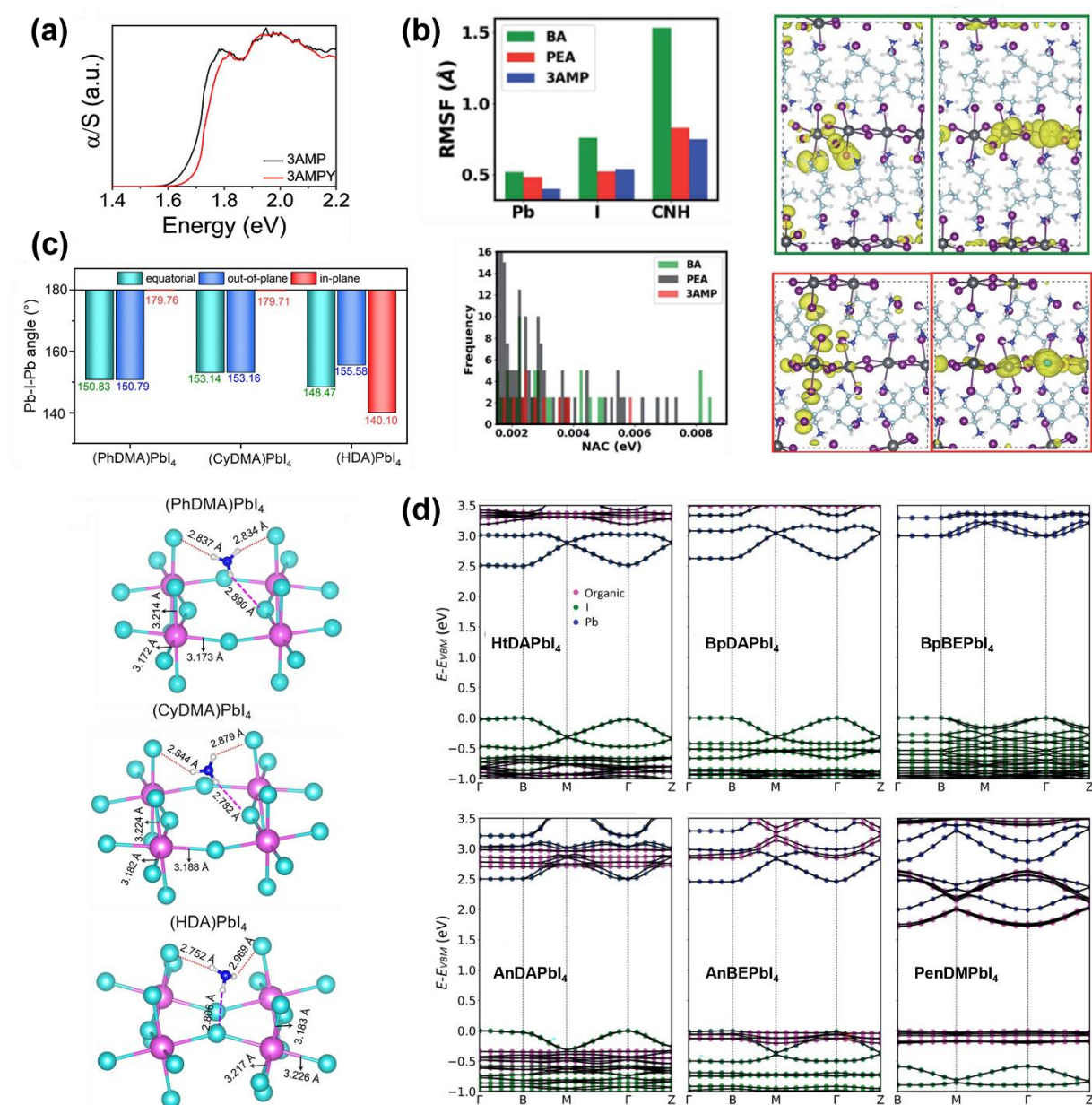
Figure 9. (a) Absorption spectroscopy is used to compare the effects of aromatic rings on 2D perovskites. Reproduced with permission.[128] Copyright 2019, American Chemical Society. (b) The root mean square fluctuations for Pb, I, and organic spacers at 300 K, the contribution of each component to VBM and CBM, and the NAC plot were used to determine non-radiative recombination. Reproduced with permission.[124c] Copyright 2020, Royal Society of Chemistry. (c) Comparison of Pb-I-Pb bond angles of three perovskites and effects of hydrogen bonding

between different types of iodine atoms in amino and inorganic layers. Reproduced with permission.[114a] Copyright 2023, Elsevier. (d) The variation trend of perovskite electron band structure concerning increasing cation conjugation. Reproduced with permission.[122b] Copyright 2021, John Wiley and Sons.

Li *et al*. conducted a comparative analysis of the photoelectric performance disparities between (3AMP)(MA)$_3$Pb$_4$I$_{13}$ and (3AMPY)(MA)$_3$Pb$_4$I$_{13}$ (3AMPY = 3-(aminomethyl)pyridinium), hereafter referred to as 3AMP and 3AMPY, respectively.[128] While the high-energy band slopes in the ultraviolet absorption spectra appeared similar, excitonic peaks resulted in distinct slopes at lower energy levels. Notably, 3AMPY exhibited a smaller E_b compared to 3AMP, thereby favoring the effective separation and collection of electron-hole pairs in the device. This lower E_b could be attributed to the higher ε_r of the aromatic intercalating cations, as opposed to alkylammonium cations. The existence of delocalized π electron clouds on the aromatic rings reduced the dielectric mismatch between the inorganic and organic layers, consequently weakening the corresponding dielectric confinement effect in the QWs structure of the 2D perovskite.

In addition to the influence of ε_r, aromatic intercalated cations also increase the crystal rigidity of 2D perovskites and reduce the electron-phonon coupling to achieve enhanced charge carrier mobility. Ghosh *et al*. investigated the root mean square fluctuations (RMSF) of different intercalated cations (**Figure 9b**).[124c] It could be observed that BA-based 2D perovskite exhibited the most significant structural volatility in terms of Pb, I atoms, and intercalated cations, while PEA-based was significantly more stable. This was because the π-π interactions between aromatic rings in PEA-based significantly enhanced the structural rigidity of the organic layer, thereby restraining their thermal motion and minimizing the thermal motion of I atoms in the inorganic layer. The histogram of instantaneous non-adiabatic coupling constants (NAC) was used to reflect the degree of nonradiative recombination in 2D perovskites. NAC could quantify the scattering strength of the recombined charges, and higher NAC values corresponded to more nonradiative recombination. The strength of NAC depended on the degree of wavefunction overlap. A more substantial wavefunction overlap led to higher phonon velocity and larger NAC values. In the case of 2D perovskites, where the VBM and CBM were confined within the inorganic framework, thermal fluctuations at the Pb and I sites directly influenced the fluctuation of wavefunction overlap. Therefore, the higher structural fluctuations at the Pb-I sites in (BA)$_2$PbI$_4$ resulted in a frequent occurrence of higher NAC values. Furthermore, in (3AMP)PbI$_4$, the more delocalized charge density at the band edges indicated a weaker overlap between the VBM and CBM. Specifically, the shorter axial distance to the I

atoms created a unique pathway for charge delocalization from the VBM, weakening the wavefunction overlap and resulting in smaller NAC values and reduced nonradiative recombination.

Liu *et al*. compared 2D perovskites with different alkyl chains, alkyl rings, and aromatic group intercalated cations, each possessing low, medium, and high rigidity, respectively.[114a] Among them, the (CyDMA)PbI$_4$ and (PhDMA)PbI$_4$ with stronger rigid cations exhibited better structural stability and reduced inorganic layer distortion (**Figure 9c**). This could be attributed to the appropriate rigidity of the intercalated cations, which support the inorganic layer framework and mitigate distortion. Furthermore, the moderately rigid (CyDMA)PbI$_4$ demonstrated greater flexibility in adjusting its structure to accommodate the inorganic framework, resulting in minor lattice strain, reduced Pb-I-Pb bond angle distortion, and a smaller bandgap. In addition to the rigidity of the intercalated cations, the Pb-I-Pb bond angle was also influenced by hydrogen bonding sites. In these 2D perovskites, three hydrogen bonds were formed between the amino group and the inorganic layer. Two of these bonds were between H and terminal I atoms, while the third was between H and bridging I atoms. The second hydrogen bond was formed in the moderately and highly rigid CyDMA^{2+} and PhDMA^{2+} cations with bridging I adjacent to terminal I. In contrast, HDA^{2+} formed a hydrogen bond with the bridging I in the opposite direction. This led to a more pronounced distortion of the [PbI$_6$]$^{4-}$ octahedra and greater Pb-I-Pb bond angle distortion.

The choice of intercalated cations significantly influences the electronic band structure of perovskite materials. Typically, when non-conjugated alkyl compounds are employed as intercalated cations, their frontier molecular orbitals (MOs) lie away from CBM and VBM of the perovskite inorganic layer, forming a type I heterojunction interface between the interlayer and inorganic layer. Charge separation/recombination and transfer processes occur exclusively within the inorganic layer framework. In contrast, utilizing intercalated cations with aromatic or other unsaturated structures possessing π-conjugation results in an evolution of the energy level alignment between the interlayer MOs and the band edges of the inorganic layer, depending on the degree of π-conjugation of the intercalated cations. Dai *et al*. investigated how the polarizability or conjugation length of the intercalated cations influences the hybridization of wave functions and electron coupling between the interlayer MOs and the band edges of the inorganic layer.[122b] The band structures, computed using HSE+SOC calculations, revealed that as the degree of conjugation increases, HOMO/LUMO of the interlayer lying progressively lower/ higher in energy than the VBM/CBM of the inorganic layer and approaching closer to them (**Figure 9d**). In contrast, the highly conjugated PenDM displayed

WILEY-VCH

HOMO and LUMO levels positioned above and below the VBM and CBM of the perovskite inorganic layer, resulting in a smaller bandgap.

In summary, dielectric confinement and structural design freedom are constrained by properties typically associated with conjugated ring organic cations. Additionally, the ability to induce intentional organic and inorganic lattice band mixing may be a worthwhile tradeoff for lowering the bandgap of 2D perovskites while also improving anisotropic carrier transport.

4.1.3. Carbon Chain Length and Branched Chains

From a molecular design perspective, the carbon chain length of the spacer cation and the presence of branched chains can alter its spatial effects, thereby influencing the interlayer spacing of the inorganic layers in 2D perovskites and the orientation and phase distribution of the thin films. The primary result of increasing carbon chain length is increased distance between inorganic sheets. This allows for the modulation of the material's electronic band structure and alters its charge transport properties and carrier generation yield.
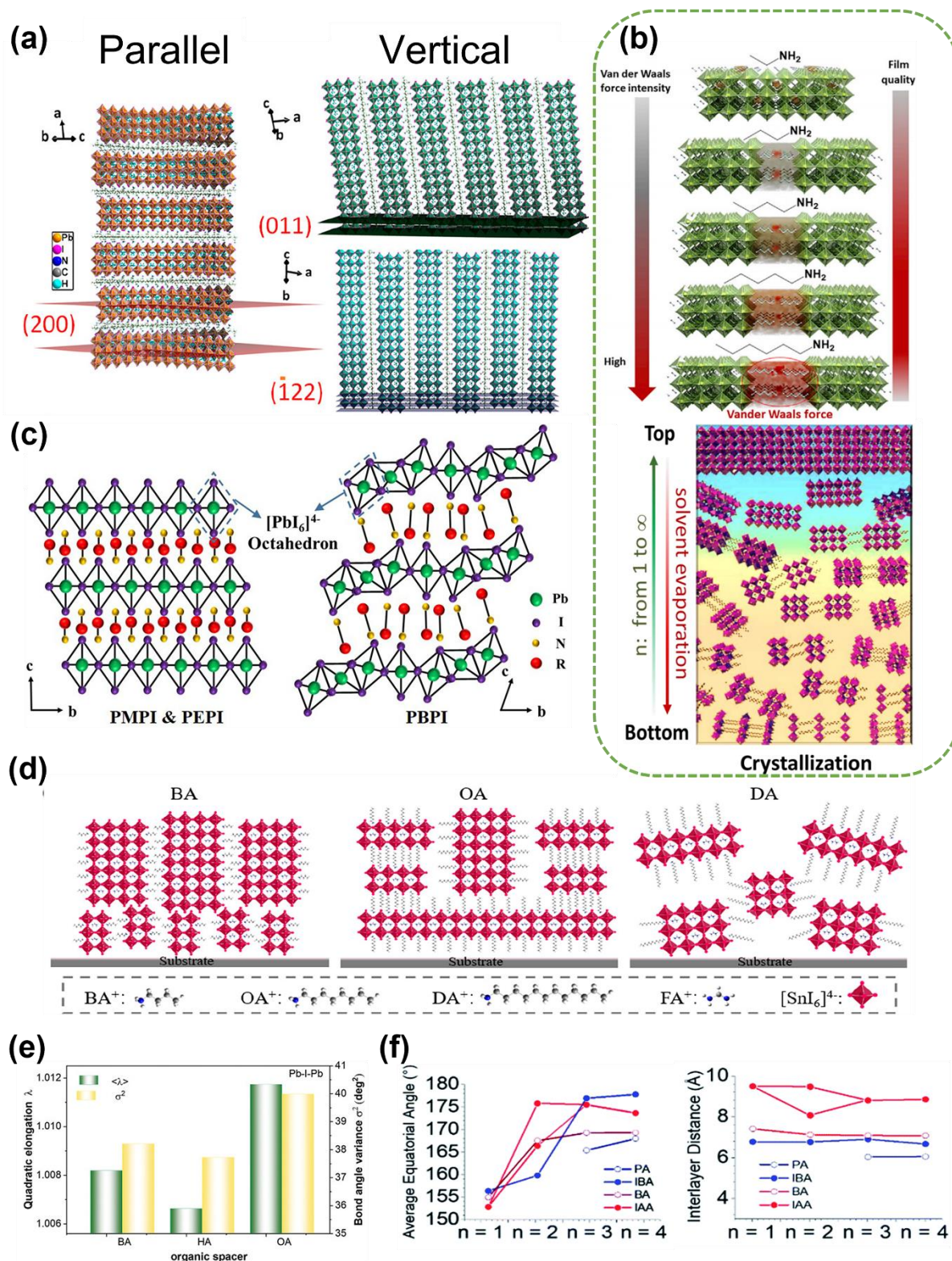
Figure 10. (a) Parallel and vertical orientation in 2D perovskite films. Reproduced with permission.[115] Copyright 2018, American Chemical Society. (b) Van der Waals forces and film mass with organic spacer cation chain length trend plot and phase distribution in 2D perovskite films. Reproduced with permission.[37] Copyright 2021, Elsevier. (c) Spaced cations with different chain lengths correspond to the crystal structure of 2D perovskites. Reproduced with permission.[238] Copyright 2017, American Chemical Society. (d) Schematic illustration

of crystal orientation, dimensionality, and phase distribution of 2D perovskite films. Reproduced with permission.[239] Copyright 2020, American Chemical Society. (e) Effect of spacer cation chain length on Pb-Pb bond length quadratic elongation ($\langle\lambda\rangle$) and bond angle variance (σ) of Pb-I-Pb bonds. Reproduced under terms of the CC-BY license.[240] Copyright 2023, Xudong Yang et al., published by John Wiley and Sons. (f) Schematic variation of the average equatorial angles and the interlayer spacing for branched and straight-chain amines with the value of n. Reproduced under terms of the CC-BY license.[54] Copyright 2020, Justin M. Hoffman et al., published by Royal Society of Chemistry.

In 2018, Li *et al*. investigated the impact of interlayer cations with different carbon chain lengths on the orientation of perovskite thin films.[115] **Figure 10a** illustrates two orientations within the 2D perovskite thin films: parallel and vertical. The overall transport performance of the device was determined by the charge transport within the inorganic layer due to the insulation property of the spacing cation layer. Therefore, perovskite thin films grown vertically to the substrate are more favorable for enhancing the optoelectronic properties of the devices. The orientation of the 2D perovskite thin films in the same series is primarily influenced by the chain length of the spacing cations. Increasing the carbon chain length of the spacing cations within a certain range leads to gradual improvements in the film's orientation and crystallinity, with a preference for the inorganic layer to arrange vertically relative to the substrate. This plays a crucial role in enhancing the optoelectronic performance of 2D perovskites by allowing effective charge transfer through the conductive inorganic layer without hindrance from the insulating organic layer.

The chain length of interlayer cations also impacts the crystalline quality of 2D perovskite films, thus influencing the optoelectronic performance of devices. Wu *et al*. demonstrated through DFT calculations that an increase in chain length enhances the van der Waals forces between interlayer cations, significantly promoting the aggregation of perovskite precursors and improving the crystalline quality of the 2D RP perovskite films (**Figure 10b**).[37] This also accelerated the growth of 3D-like components, promoted phase separation, and led to the overall thickening of the perovskite film. Among this series of 2D perovskites, the AA-based (pentylamine) 2D perovskite demonstrated the best crystal orientation. This was attributed to AA-based having the most suitable molecular interactions and optimal precursor aggregation, facilitating the reduction of parallel orientations, thus enabling more efficient charge transfer across different n-value components. Additionally, compared to perovskites with BA^+, HA^+, and PA^+ as interlayer cations, the AA-based perovskite film exhibited a higher ε_r. This improvement in crystal orientation led to a more favorable alignment of dipoles along the

vertical direction, resulting in an increased macroscopic ε_r of the perovskite film. The increase in ε_r reduced the dielectric confinement of the 2D RP perovskite and facilitated the generation of free charge carriers, thereby enhancing the optoelectronic performance of the perovskite.

Paritmongkol *et al*. discovered that within the interlayer of 2D perovskites, a specific interaction existed between different organic interlayer cations.[241] This interaction induced stress within the layers, which can be transmitted to the inorganic layer through the carbon chains of the interlayer molecules, resulting in distortion of the inorganic octahedra. As the length of the organic interlayer increases, the stress was absorbed more by the longer carbon chains, leading to a reduction in stress transmitted to the $[PbI_6]^{4-}$ octahedra. Gan *et al*. found that when the organic interlayer cation is benzylamine or its derivatives, the crystal structure of the 2D perovskite undergoes a reorganization with increasing chain length of the interlayer cation, resulting in additional quantum confinement (**Figure 10c**).[238] In 2D perovskites with short-chain interlayer cations, the inorganic layer was predominantly composed of corner-sharing octahedra. However, for 2D perovskites with long-chain interlayer cations, the inorganic layer contained corner-sharing and face-sharing octahedra. Face-sharing octahedra induced additional constraint effects, leading to significant changes in the band structure.

The length of the carbon chain in the spacer cations affects the orientation properties of the perovskite films and their phase distribution. In 2020, Li *et al*. examined the impact of chain length on the crystal orientation and phase distribution of 2D tin-based perovskite films.[239] As depicted in **Figure 10d**, with increasing carbon chain length of the spacer cations, the distribution of high n-value phases shifted from the top to the bottom of the film, which hindered exciton dissociation and increased energy losses between different phases.

Zeng *et al*. investigated the influence of interlayer cations with different chain lengths on lattice distortion in perovskite crystals, where the carbon chain length of the interlayer cations ranged from butylammonium (BA^+) to octylammonium (OA^+).[240] In **Figure 10e**, the 2D perovskite with hexylaminium (HA^+) as the interlayer cation exhibited the smallest average Pb-Pb bond elongation rate ($<\lambda>$) and Pb-I-Pb bond angle variance (σ^2), indicating the minor lattice distortion. This could be attributed to the staggered arrangement of interlayer cations exerting shear forces on the octahedral Pb-I framework within the interlayer, which leads to varying degrees of lattice distortion in the inorganic layer. However, HA^+ with an appropriate chain length weakened these shear forces, suppressing lattice distortion. Hoffman *et al*. compared the structural and performance differences of 2D perovskites with straight-chain alkylammonium cations and branched alkylammonium cations as spacer cations (**Figure 10f**).[54] Compared to branched alkylammonium cations, the 2D perovskite structure prepared with straight-chain

alkylammonium cations exhibited greater distortion at higher n values. Spacer cations with branched chains had larger equatorial Pb-I-Pb bond angles. This can be attributed to introducing branches that provide larger steric hindrance, making it more difficult for the spacer cations to distort the inorganic layers. Less distortion in the inorganic layer framework contributed to better optoelectronic performance. Additionally, introducing branching in the organic cations increased the spacing distance between inorganic layers to accommodate larger organic cation sterics.

In summary, the vast molecular design space of the organic cation (sterics, heteroatom incorporation, valency, degree of conjugation, etc.) enables a profound degree of tailoring 2D perovskite optoelectronic properties. Due to the diverse range of interlayer cation species, elucidating their complex influence mechanisms on 2D perovskites is crucial. Taking the chain length analyzed in this section as an example, for alkyl chain-type interlayer cations, an appropriate increase in chain length helps improve the crystallinity and orientation of the film, alleviating the stress of organic layers on the inorganic framework. However, the increase in chain length typically leads to an increase in the interlayer spacing of the inorganic layers, inhibiting the out-of-plane charge transport of 2D perovskites. Therefore, to clarify this complex mechanism, future researchers should investigate all the nuances the organic layer length and impacts on the inorganic layer can have, with the specific goal of understanding carrier transport effects.

4.2. B-Site Metal Cations

Pb exhibits the broadest range of applications in perovskite materials compared to Sn and Ge. This can be attributed to the larger atomic radius of lead, which facilitates superior lattice matching and stability, thereby minimizing lattice defects and distortions. Furthermore, tin and germanium possess relatively poorer stability in their oxidized states than lead, making them prone to oxidation reactions that compromise the long-term stability of perovskite materials. Nevertheless, the environmental and health hazards of lead cannot be overlooked. Hence, research on lead-free or mixed-metal perovskite materials requires increased effort to balance performance and environmental considerations.
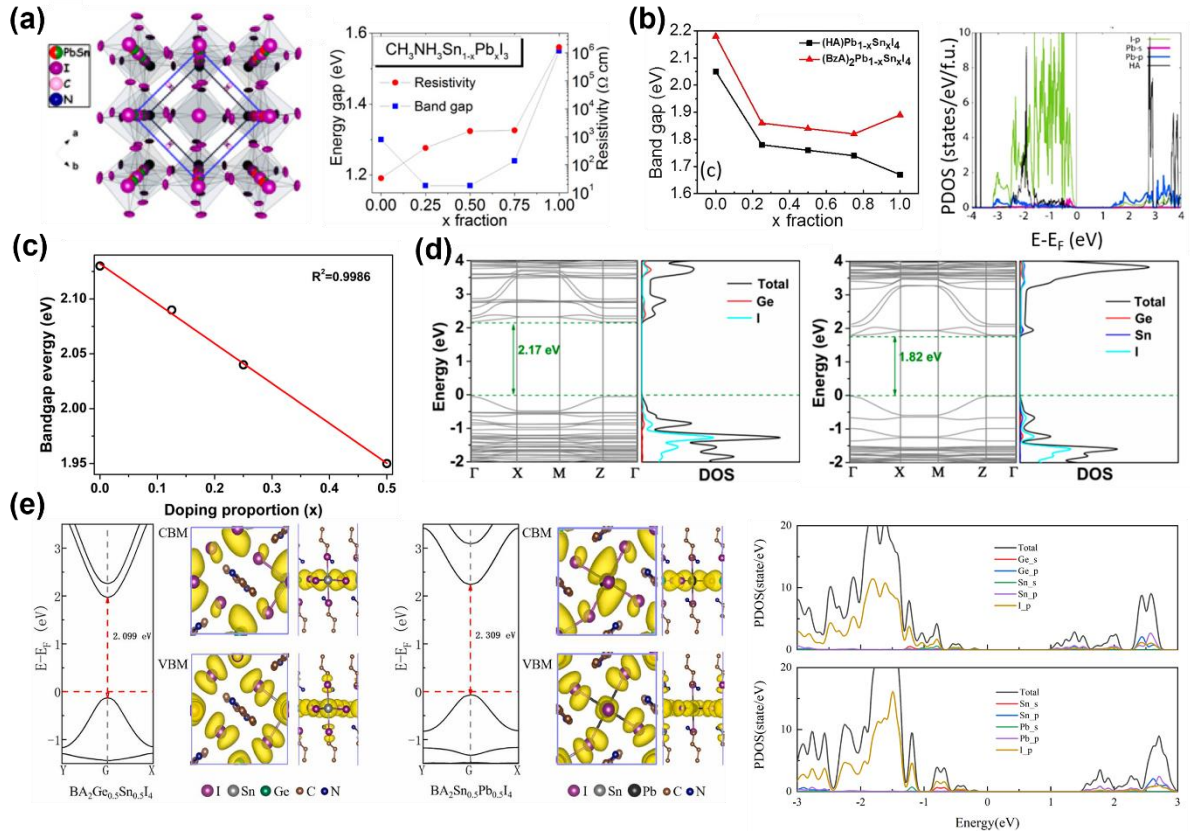
Figure 11. (a) 3D perovskite crystal structure diagram of mixed metal ions, band gap, and resistivity as a function of metal composition. Reproduced with permission.[242] Copyright 2014, American Chemical Society. (b) Line graph of bandgap energy variation and projected density of states (PDOS) of $(HA)Pb_xSn_{1-x}I_4$ and $(BZA)_2Pb_xSn_{1-x}I_4$ (x = 0, 0.25, 0.5, 0.75, 1). Reproduced with permission.[137] Copyright 2016, American Chemical Society. (c) Band gap energies with increasing values of x in $(PEA)_2Ge_{1-x}Sn_xI_4$. (d) The calculated band structure and DOS of $(PEA)_2GeI_4$ (up) and $(PEA)_2Ge_{0.5}Sn_{0.5}I_4$ (down). Reproduced with permission.[243] Copyright 2018, American Chemical Society. (e) The band structures and PDOS of $BA_2M_{0.5}Sn_{0.5}I_4$ (M = Ge/Pb). Reproduced with permission.[244] Copyright 2022, Elsevier.

Mixing metal ions at the B site in perovskites can alter their band structure. It can be observed that introducing Sn into 3D Pb-based perovskites led to a reduced bandgap (**Figure 11a**).[242] This change also provided a new avenue for 2D perovskites. Mao *et al.* incorporated a certain proportion of Sn metal ions into 2D perovskite films with varying interlayer cations.[137] In the $(HA)PbI_4$ and $(BZA)_2PbI_4$ systems, the addition of Sn led to a reduction in the bandgap (**Figure 11b**). However, this behavior deviated from the expected smooth dependence on Vegard's law. This strange phenomenon could be attributed to the antagonistic effect of SOC, which arose from the alloying of heavier Pb atoms with lighter Sn atom's structural deformations induced by phase transitions.

To further investigate the influence of metal Sn on 2D perovskites, Cheng *et al*. synthesized 2D halide perovskites with mixed metal atoms (Ge and Sn), with Sn content ranging from 0% to 50%.[243] It could be observed that the bandgap of the $(PEA)_2Ge_{1-x}Sn_xI_4$ system decreased gradually, following Vegard's law, as the Sn content increased (**Figure 11c**). Compared to $(PEA)_2GeI_4$, $(PEA)_2Ge_{0.5}Sn_{0.5}I_4$ exhibited greater dispersion at the top of the valence band and the bottom of the conduction band, indicating a smaller bandgap and improved carrier transport (**Figure 11d**). The LDOS exhibited the contribution of Sn, where in $(PEA)_2GeI_4$, the Ge^{2+} cations primarily contributed to the bottom of the conduction band. In contrast, I^- mainly contributes to the top of the valence band. The incorporation of Sn introduced new Sn^{2+}-derived valence and conduction bands, thereby significantly impacting the band structure of the perovskite.

Wang *et al*. studied the electronic band structures of 2D perovskites with mixed metal ions.[244] In the case of Ge-Sn mixed perovskites, the VBM was mainly composed of Ge 4p, Sn 5s, and I 5p orbitals, while the CBM was mainly composed of Ge 4p and Sn 5p orbitals, with a minor contribution from I 5p orbitals (**Figure 11e)**. Similar phenomena were observed in mixed Sn-Pb perovskites. The metal cations and halide anions contributed to the VBM and CBM, while the organic cations did not, which is consistent with typical 2D perovskites.

In summary, the electronic structure of perovskites can be adjusted by changing the composition of metal cations, thereby improving their optoelectronic performance. Furthermore, research on metal cations may be combined with studies on organic cations that exhibit orbital hybridization between organic and inorganic layers. It could be a route to offset the SOC effects of Pb-Sn compositions by compensating with structural offsets induced by the organic cation design and additionally, using highly conjugated and potentially electron-rich or electron-poor cations to push organic layer energies more into the same region as the VBM and CBM of the inorganic layers warrants further exploration by researchers.

4.3. X-Site Halide Ions
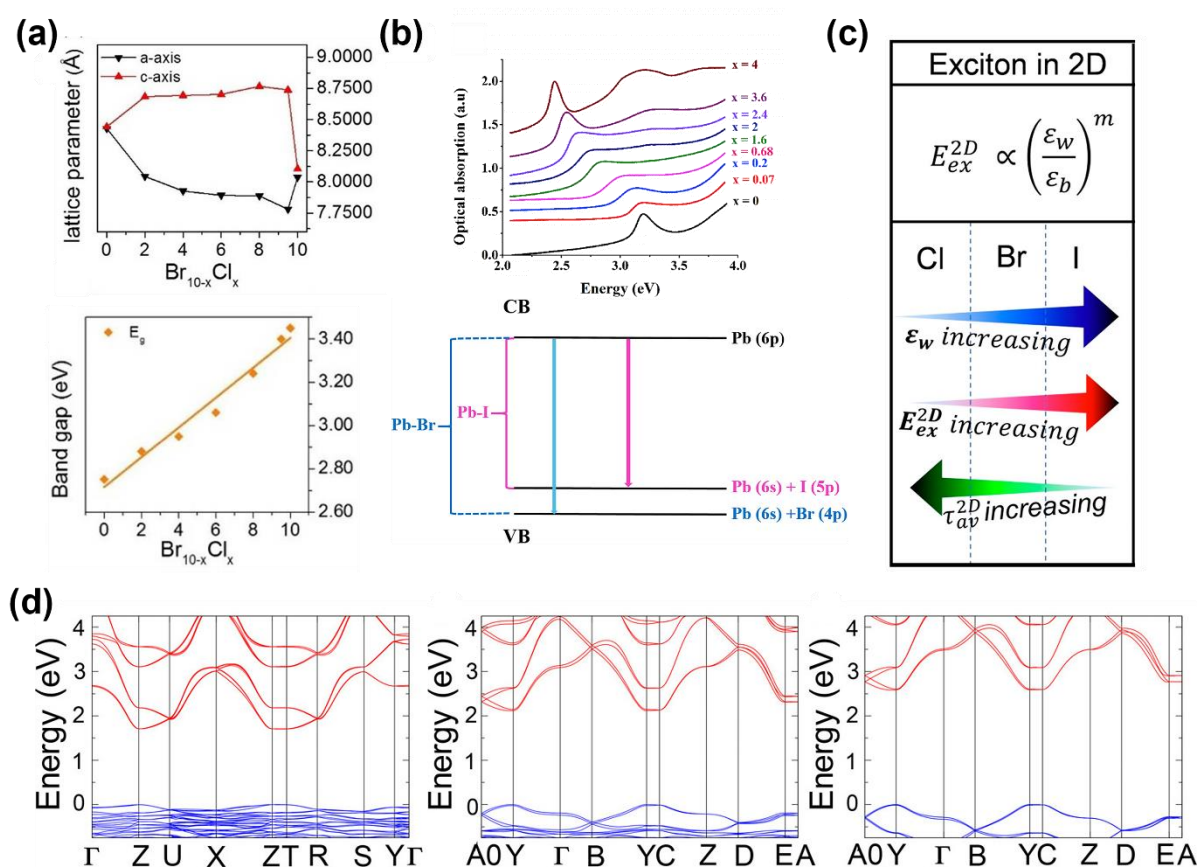
Figure 12. (a) Lattice changes and band gap trends of $EA_4Pb_3Br_{10-x}Cl_x$ (x = 0, 2, 4, 6, 8, 9.5, and 10). Reproduced with permission.[245] Copyright 2017, American Chemical Society. (b) Optical absorption spectra of $(C_6H_{11}NH_3)_2[PbBr_{4-x}I_x]$ films and schematic energy levels of orbitals in compounds. Reproduced with permission.[246] Copyright 2017, Elsevier. (c) Effect of halogens on the ε_r, E_b, and exciton lifetime of 2D perovskites. Reproduced with permission.[187b] Copyright 2020, American Chemical Society. (d) DFT calculations of band structures, from left to right: $(3APr)PbI_4$, $(3APr)PbBr_4$, and $(3APr)PbCl_4$. Reproduced with permission.[247] Copyright 2019, American Chemical Society.

Halogens play a crucial role in perovskite materials. Specifically, Br⁻ and I⁻ contribute to higher optical absorption coefficients and stability, although they have slower diffusion rates. On the other hand, Cl exhibits excellent charge transfer properties but lower light absorption capacity. Furthermore, the ionic radii differences across the halide series significantly impact perovskite materials through structural changes; altering their composition affects the tolerance factor, leading to tetrahedral distortions that further influence the electronic structure of 2D perovskites.

Single crystal x-ray diffraction studies have and continue to elucidate the complex relationship between halide ions, the crystal structure, and the properties of 2D perovskites, with continuous research focused on halide mixing. Mao *et al*. investigated the impact of halide

composition on 2D perovskites by synthesizing $EA_4Pb_3Br_{10-x}Cl_x$, where EA^+ served as both the spacer and A-site cation.[245] The difference in the lattice parameters, specifically the a- and c-axes, increased as the Cl^- content increased. More specifically, an increase in the Cl content led to greater lattice distortion and an increase in the bandgap of $EA_4Pb_3Br_{10-x}Cl_x$. The larger ionic radius of Br^- could explain this phenomenon compared to Cl^-, which enlarged the cavities in the inorganic layers. These larger cavities could better accommodate the bulky EA^+ cations, reducing octahedral distortions and ultimately affecting the bandgap size. Moreover, compared to the narrow blue light emission observed in $EA_4Pb_3Br_{10}$, the distortion of the inorganic framework also enabled $EA_4Pb_3Cl_{10}$ to exhibit broad white light emission. This could be understood through an amplified process of self-trapped excitons (STEs). The highly distorted Pb-X framework facilitated the generation of additional transient photoexcited STE states arising from solid electron-phonon coupling.

Boukheddaden *et al*. explored the impact of I^- and Br^- content on 2D perovskites.[246] The bandgap of different compositions of 2D perovskites decreased as the I^- content increased (**Figure 12b**). In typical 2D perovskite crystals, the valence band is composed of a hybridization of Pb 6s orbitals with Br 4p or I 5p orbitals. The extent of orbital hybridization between metals and halogens largely influenced the electronic band structure of 2D perovskites. The decrease in the bandgap could be explained by the higher energy level of the I 5p orbital compared to the Br 4p orbital. As the content of I increased, the perovskite's valence band structure changed, with the hybridization of Pb 6s orbitals with I 5p and Br 4p orbitals. Furthermore, variations in halogen content also altered the strength of hydrogen bonding interactions with the organic layers. Hydrogen bonds that formed between organic ammonium cations and Br^- were shorter, indicating stronger hydrogen bonding interactions. This difference led to greater octahedral distortion, resulting in STE that shifts the photoluminescence effect towards white light emission.

Chakraborty *et al*. investigated the influence of different halogen compositions on E_b. The high-frequency ε_r of the inorganic well layer (ε_w) and the organic barrier (ε_b) significantly affected the exciton binding energy (E_{ex}^{2D}) in 2D perovskites.[187b] Any changes in the halogen composition could alter ε_w, thus further impacting E_{ex}^{2D}. Li *et al*. studied the effect of three halogens on the electronic band structure of 2D perovskites.[247] The trend in bandgap followed $E_g(I) < E_g(Br) < E_g(Cl)$, indicating that the change from iodide to chloride reduces the VBM while the CBM remains nearly unchanged, resulting in an increased bandgap (**Figure 12d**). This was because halogen variation within the inorganic framework leads to different tolerances for the same spaced cations. The Pb-I bond length was the longest among Pb-X, creating the

most significant space to accommodate the cations. Additionally, iodide had the lowest electronegativity and highest polarizability among the halides, resulting in weaker hydrogen bonding with N-H and less electrostatic repulsions.

In summary, halide ionic radii, polarizability, electronegativity (and subsequent strength of H-bonding), and orbital mixing with the B-site metal all contribute to the design of 2D perovskites. I⁻ with a larger radius, higher polarizability, and lower electronegativity, has more significant advantages in adjusting the material's band structure and reducing the bandgap. Furthermore, regarding the X-site component, previous studies have mainly focused on controlling the influence of halides on excitons and band structures. There is an urgent need for a thorough discussion of the charge transfer mechanisms influenced by halides. Specifically, intentional comparisons are carried out for the same A-site and B-site compositions but with different X-site compositions, and carrier dynamics have been measured.

4.4. A-Site Cations

The previous section mentioned the influence of interlayer cations in quasi-2D perovskites. This section will illustrate the differences brought about by varying the thickness of inorganic layers (values of n) and A-site cations. The thickness of the potential barrier determines the carrier transport between inorganic layers in perovskite structures. However, insulating organic spacers leads to a higher energy barrier in 2D perovskites, resulting in poor carrier transport between the inorganic layers. By adjusting the content of A-site cations, it is possible to increase values of n, thereby minimizing the influence of interlayer barriers. Moreover, increasing the thickness of the inorganic layers effectively suppresses quantum confinement effects in 2D perovskites, reducing exciton binding energies and facilitating carrier generation and transport.[248]

4.4.1. Content of A-Site Cations (Inorganic Layer Thickness)
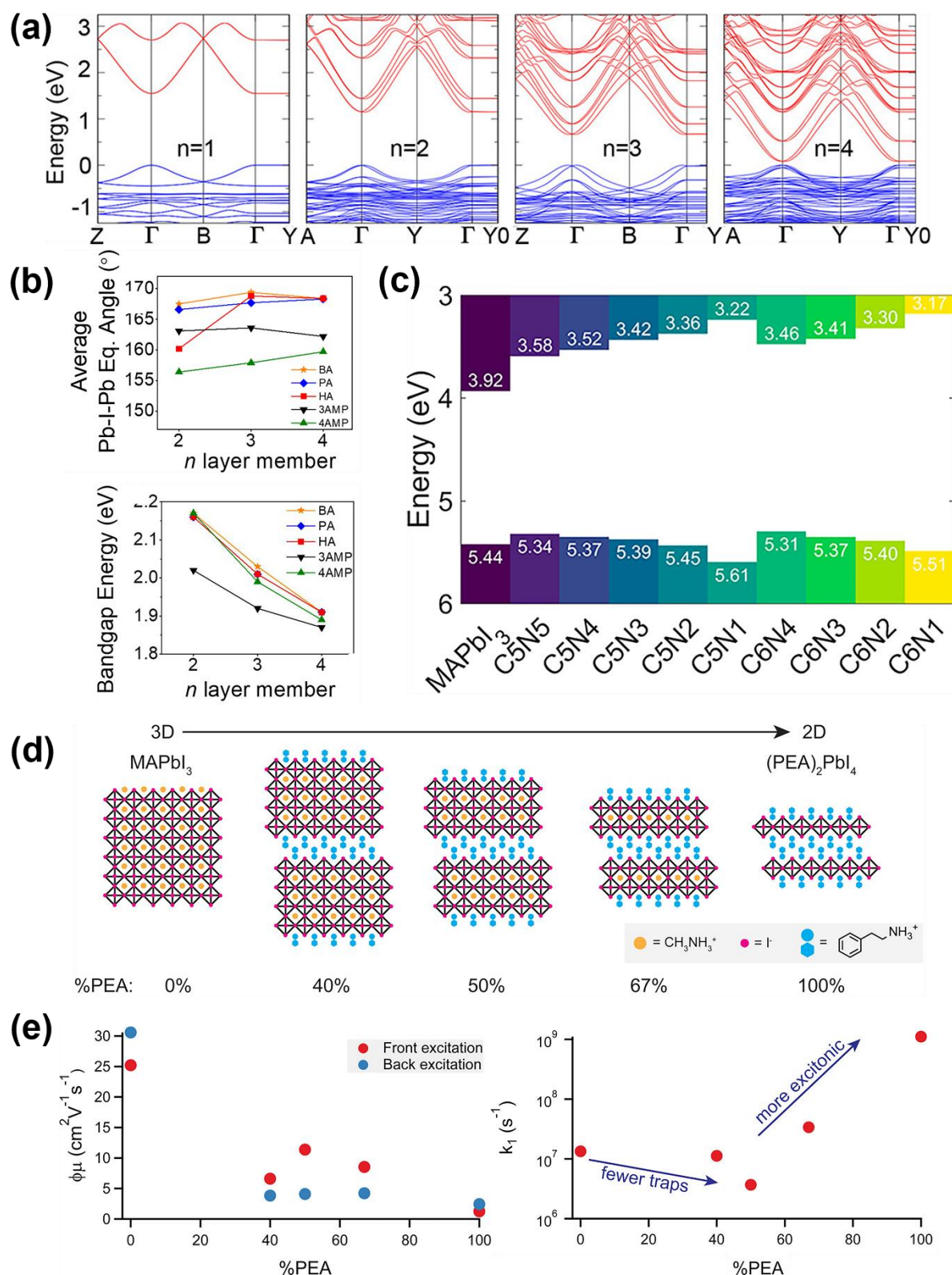
Figure 13. (a) Band structures of $(NH_3C_8H_{16}NH_3)(CH_3NH_3)_{n-1}Pb_nI_{3n+1}$ (m = 8, n = 1−4). Reproduced with permission.[115] Copyright 2018, American Chemical Society. (b) Average Pb-I-Pb angle as a function of perovskite layer thickness (n) for different spaced cationic 2D perovskite. Reproduced with permission.[249] Copyright 2021, American Chemical Society. (c) Comparative band energy diagram of perovskite. Reproduced with permission.[39c] Copyright 2019, American Chemical Society. (d) Schematic representation of the change in the crystal

structure of chalcocite with increasing PEA content. (e) The change of Effective charge-carrier mobility ($\varphi\mu$) and monomolecular recombination rate (k_1) with increasing PEA content. Reproduced under terms of the CC-BY license.[179] Copyright 2016, Rebecca L. Milot et al., published by American Chemical Society.

Li *et al.* investigated the impact of inorganic layer thickness on the band structure of 2D perovskites.[115] It was evident that the perovskite bandgap decreases significantly with increasing inorganic layer thickness. As the value of "n" increased, the sub-bands gradually expanded, widening the energy band range. This led to a reduction in quantum confinement and a decrease in the bandgap. (**Figure 13a**). Vasileiadou *et al.* compared the structures and properties of RP and DJ phase perovskites with different values of n and found that as n increases, the trend of the equatorial Pb-I-Pb bond angle, directly related to the electronic band structure, was towards an increase in both types of 2D perovskites.[249] Furthermore, they observed a decrease in the bandgap to a certain extent (**Figure 13b**). This indicates that increasing the value of n can weaken the influence of interlayer organic spacers on the structure of 2D perovskites. Similar findings were also reported by Spanopoulos *et al.*[39c] The bandgap gradually decreases with the increase in n (**Figure 13c**). Moreover, as n increases, the exciton peak gradually disappears. This phenomenon can be attributed to the diminishing quantum confinement effects and enhanced vertical diffusion of electrons and holes with increasing layers. As a result, the energy level structure of excitons becomes less defined. For ACI-phase perovskites, augmenting the value of n also contributes to diminishing their bandgap, enhancing charge collection efficiency, and ameliorating charge carrier transport properties.[250]

Does continuously increasing the number of inorganic layers improve the optoelectronic performance of 2D perovskites? Milot *et al.* investigated the influence of the value of n on the carrier mobility, charge dynamics, and diffusion length of thin films of 2D perovskites ($PEA_2MA_{n-1}Pb_nI_{3n+1}$), where the value of n was determined by the content of the organic cation PEA^+ (**Figure 13e**).[179] It could be observed that the overall trend of carrier mobility was to decrease with increasing PEA^+ content. However, the variation in charge carrier mobility was not linear, and films containing 40% PEA^+ exhibited the lowest mobility. This phenomenon is closely related to the process of single-molecule recombination (**Figure 13f**). The single-molecule recombination rate is related to the presence of defects in the material, and a small amount of PEA^+ can effectively passivate the defects in the perovskite, improving the film quality and reducing the single-molecule recombination rate. However, as the PEA^+ content increases, the quantum confinement effect increases due to dimensional reduction, increasing E_b and the probability of exciton formation. This provides an additional pathway for single-

molecule recombination. The change in film orientation during the rise in PEA^+ content also affects carrier mobility. As the value of n decreases, the perovskite film transitions from a random to a parallel orientation, significantly limiting carrier transport.

In summary, while increasing the content of A-site cations to enhance the benefits of increased layer thickness is significant, it is also essential to consider the trade-offs between perovskite orientation, defects, quantum confinement, and stability issues. The issue of uneven phase distribution should also be considered, as discussed in the interlayer (A'-site) cations section.

4.4.2. Types of A-Site Cations
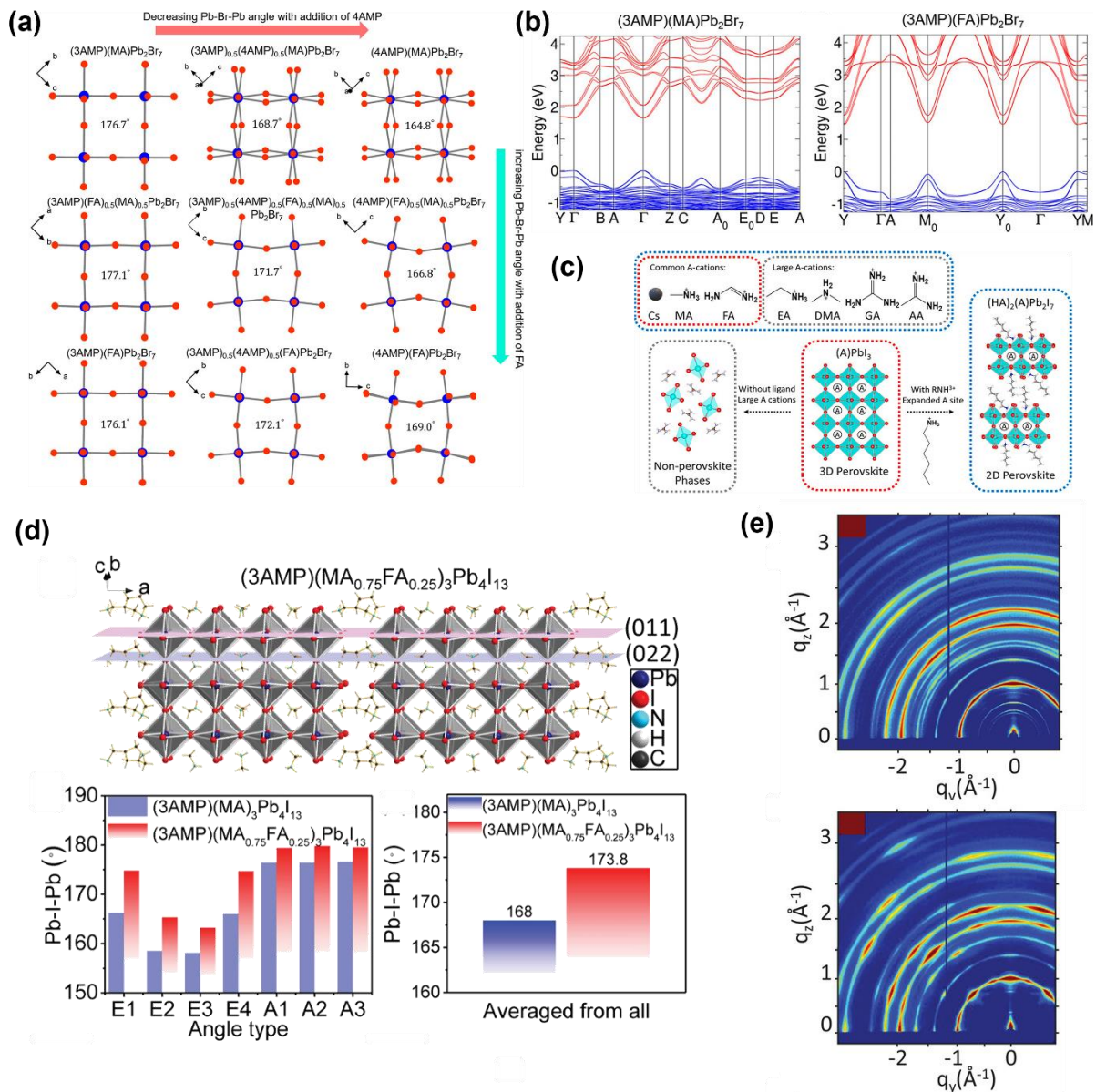
Figure 14. (a) Top view of 2D perovskite crystal structure with different compositions. (b) band structure of $(3AMP)(MA)Pb_2Br_7$ and $(3AMP)(FA)Pb_2Br_7$. Reproduced with permission.[124a]

As a reminder, A-site cations are differentiated from A'-site cations as cations that fulfill the tolerance factor $0.8 < t < 1.0$, such that A cations produce 3D structures and A' cations produce lower dimensional structures. Guo *et al*. compared the structural and performance differences in DJ phase 2D perovskites resulting from different A-site cations.[124a] Within the same series of 2D perovskites, the average Pb-Br-Pb angle gradually increased with increasing content of FA cations (**Figure 14a**). This phenomenon could be attributed to the larger volume of FA cations in the octahedral cavities, inhibiting octahedral distortion. It was evident that FA-based perovskites exhibited a more dispersed valence band than MA-based perovskites (**Figure 14b**). This was a result of the enlarged Pb-Br-Pb bond angles, which led to increased overlap between the Pb s- and Br p-orbitals, thereby enhancing the interaction between bonding and anti-bonding orbitals, broadening the valence band and elevating the energy level of the VBM. The regulation of A-site cations has also been studied in ACI-phase perovskites. Compared to MA-based and Cs-based ACI-phase perovskites, the introduction of FA^+ results in a different crystal structure.[253] As discussed earlier, perovskites' electronic band structure and charge transport are closely related to their structure. Therefore, the performance modulation of ACI-phase perovskites can also be achieved through the compositional design of A-site cations.

In contrast to the limited choice of A-site cations in 3D perovskites, 2D perovskites exhibit higher tolerance towards A-site cations. Hautzinger *et al*. investigated the role of A-site cations by selecting seven different A-site cations to synthesize 2D perovskites (**Figure 14c**).[251] Compared to FA^+ and MA^+, larger cations such as EA^+ and DMA^+ and the smallest cation, Cs+, exhibited a significant increase in bandgap. This could be attributed to the larger A-site cations compressing the inorganic layer, leading to distortion. In contrast, the smaller Cs^+ could not fully support the octahedral cavities in the inorganic layer, causing the octahedra to tilt. Comprehensive analysis suggested that appropriately sized FA^+ and MA^+ seemed to be the "ideal" A-site cations within the lead iodide perovskite cage. Perovskites with appropriately sized MA^+ and FA^+ had longer carrier lifetimes, lower defect densities, and fewer non-radiative recombination than other A-site cations. This was due to the stretching of the Pb-I bonds and distortion of the Pb-I network when the larger cations were introduced into the octahedral

cavities, which enhanced electron-phonon coupling and made the perovskite more prone to non-radiative recombination.

A-site cations impact the skeleton structure of perovskite and influence the crystallinity of thin films. Zhou *et al*. investigated the effect of incorporating FA^+ on the crystallization kinetics.[254] The results demonstrated that incorporating FA^+ helped reduce the non-radiative recombination centers in the thin films, forming highly oriented and high-quality films. Furthermore, Gao *et al*. first explored the advantages of 2D perovskites mixed with three A-site cations (MA^+, FA^+, Cs^+).[1g] Compared to traditional materials based solely on MA^+, the 2D perovskite films with the mixture of these three cations exhibited smoother and denser surface morphology, larger grain size, and fewer grain boundaries. These characteristics favored reducing defect sites, suppressing non-radiative recombination, and extending carrier lifetime. To investigate the influence of FA^+ content on 2D perovskites more comprehensively, Ke *et al*. introduced five different levels of FA^+ content (ranging from 0% to 30%).[252] At FA^+ content of 25%, the corresponding 2D perovskite exhibited the narrowest bandgap and the largest Pb-I-Pb bond angle. Additionally, the 2D perovskite film with a 25% FA^+ content demonstrates excellent <011> orientation and vertical growth on the substrate (**Figure 14e**), significantly enhancing carrier transport properties.

In summary, although 2D perovskites offer a more comprehensive range of choices for A-site cations, moderately sized MA^+ and FA^+ remain the preferred options. Specifically, the FA cation contributes to film crystallization and reduces non-radiative recombination, among other advantages. However, in mixed A-site cation 2D perovskites, the improvement in transport performance is not directly proportional to the FA^+ content. Determining the optimal FA^+ content remains a crucial step in optimizing charge transport.

5. Charge Transport in Halide Perovskites

The insufficient transport properties of 2D perovskite in the direction perpendicular to the inorganic layers pose a significant challenge in this field. To address this issue, a solid theoretical foundation is essential. This article systematically summarizes the influencing factors and standard test methods of charge transport in 2D perovskites, demonstrating the role of compositional tuning in enhancing the transport properties of 2D perovskites. Therefore, this article also serves as a reference for establishing the fundamental theory of factors affecting the transport properties of 2D perovskite for future researchers. Despite these merits, efforts toward some intractable challenges remain to be emphasized as follows:

Thin films' Phase purity. In practice, for 2D perovskites with n > 3, the films often consist

of MQWs with varying n values. The 2D films with mixed n values may limit their efficiency for different optoelectronic uses and also cloud the ability to fundamentally understand the origins of observed carrier transport properties in thin films, especially in light of the diversity of physical and chemical characteristics that can be accessed in 2D perovskite structures. This will lead to another issue of customizing materials and structure design. Creating synthetic tools and strategies to isolate pure-phase 2D perovskite structures and analyze the distribution of various n values will advance the progress of 3D/2D perovskites and enhance the comprehension of their optoelectronic characteristics for potential applications in other optoelectronic domains. Until precise control over mixed n numbers can be proven in perovskite single crystals or thin film samples, more mechanistic studies should be carried out with simplified n = 1 compositions.

Charge transport in 2D perovskites. The crystalline growth mode has been demonstrated to have a particular influence on the transport of 2D perovskites. Hence, it is imperative to develop a unified crystal growth method and devise an in-situ detection technique for single-crystal growth while simultaneously measuring charge carrier transport. These direct measurements and their correlations should be combined with existing single-crystal databases to gather single-crystal data and identify robust "rules" that describe structure-property relationships with charge transport. Similarly, challenges exist in the characterization of transport properties of polycrystalline thin films; different testing methods significantly impact the transport characterization of thin films. Even for the same thin films, obtaining consistent experimental results is challenging due to experimental conditions and device structure variations.[255] This uncertainty in summarizing the factors influencing the transport properties of perovskite materials makes it challenging to derive general trends from different transport testing methods, so broader surveys of sole source samples with sole source measurements would benefit the field. Establishing a standardized testing method and unified criteria to address this issue is crucial to facilitate comparisons between different studies. With access to more extensive and higher quality structural datasets as well as standardized collections of high-quality transport characterization techniques in databases, artificial intelligence and machine learning approaches should expedite the complex parameter and variable space involved with understanding the design principles that will unlock exceptional performance and material stability in 2D and 2D/3D perovskites.

Only after addressing the shortcomings above in the field of 2D perovskites and obtaining guiding synthetic principles can we further consolidate and expand their application value.

In photovoltaic applications, 2D perovskites can serve not only as absorbing layers themselves but also as capping layers on top of 3D perovskite absorbing layers or mixing directly with 3D perovskites to form a composite absorbing layer (forming 2D/3D heterojunctions).[256] The latter serves as a strategy to mitigate the insufficient charge transport in 2D perovskites (distinct from the regulation of 2D perovskite itself discussed in this review), aiming to combine the excellent stability of 2D perovskites with the outstanding optoelectronic properties of 3D perovskites.[257] Furthermore, combining the charge transport optimization of 2D perovskites discussed in this review with the 2D/3D heterojunction strategy would enhance its effectiveness (prolonging carrier lifetimes, minimizing charge recombination, and optimizing charge extraction).[258]

Apart from their use in the photovoltaic field, the inherent multiple QW structure of 2D perovskites promotes the formation of excitons and reduces the likelihood of exciton dissociation, making them effective luminescent materials.[259] Additionally, the 2D/3D heterojunction can also be applied to LEDs. The formation of heterojunctions enhances energy cascading, induces energy transfer from the wide-bandgap region to the narrow-bandgap region, suppresses free charge diffusion, enhances radiative recombination, and ultimately improves the external quantum efficiency.[260] The tunable optical bandgap and self-trapping states in photodetectors make 2D perovskites highly promising for narrow-band light detection.[261] Moreover, the presence of interlayer cations gives 2D perovskites anisotropic in-plane/out-of-plane conductivity. The minimal conductivity along the out-of-plane direction effectively suppresses dark currents and improves the on-off ratio, enhancing device performance.[262]

In conclusion, the numerous excellent properties of 2D perovskites provide them with enormous potential in various application fields. Their inherent stability advantages open up possibilities for practical device applications. Subsequent research should focus on optimizing 2D perovskites to fully exploit their advantages in multiple fields.

Received: ((will be filled in by the editorial staff))
Revised: ((will be filled in by the editorial staff))
Published online: ((will be filled in by the editorial staff))

References

[1]   a) G. Xing, N. Mathews, S. Sun, S. S. Lim, Y. M. Lam, M. Grätzel, S. Mhaisalkar, T. C. Sum, Science 2013, 342, 344; b) D. W. de Quilettes, S. M. Vorpahl, S. D. Stranks, H. Nagaoka, G. E. Eperon, M. E. Ziffer, H. J. Snaith, D. S. Ginger, Science 2015, 348, 683; c) B. A. Connor, L. Leppert, M. D. Smith, J. B. Neaton, H. I. Karunadasa, J. Am. Chem. Soc. 2018, 140, 5235; d) J. Pan, Z. Chen, T. Zhang, B. Hu, H. Ning, Z. Meng, Z. Su, D. Nodari, W. Xu, G. Min, M. Chen, X. Liu, N. Gasparini, S. A. Haque, P. R. F. Barnes, F. Gao, A. A. Bakulin, Nat. Commun. 2023, 14, 8000; e) X. Y. Chin, D. Turkay, J. A. Steele, S. Tabean, S. Eswara, M. Mensi, P. Fiala, C. M. Wolff, A. Paracchino, K. Artuk, D. Jacobs, Q. Guesnay, F. Sahli, G. Andreatta, M. Boccard, Q. Jeangros, C. Ballif, Science 2023, 381, 59; f) S. D. Stranks, G. E. Eperon, G. Grancini, C. Menelaou, M. J. P. Alcocer, T. Leijtens, L. M. Herz, A. Petrozza, H. J. Snaith, Science 2013, 342, 341; g) L. Gao, F. Zhang, X. Chen, C. Xiao, B. W. Larson, S. P. Dunfield, J. J. Berry, K. Zhu, Angew Chem Int Ed Engl 2019, 58, 11737.

[2]   a) R. Lin, J. Xu, M. Wei, Y. Wang, Z. Qin, Z. Liu, J. Wu, K. Xiao, B. Chen, S. M. Park, G. Chen, H. R. Atapattu, K. R. Graham, J. Xu, J. Zhu, L. Li, C. Zhang, E. H. Sargent, H. Tan, Nature 2022, 603, 73; b) Y. Rong, Y. Hu, A. Mei, H. Tan, M. I. Saidaminov, S. I. Seok, M. D. McGehee, E. H. Sargent, H. Han, Science 2018, 361.

[3]   a) Y.-K. Wang, F. Jia, X. Li, S. Teale, P. Xia, Y. Liu, P. T.-s. Chan, H. Wan, Y. Hassan, M. Imran, H. Chen, L. Grater, L.-D. Sun, G. C. Walker, S. Hoogland, Z.-H. Lu, C.-H. Yan, L.-S. Liao, E. H. Sargent, Sci. Adv. 2023, 9, eadh2140; b) J. S. Kim, J.-M. Heo, G.-S. Park, S.-J. Woo, C. Cho, H. J. Yun, D.-H. Kim, J. Park, S.-C. Lee, S.-H. Park, E. Yoon, N. C. Greenham, T.-W. Lee, Nature 2022, 611, 688.

[4]   a) Y. Hou, J. Li, J. Yoon, A. M. Knoepfel, D. Yang, L. Zheng, T. Ye, S. Ghosh, S. Priya, K. Wang, Sci. Adv. 2023, 9, eade2338; b) Y. Zhou, C. Fei, M. A. Uddin, L. Zhao, Z. Ni, J. Huang, Nature 2023, 616, 712.

[5]   a) S. P. Senanayak, M. Abdi-Jalebi, V. S. Kamboj, R. Carey, R. Shivanna, T. Tian, G. Schweicher, J. Wang, N. Giesbrecht, D. Di Nuzzo, H. E. Beere, P. Docampo, D. A. Ritchie, D. Fairen-Jimenez, R. H. Friend, H. Sirringhaus, Sci. Adv. 2020, 6, eaaz4948; b) S. P. Senanayak, K. Dey, R. Shivanna, W. Li, D. Ghosh, Y. Zhang, B. Roose, S. J. Zelewski, Z. Andaji-Garmaroudi, W. Wood, N. Tiwale, J. L. MacManus-Driscoll, R. H. Friend, S. D. Stranks, H. Sirringhaus, Nat. Mater. 2023, 22, 216.

[6]   a) X. Wang, L. Jin, A. Sergeev, W. Liu, S. Gu, N. Li, K. Fan, S.-c. Chen, K. S. Wong, X. Sun, N. Zhao, Sci. Adv. 2023, 9, eadj3476; b) C. Qin, A. S. D. Sandanayaka, C. Zhao, T. Matsushima, D. Zhang, T. Fujihara, C. Adachi, Nature 2020, 585, 53.

[7]   https://wwwnrelgov/pv/cell-efficiencyhtml.

[8]   a) F. Zhang, W. Shi, J. Luo, N. Pellet, C. Yi, X. Li, X. Zhao, T. J. S. Dennis, X. Li, S. Wang, Y. Xiao, S. M. Zakeeruddin, D. Bi, M. Gratzel, Adv Mater 2017, 29, 1606806; b) J.-P. Correa-Baena, M. Saliba, T. Buonassisi, M. Grätzel, A. Abate, W. Tress, A. Hagfeldt, Science 2017, 358, 739; c) F. Zhang, S. Y. Park, C. Yao, H. Lu, S. P. Dunfield, C. Xiao, S. Uličná, X. Zhao, L. Du Hill, X. Chen, X. Wang, L. E. Mundt, K. H. Stone, L. T. Schelhas, G. Teeter, S. Parkin, E. L. Ratcliff, Y.-L. Loo, J. J. Berry, M. C. Beard, Y. Yan, B. W. Larson, K. Zhu, Science 2022, 375, 71; d) Y. Chen, J. Hu, Z. Xu, Z. Jiang, S. Chen, B. Xu, X. Xiao, X. Liu, K. Forberich, C. J. Brabec, Y. Mai, F. Guo, Adv. Funct. Mater. 2022, 32; e) N. Ahn, M. Choi, Adv. Sci., n/a, 2306110.

[9]   a) W. Chen, Y. Shi, J. Chen, P. Ma, Z. Fang, D. Ye, Y. Lu, Y. Yuan, J. Zhao, Z. Xiao, Adv Mater 2021, 33, e2104842; b) Y. Wang, T. Wu, J. Barbaud, W. Kong, D. Cui, H. Chen, X. Yang, L. Han, Science 2019, 365, 687; c) H. Kim, M. Pei, Y. Lee, A. A. Sutanto, S. Paek, V. I. E. Queloz, A. J. Huckaba, K. T. Cho, H. J. Yun, H. Yang, M. K. Nazeeruddin, Adv. Funct. Mater. 2020, 30, 1910620; d) Y. Zheng, T. Niu, X. Ran, J. Qiu, B. Li, Y. Xia, Y. Chen, W. Huang, J. Mater. Chem. A 2019, 7, 13860.

[10]   J. M. Frost, K. T. Butler, F. Brivio, C. H. Hendon, M. van Schilfgaarde, A. Walsh, Nano Lett. 2014, 14, 2584.

[11]   a) T. Yang, C. Ma, W. Cai, S. Wang, Y. Wu, J. Feng, N. Wu, H. Li, W. Huang, Z. Ding, L. Gao, S. Liu, K. Zhao, Joule 2023, 7, 574; b) Y. Zhang, M. Chen, T. He, H. Chen, Z. Zhang, H. Wang, H. Lu, Q. Ling, Z. Hu, Y. Liu, Y. Chen, G. Long, Adv Mater 2023, 35, e2210836.

[12]   N. J. Jeon, J. H. Noh, W. S. Yang, Y. C. Kim, S. Ryu, J. Seo, S. I. Seok, Nature 2015, 517, 476.

[13]   C. Liu, Y. Yang, H. Chen, J. Xu, A. Liu, A. S. R. Bati, H. Zhu, L. Grater, S. S. Hadke, C. Huang, V. K. Sangwan, T. Cai, D. Shin, L. X. Chen, M. C. Hersam, C. A. Mirkin, B. Chen, M. G. Kanatzidis, E. H. Sargent, Science 2023, 382, 810.

[14]   a) D. P. McMeekin, P. Holzhey, S. O. Fürer, S. P. Harvey, L. T. Schelhas, J. M. Ball, S. Mahesh, S. Seo, N. Hawkins, J. Lu, M. B. Johnston, J. J. Berry, U. Bach, H. J. Snaith, Nat. Mater. 2023, 22, 73; b) F. Zhang, K. Zhu, Adv. Energy Mater. 2020, 10, 1902579; c) H. Zhong, X. Liu, M. Liu, S. Yin, Z. Jia, G. Fu, S. Yang, W. Kong, Nano Energy 2023, 105, 108014.

[15]   Y. Shi, F. Zhang, Sol. RRL 2023, 7, 2201123.

[16]   K. Li, S. Yue, X. Li, N. Ahmad, Q. Cheng, B. Wang, X. Zhang, S. Li, Y. Li, G. Huang, H. Kang, T. Yue, S. U. Zafar, H. Zhou, L. Zhu, Y. Zhang, Adv. Funct. Mater. 2022, 32.

[17]   a) M. Shao, T. Bie, L. Yang, Y. Gao, X. Jin, F. He, N. Zheng, Y. Yu, X. Zhang, Adv Mater 2022, 34, 2107211; b) Y. C. Liu, J. T. Lin, Y. L. Lee, C. M. Hung, T. C. Chou, W. C. Chao, Z. X. Huang, T. H. Chiang, C. W. Chiu, W. T. Chuang, P. T. Chou, J Am Chem Soc 2022, 144, 14897.

[18]   M. Saliba, T. Matsui, K. Domanski, J.-Y. Seo, A. Ummadisingu, S. M. Zakeeruddin, J.-P. Correa-Baena, W. R. Tress, A. Abate, A. Hagfeldt, M. Grätzel, Science 2016, 354, 206.

[19]   J. Li, H. Liang, C. Xiao, X. Jia, R. Guo, J. Chen, X. Guo, R. Luo, X. Wang, M. Li, M. Rossier, A. Hauser, F. Linardi, E. Alvianto, S. Liu, J. Feng, Y. Hou, Nat. Energy 2024.

[20]   a) J. Gong, M. Hao, Y. Zhang, M. Liu, Y. Zhou, Angew Chem Int Ed Engl 2022, 61, e202112022; b) J. Sun, K. Wang, K. Ma, J. Y. Park, Z. Y. Lin, B. M. Savoie, L. Dou, J Am Chem Soc 2023, 145, 20694; c) X. Li, J. M. Hoffman, M. G. Kanatzidis, Chem Rev 2021, 121, 2230; d) F. Zhang, H. Lu, J. Tong, J. J. Berry, M. C. Beard, K. Zhu, Energy Environ. Sci. 2020, 13, 1154.

[21]   H. L. Wells, Z. Anorg. Chem. 1893, 3, 195.

[22]   B. E. Cohen, Y. Li, Q. Meng, L. Etgar, Nano Lett 2019, 19, 2588.

[23]   V. M. Goldschmidt, Naturwissenschaften 1926, 14, 477.

[24]   C. Ge, Y. Li, H. Song, Q. Xie, L. Zhang, X. Ma, J. Liu, X. Guo, Y. Yan, D. Liu, W. Zhang, S. Liu, Y. Liu, Nat. Commun. 2024, 15, 914.

[25]   H. Lai, B. Kan, T. Liu, N. Zheng, Z. Xie, T. Zhou, X. Wan, X. Zhang, Y. Liu, Y. Chen, J Am Chem Soc 2018, 140, 11639.

[26]   Y. Dolzhenko, T. Inabe, Y. Maruyama, Bull. Chem. Soc. Jpn. 1986, 59, 563.

[27]   C. C. Stoumpos, D. H. Cao, D. J. Clark, J. Young, J. M. Rondinelli, J. I. Jang, J. T. Hupp, M. G. Kanatzidis, Chem. Mater. 2016, 28, 2852.

[28]   a) D. Lu, G. Lv, Z. Xu, Y. Dong, X. Ji, Y. Liu, J Am Chem Soc 2020, 142, 11114; b) L. Mao, W. Ke, L. Pedesseau, Y. Wu, C. Katan, J. Even, M. R. Wasielewski, C. C. Stoumpos, M. G. Kanatzidis, J Am Chem Soc 2018, 140, 3775.

[29]   K. Zheng, T. Pullerits, J Phys Chem Lett 2019, 10, 5881.

[30]   F. Zhang, K. Zhu, Joule 2021, 5, 14.

[31]   a) L. Yan, J. Ma, P. Li, S. Zang, L. Han, Y. Zhang, Y. Song, Adv Mater 2022, 34, 2106822; b) X. Zhang, T. Yang, X. Ren, L. Zhang, K. Zhao, S. Liu, Adv. Energy Mater. 2021, 11.

[32]   a) P. Yan, S. Hu, Y. Zhang, C. Wang, Y. Wang, H. Li, C. Sheng, Org. Electron. 2022, 105, 106486; b) Y. Huang, Y. Li, E. L. Lim, T. Kong, Y. Zhang, J. Song, A. Hagfeldt, D. Bi, J. Am. Chem. Soc. 2021, 143, 3911; c) Y. Ding, Y. Wu, Y. Tian, Y. Xu, M. Hou, B. Zhou, J. Luo, G. Hou, Y. Zhao, X. Zhang, J. Energy Chem. 2021, 58, 48.

[33]   M.-J. Yang, S.-Y. Tang, Y.-R. Weng, F. Zhou, Y. Shi, Y.-J. Bai, Y. Ai, Inorg. Chem. 2022, 61, 5836.

[34]   D. Pariari, S. Mehta, S. Mandal, A. Mahata, T. Pramanik, S. Kamilya, A. Vidhan, T. N. Guru Row, P. K. Santra, S. K. Sarkar, F. De Angelis, A. Mondal, D. D. Sarma, J. Am. Chem. Soc. 2023, 145, 15896.

[35]   a) S. N. Ruddlesden, P. Popper, Acta Crystallographica 1958, 11, 54; b) S. N. Ruddlesden, P. Popper, Acta Crystallographica 1957, 10, 538; c) M. Dion, M. Ganne, M. Tournoux, Mater. Res. Bull. 1981, 16, 1429; d) A. J. Jacobson, J. W. Johnson, J. T. Lewandowski, Inorg. Chem. 1985, 24, 3727.

[36]   M.-H. Tremblay, J. Bacsa, B. Zhao, F. Pulvirenti, S. Barlow, S. R. Marder, Chem. Mater. 2019, 31, 6145.

[37]   G. Wu, T. Yang, X. Li, N. Ahmad, X. Zhang, S. Yue, J. Zhou, Y. Li, H. Wang, X. Shi, S. Liu, K. Zhao, H. Zhou, Y. Zhang, Matter 2021, 4, 582.

[38]   a) P. Cheng, Z. Xu, J. Li, Y. Liu, Y. Fan, L. Yu, D.-M. Smilgies, C. Müller, K. Zhao, S. F. Liu, ACS Energy Lett. 2018, 3, 1975; b) S. Ahmad, P. Fu, S. Yu, Q. Yang, X. Liu, X. Wang, X. Wang, X. Guo, C. Li, Joule 2019, 3, 794.

[39]   a) Y. Chen, Y. Sun, J. Peng, W. Zhang, X. Su, K. Zheng, T. Pullerits, Z. Liang, Adv. Energy Mater. 2017, 7; b) X. Zhao, M. L. Ball, A. Kakekhani, T. Liu, A. M. Rappe, Y. L. Loo, Nat Commun 2022, 13, 3970; c) I. Spanopoulos, I. Hadar, W. Ke, Q. Tu, M. Chen, H. Tsai, Y. He, G. Shekhawat, V. P. Dravid, M. R. Wasielewski, A. D. Mohite, C. C. Stoumpos, M. G.

Kanatzidis, J Am Chem Soc 2019, 141, 5518; d) C. Ni, Y. Huang, T. Zeng, D. Chen, H. Chen, M. Wei, A. Johnston, A. H. Proppe, Z. Ning, E. H. Sargent, P. Hu, Z. Yang, Angew Chem Int Ed Engl 2020, 59, 13977.

[40]   R. L. Kingsford, S. R. Jackson, L. C. Bloxham, C. G. Bischak, J Am Chem Soc 2023, 145, 11773.

[41]   R. Hamaguchi, M. Yoshizawa-Fujita, T. Miyasaka, H. Kunugita, K. Ema, Y. Takeoka, M. Rikukawa, Chem Commun (Camb) 2017, 53, 4366.

[42]   A. Lemmerer, D. G. Billing, Dalton Trans 2012, 41, 1146.

[43]   a) M. C. Weidman, M. Seitz, S. D. Stranks, W. A. Tisdale, ACS Nano 2016, 10, 7830; b) Z. Yin, J. Leng, S. Wang, G. Liang, W. Tian, K. Wu, S. Jin, J Am Chem Soc 2021, 143, 4725.

[44]   D. G. Billing, A. Lemmerer, New J. Chem. 2008, 32.

[45]   D. Yu, F. Cao, Y. Shen, X. Liu, Y. Zhu, H. Zeng, J Phys Chem Lett 2017, 8, 2565.

[46]   a) C. Lermer, S. T. Birkhold, I. L. Moudrakovski, P. Mayer, L. M. Schoop, L. Schmidt-Mende, B. V. Lotsch, Chem. Mater. 2016, 28, 6560; b) P. X. Wang, A. M. Najarian, Z. Hao, A. Johnston, O. Voznyy, S. Hoogland, E. H. Sargent, J Phys Chem Lett 2020, 11, 10144.

[47]   T. Zhang, L. Xie, L. Chen, N. Guo, G. Li, Z. Tian, B. Mao, Y. Zhao, Adv. Funct. Mater. 2017, 27.

[48]   G. Xie, L. Wang, P. Li, S. Song, C. Yao, S. Wang, Y. Liu, Z. Wang, X. Wang, X. Tao, ACS Appl Mater Interfaces 2021, 13, 3325.

[49]   A. Lemmerer, D. G. Billing, CrystEngComm 2010, 12, 1290.

[50]   B. Luo, Y. Guo, Y. Xiao, X. Lian, T. Tan, D. Liang, X. Li, X. Huang, J Phys Chem Lett 2019, 10, 5271.

[51]   S. Tan, N. Zhou, Y. Chen, L. Li, G. Liu, P. Liu, C. Zhu, J. Lu, W. Sun, Q. Chen, H. Zhou, Adv. Energy Mater. 2018.

[52]   H. Ren, S. Yu, L. Chao, Y. Xia, Y. Sun, S. Zuo, F. Li, T. Niu, Y. Yang, H. Ju, B. Li, H. Du, X. Gao, J. Zhang, J. Wang, L. Zhang, Y. Chen, W. Huang, Nat. Photonics 2020, 14, 154.

[53]   X. Li, H. Dong, G. Volonakis, C. C. Stoumpos, J. Even, C. Katan, P. Guo, M. G. Kanatzidis, Chem. Mater. 2022, 34, 6541.

[54]   J. M. Hoffman, C. D. Malliakas, S. Sidhik, I. Hadar, R. McClain, A. D. Mohite, M. G. Kanatzidis, Chem Sci 2020, 11, 12139.

[55]   a) E. S. Vasileiadou, X. Jiang, M. Kepenekian, J. Even, M. C. De Siena, V. V. Klepov, D. Friedrich, I. Spanopoulos, Q. Tu, I. S. Tajuddin, E. A. Weiss, M. G. Kanatzidis, J Am Chem

Soc 2022, 144, 6390; b) A. H. Proppe, R. Quintero-Bermudez, H. Tan, O. Voznyy, S. O. Kelley, E. H. Sargent, J Am Chem Soc 2018, 140, 2890.

[56]   L. Chao, T. Niu, Y. Xia, X. Ran, Y. Chen, W. Huang, J Phys Chem Lett 2019, 10, 1173.

[57]   T. Zhu, Y. Yang, K. Gu, C. Liu, J. Zheng, X. Gong, ACS Appl Mater Interfaces 2020, 12, 51744.

[58]   M. Mączka, M. Ptak, A. Gągor, D. Stefańska, A. Sieradzki, Chem. Mater. 2019, 31, 8563.

[59]   T. Li, W. A. Dunlap-Shohl, E. W. Reinheimer, P. Le Magueres, D. B. Mitzi, Chem Sci 2019, 10, 1168.

[60]   K. T. Cho, Y. Zhang, S. Orlandi, M. Cavazzini, I. Zimmermann, A. Lesch, N. Tabet, G. Pozzi, G. Grancini, M. K. Nazeeruddin, Nano Lett 2018, 18, 5467.

[61]   D. G. Billing, A. Lemmerer, CrystEngComm 2009, 11.

[62]   S. A. Cuthriell, C. D. Malliakas, M. G. Kanatzidis, R. D. Schaller, J Am Chem Soc 2023, 145, 11710.

[63]   T. T. Sha, Y. A. Xiong, Q. Pan, X. G. Chen, X. J. Song, J. Yao, S. R. Miao, Z. Y. Jing, Z. J. Feng, Y. M. You, R. G. Xiong, Adv Mater 2019, 31, e1901843.

[64]   X. N. Li, P. F. Li, W. Q. Liao, J. Z. Ge, D. H. Wu, H. Y. Ye, Eur. J. Inorg. Chem. 2017, 2017, 938.

[65]   D. G. Billing, A. Lemmerer, Acta Crystallogr C 2006, 62, 269.

[66]   Y. Takahashi, R. Obara, K. Nakagawa, M. Nakano, J.-y. Tokita, T. Inabe, Chem. Mater. 2007, 19, 6312.

[67]   G. S. Lorena, H. Hasegawa, Y. Takahashi, J. Harada, T. Inabe, Chem. Lett. 2014, 43, 1535.

[68]   a) Z. Li, N. Liu, K. Meng, Z. Liu, Y. Hu, Q. Xu, X. Wang, S. Li, L. Cheng, G. Chen, Nano Lett 2019, 19, 5237; b) J. Rodríguez-Romero, B. C. Hames, I. Mora-Seró, E. M. Barea, ACS Energy Lett. 2017, 2, 1969.

[69]   Y. Q. Zhao, Q. R. Ma, B. Liu, Z. L. Yu, J. Yang, M. Q. Cai, Nanoscale 2018, 10, 8677.

[70]   C. K. Yang, W. N. Chen, Y. T. Ding, J. Wang, Y. Rao, W. Q. Liao, Y. Y. Tang, P. F. Li, Z. X. Wang, R. G. Xiong, Adv Mater 2019, 31, e1808088.

[71]   M.-H. Tremblay, J. Bacsa, S. Barlow, S. R. Marder, Mater. Chem. Front. 2020, 4, 2023.

[72]   a) Z. Wang, X. Liu, H. Ren, L. Liu, X. Tang, X. Yao, Z. Su, X. Gao, Q. Wei, H. Xie, Y. Zheng, M. Li, ACS Appl Mater Interfaces 2022, 14, 7917; b) S. Yu, Y. Yan, M. Abdellah, T. Pullerits, K. Zheng, Z. Liang, Small 2019, 15, e1905081.

[73]   a) Z. Wang, Q. Wei, X. Liu, L. Liu, X. Tang, J. Guo, S. Ren, G. Xing, D. Zhao, Y. Zheng, Adv. Funct. Mater. 2020, 31; b) J. Shi, Y. Gao, X. Gao, Y. Zhang, J. Zhang, X. Jing, M. Shao, Adv Mater 2019, 31, e1901673; c) J. Liang, Z. Zhang, Y. Zheng, X. Wu, J. Wang, Z. Zhou, Y. Yang, Y. Huang, Z. Chen, C.-C. Chen, J. Mater. Chem. A 2021, 9, 11741; d) W. Fu, H. Liu, X. Shi, L. Zuo, X. Li, A. K. Y. Jen, Adv. Funct. Mater. 2019, 29; e) Y. Qin, H. Zhong, J. J. Intemann, S. Leng, M. Cui, C. Qin, M. Xiong, F. Liu, A. K. Y. Jen, K. Yao, Adv. Energy Mater. 2020, 10.

[74]   a) B.-E. Cohen, M. Wierzbowska, L. Etgar, Sustainable Energy Fuels 2017, 1, 1935; b) M. E. Kamminga, H.-H. Fang, M. R. Filip, F. Giustino, J. Baas, G. R. Blake, M. A. Loi, T. T. M. Palstra, Chem. Mater. 2016, 28, 4554.

[75]   A. H. Proppe, M. Wei, B. Chen, R. Quintero-Bermudez, S. O. Kelley, E. H. Sargent, J Am Chem Soc 2019, 141, 14180.

[76]   G. Yan, G. Sui, W. Chen, K. Su, Y. Feng, B. Zhang, Chem. Mater. 2022, 34, 3346.

[77]   a) H. Pan, X. Zhao, G. Xiu, H. Li, X. L. Zhang, G. Liang, Y. Shen, M. Wang, Nanoscale 2020, 12, 7330; b) X. Gan, W. Zhao, T. Xu, Y. Liang, L. Guo, H. Liu, J. Mater. Sci. 2021, 56, 17167.

[78]   a) D. B. Mitzi, C. D. Dimitrakopoulos, L. L. Kosbar, Chem. Mater. 2001, 13, 3728; b) Z. Xu, D. B. Mitzi, C. D. Dimitrakopoulos, K. R. Maxcy, Inorg. Chem. 2003, 42, 2031.

[79]   J. Hu, I. W. H. Oswald, H. Hu, S. J. Stuard, M. M. Nahid, L. Yan, Z. Chen, H. Ade, J. R. Neilson, W. You, ACS Mater. Lett. 2019, 1, 171.

[80]   J. V. Passarelli, C. M. Mauck, S. W. Winslow, C. F. Perkinson, J. C. Bard, H. Sai, K. W. Williams, A. Narayanan, D. J. Fairfield, M. P. Hendricks, W. A. Tisdale, S. I. Stupp, Nat Chem 2020, 12, 672.

[81]   Z. Chen, C. Zhang, X. F. Jiang, M. Liu, R. Xia, T. Shi, D. Chen, Q. Xue, Y. J. Zhao, S. Su, H. L. Yip, Y. Cao, Adv Mater 2017, 29.

[82]   J. Xi, I. Spanopoulos, K. Bang, J. Xu, H. Dong, Y. Yang, C. D. Malliakas, J. M. Hoffman, M. G. Kanatzidis, Z. Wu, J Am Chem Soc 2020, 142, 19705.

[83]   I. H. Park, L. Chu, K. Leng, Y. F. Choy, W. Liu, I. Abdelwahab, Z. Zhu, Z. Ma, W. Chen, Q. H. Xu, G. Eda, K. P. Loh, Adv. Funct. Mater. 2019, 29.

[84]   R. Sasai, H. Shinomura, J. Solid State Chem. 2013, 198, 452.

[85]   S. J. Yang, K. Wang, Y. Luo, J. Y. Park, H. Yang, A. H. Coffey, K. Ma, J. Sun, S. Wieghold, C. Zhu, L. Dou, ACS Energy Lett. 2023, 8, 3693.

[86]   H. Yao, Z. Li, C. Shi, Y. Xu, Q. Wang, Z. Li, G. Peng, Y. Lei, H. Wang, Z. Ci, Z. Jin, Adv. Funct. Mater. 2022, 32.

[87]   a) N. Wang, L. Cheng, R. Ge, S. Zhang, Y. Miao, W. Zou, C. Yi, Y. Sun, Y. Cao, R. Yang, Y. Wei, Q. Guo, Y. Ke, M. Yu, Y. Jin, Y. Liu, Q. Ding, D. Di, L. Yang, G. Xing, H. Tian, C. Jin, F. Gao, R. H. Friend, J. Wang, W. Huang, Nat. Photonics 2016, 10, 699; b) Z. Xu, D. Lu, F. Liu, H. Lai, X. Wan, X. Zhang, Y. Liu, Y. Chen, ACS Nano 2020, 14, 4871; c) T. Zhou, Z. Xu, R. Wang, X. Dong, Q. Fu, Y. Liu, Adv Mater 2022, 34, e2200705; d) C. Qin, T. Matsushima, W. J. Potscavage, A. S. D. Sandanayaka, M. R. Leyden, F. Bencheikh, K. Goushi, F. Mathevet, B. Heinrich, G. Yumoto, Y. Kanemitsu, C. Adachi, Nat. Photonics 2019, 14, 70.

[88]   K. Z. Du, Q. Tu, X. Zhang, Q. Han, J. Liu, S. Zauscher, D. B. Mitzi, Inorg Chem 2017, 56, 9291.

[89]   J. V. Passarelli, D. J. Fairfield, N. A. Sather, M. P. Hendricks, H. Sai, C. L. Stern, S. I. Stupp, J Am Chem Soc 2018, 140, 7313.

[90]   M. Braun, W. Tuffentsammer, H. Wachtel, H. C. Wolf, Chem. Phys. Lett. 1999, 307, 373.

[91]   W. T. M. Van Gompel, R. Herckens, K. Van Hecke, B. Ruttens, J. D'Haen, L. Lutsen, D. Vanderzande, Chem Commun (Camb) 2019, 55, 2481.

[92]   Q. Li, Y. Dong, G. Lv, T. Liu, D. Lu, N. Zheng, X. Dong, Z. Xu, Z. Xie, Y. Liu, ACS Energy Lett. 2021, 6, 2072.

[93]   Q. Fu, M. Chen, Q. Li, H. Liu, R. Wang, Y. Liu, J Am Chem Soc 2023, 145, 21687.

[94]   Y. Dong, D. Lu, Z. Xu, H. Lai, Y. Liu, Adv. Energy Mater. 2020, 10.

[95]   H. Lai, D. Lu, Z. Xu, N. Zheng, Z. Xie, Y. Liu, Adv Mater 2020, 32, e2001470.

[96]   C. Lermer, S. P. Harm, S. T. Birkhold, J. A. Jaser, C. M. Kutz, P. Mayer, L. Schmidt-Mende, B. V. Lotsch, Zeitschrift für anorganische und allgemeine Chemie 2016, 642, 1369.

[97]   G. Liu, H. Zheng, J. Ye, S. Xu, L. Zhang, H. Xu, Z. Liang, X. Chen, X. Pan, ACS Energy Lett. 2021, 6, 4395.

[98]   C. Liu, Z. Fang, J. Sun, Q. Lou, J. Ge, X. Chen, E. Zhou, M.-H. Shang, W. Yang, Z. Ge, ACS Energy Lett. 2020, 5, 3617.

[99]   R. Yang, R. Li, Y. Cao, Y. Wei, Y. Miao, W. L. Tan, X. Jiao, H. Chen, L. Zhang, Q. Chen, H. Zhang, W. Zou, Y. Wang, M. Yang, C. Yi, N. Wang, F. Gao, C. R. McNeill, T. Qin, J. Wang, W. Huang, Adv Mater 2018, 30, e1804771.

[100]   Y. Boeije, W. T. M. Van Gompel, Y. Zhang, P. Ghosh, S. J. Zelewski, A. Maufort, B. Roose, Z. Y. Ooi, R. Chowdhury, I. Devroey, S. Lenaers, A. Tew, L. Dai, K. Dey, H. Salway, R. H. Friend, H. Sirringhaus, L. Lutsen, D. Vanderzande, A. Rao, S. D. Stranks, J Am Chem Soc 2023, 145, 21330.

[101]   R. Herckens, W. T. M. Van Gompel, W. Song, M. C. Gélvez-Rueda, A. Maufort, B. Ruttens, J. D'Haen, F. C. Grozema, T. Aernouts, L. Lutsen, D. Vanderzande, J. Mater. Chem. A 2018, 6, 22899.

[102]   K. Jemli, P. Audebert, L. Galmiche, G. Trippe-Allard, D. Garrot, J. S. Lauret, E. Deleporte, ACS Appl Mater Interfaces 2015, 7, 21763.

[103]   R. Wang, X. Dong, Q. Ling, Z. Hu, Y. Gao, Y. Chen, Y. Liu, Angew Chem Int Ed Engl 2023, e202314690.

[104]   Y. Gao, E. Shi, S. Deng, S. B. Shiring, J. M. Snaider, C. Liang, B. Yuan, R. Song, S. M. Janke, A. Liebman-Pelaez, P. Yoo, M. Zeller, B. W. Boudouris, P. Liao, C. Zhu, V. Blum, Y. Yu, B. M. Savoie, L. Huang, L. Dou, Nat Chem 2019, 11, 1151.

[105]   Z. Wei, K. Wang, W. Zhao, Y. Gao, Q. Hu, K. Chen, L. Dou, Chem Commun (Camb) 2021, 57, 11469.

[106]   S. Nussbaum, E. Socie, L. Yao, J.-H. Yum, J.-E. Moser, K. Sivula, Chem. Mater. 2022, 34, 3798.

[107]   a) L. Min, W. Tian, F. Cao, J. Guo, L. Li, Adv Mater 2021, 33, e2101714; b) J. Qing, X.-K. Liu, M. Li, F. Liu, Z. Yuan, E. Tiukalova, Z. Yan, M. Duchamp, S. Chen, Y. Wang, S. Bai, J.-M. Liu, H. J. Snaith, C.-S. Lee, T. C. Sum, F. Gao, Adv. Energy Mater. 2018, 8.

[108]   D. Thrithamarassery Gangadharan, D. Ma, Energy Environ. Sci. 2019, 12, 2860.

[109]   I. C. Smith, E. T. Hoke, D. Solis-Ibarra, M. D. McGehee, H. I. Karunadasa, Angew Chem Int Ed Engl 2014, 53, 11232.

[110]   a) X. Lai, W. Li, X. Gu, H. Chen, Y. Zhang, G. Li, R. Zhang, D. Fan, F. He, N. Zheng, J. Yu, R. Chen, A. K. K. Kyaw, X. W. Sun, Chem. Eng. J. 2022, 427, 130949; b) J. Liang, Z. Zhang, Q. Xue, Y. Zheng, X. Wu, Y. Huang, X. Wang, C. Qin, Z. Chen, C.-C. Chen, Energy Environ. Sci. 2022, 15, 296.

[111]   Z. Lai, R. Dong, Q. Zhu, Y. Meng, F. Wang, F. Li, X. Bu, X. Kang, H. Zhang, Q. Quan, W. Wang, F. Wang, S. Yip, J. C. Ho, ACS Appl Mater Interfaces 2020, 12, 39567.

[112]   a) S. Liu, X. Guan, W. Xiao, R. Chen, J. Zhou, F. Ren, J. Wang, W. Chen, S. Li, L. Qiu, Y. Zhao, Z. Liu, W. Chen, Adv. Funct. Mater. 2022, 32; b) P. Vishnoi, J. L. Zuo, X. Li, D. C. Binwal, K. E. Wyckoff, L. Mao, L. Kautzsch, G. Wu, S. D. Wilson, M. G. Kanatzidis, R. Seshadri, A. K. Cheetham, J Am Chem Soc 2022, 144, 6661; c) L. Cheng, Z. Liu, S. Li, Y. Zhai, X. Wang, Z. Qiao, Q. Xu, K. Meng, Z. Zhu, G. Chen, Angew Chem Int Ed Engl 2021, 60, 856.

[113]   a) M. Safdari, P. H. Svensson, M. T. Hoang, I. Oh, L. Kloo, J. M. Gardner, J. Mater. Chem. A 2016, 4, 15638; b) B. Xiao, Q. Sun, S. Wang, L. Ji, Y. Li, S. Xi, B. B. Zhang, J. Wang, W. Jie, Y. Xu, J Phys Chem Lett 2022, 13, 1187.

[114]   a) Y. Liu, H. Zhou, Y. Ni, J. Guo, R. Lu, C. Li, X. Guo, Joule 2023, 7, 1016; b) B. Ma, J. Chen, M. Wang, X. Xu, J. Qian, Y. Lu, W. Zhang, P. Xia, M. Qin, W. Zhu, L. Zhang, S. Chen, X. Lu, W. Huang, The Journal of Physical Chemistry C 2020, 124, 16289; c) H. Wang, Z. Qin, J. Xie, S. Zhao, K. Liu, X. Guo, G. Li, X. Lu, K. Yan, J. Xu, Small 2020, 16, e2003098.

[115]   X. Li, J. Hoffman, W. Ke, M. Chen, H. Tsai, W. Nie, A. D. Mohite, M. Kepenekian, C. Katan, J. Even, M. R. Wasielewski, C. C. Stoumpos, M. G. Kanatzidis, J Am Chem Soc 2018, 140, 12226.

[116]   A. Lemmerer, D. G. Billing, CrystEngComm 2012, 14.

[117]   a) L. Mao, Y. Wu, C. C. Stoumpos, M. R. Wasielewski, M. G. Kanatzidis, J Am Chem Soc 2017, 139, 5210; b) W. Zhao, Q. Dong, J. Zhang, S. Wang, M. Chen, C. Zhao, M. Hu, S. Jin, N. P. Padture, Y. Shi, J. Mater. Chem. A 2020, 8, 9919.

[118]   E. R. Dohner, E. T. Hoke, H. I. Karunadasa, J Am Chem Soc 2014, 136, 1718.

[119]   Z. Xu, D. B. Mitzi, D. R. Medeiros, Inorg. Chem. 2003, 42, 1400.

[120]   D. Fu, J. Yuan, S. Wu, Y. Yao, X. Zhang, X.-M. Zhang, Inorg. Chem. Front. 2020, 7, 1394.

[121]   T. Zhao, C.-C. Chueh, Q. Chen, A. Rajagopal, A. K. Y. Jen, ACS Energy Lett. 2016, 1, 757.

[122]   a) N. Marchal, E. Mosconi, G. Garcia-Espejo, T. M. Almutairi, C. Quarti, D. Beljonne, F. De Angelis, J Phys Chem Lett 2021, 12, 2528; b) Q. Dai, H. Li, G. Sini, J. L. Bredas, Adv. Funct. Mater. 2021, 32.

[123]   a) L. Zhang, G. Qi, Y. Zhang, H. Wu, X. Xu, G. Zhou, H. Zhu, X. Li, G. Wu, H. Chen, Chem. Eng. J. 2023, 451; b) Z. Miao, Q. Cao, S. Peng, H. Zhu, F. Yuan, Y. Liang, T. Zhang, R. Zhao, P. Li, Y. Zhang, Y. Song, Adv. Funct. Mater. 2023.

[124]   a) L. Mao, P. Guo, M. Kepenekian, I. Spanopoulos, Y. He, C. Katan, J. Even, R. D. Schaller, R. Seshadri, C. C. Stoumpos, M. G. Kanatzidis, J Am Chem Soc 2020, 142, 8342; b) W. Ke, C. Chen, I. Spanopoulos, L. Mao, I. Hadar, X. Li, J. M. Hoffman, Z. Song, Y. Yan, M. G. Kanatzidis, J Am Chem Soc 2020, 142, 15049; c) D. Ghosh, D. Acharya, L. Pedesseau, C. Katan, J. Even, S. Tretiak, A. J. Neukirch, J. Mater. Chem. A 2020, 8, 22009.

[125]   W. Li, S. Sidhik, B. Traore, R. Asadpour, J. Hou, H. Zhang, A. Fehr, J. Essman, Y. Wang, J. M. Hoffman, I. Spanopoulos, J. J. Crochet, E. Tsai, J. Strzalka, C. Katan, M. A. Alam, M. G. Kanatzidis, J. Even, J. C. Blancon, A. D. Mohite, Nat Nanotechnol 2022, 17, 45.

[126]   A. Bonamartini Corradi, A. M. Ferrari, L. Righi, P. Sgarabotto, Inorg. Chem. 2001, 40, 218.

[127]   P. Liang-Chang, W. Zhen-Hong, Z. Xiu-Xiu, Y. Jiao-Jiao, C. Hu, Chin. J. Struct. Chem. 2019, 38, 1494.

[128]   X. Li, W. Ke, B. Traore, P. Guo, I. Hadar, M. Kepenekian, J. Even, C. Katan, C. C. Stoumpos, R. D. Schaller, M. G. Kanatzidis, J Am Chem Soc 2019, 141, 12880.

[129]   L. Gao, X. Li, B. Traoré, Y. Zhang, J. Fang, Y. Han, J. Even, C. Katan, K. Zhao, S. Liu, M. G. Kanatzidis, J. Am. Chem. Soc. 2021, 143, 12063.

[130]   D. Wang, S.-C. Chen, Q. Zheng, J. Mater. Chem. A 2021, 9, 11778.

[131]   M. P. Hautzinger, J. Dai, Y. Ji, Y. Fu, J. Chen, I. A. Guzei, J. C. Wright, Y. Li, S. Jin, Inorg Chem 2017, 56, 14991.

[132]   L. Wu, G. Li, K. Prashanthan, A. Musiienko, J. Li, T. W. Gries, H. Zhang, H. Kobler, P. Janasik, A. N. S. Appiah, G. Paramasivam, T. Sun, M. Li, D. Marongiu, M. Saba, A. Abate, Adv Mater 2023, e2304150.

[133]   Y. L. Lin, J. C. Johnson, J Phys Chem Lett 2021, 12, 4793.

[134]   R. Zhao, R. P. Sabatini, T. Zhu, S. Wang, A. Morteza Najjarian, A. Johnston, A. J. Lough, S. Hoogland, E. H. Sargent, D. S. Seferos, J. Am. Chem. Soc. 2021, 143, 19901.

[135]   H. Yu, Z. Wei, Y. Hao, Z. Liang, Z. Fu, H. Cai, New J. Chem. 2017, 41, 9586.

[136]   Y. Li, G. Zheng, C. Lin, J. Lin, Crystal Growth & Design 2008, 8, 1990.

[137]   L. Mao, H. Tsai, W. Nie, L. Ma, J. Im, C. C. Stoumpos, C. D. Malliakas, F. Hao, M. R. Wasielewski, A. D. Mohite, M. G. Kanatzidis, Chem. Mater. 2016, 28, 7781.

[138]   Z. Tang, J. Guan, A. M. Guloy, J. Mater. Chem. 2001, 11, 479.

[139]   I. Zimmermann, S. Aghazada, M. K. Nazeeruddin, Angew Chem Int Ed Engl 2019, 58, 1072.

[140]   Z. Xu, D. Lu, X. Dong, M. Chen, Q. Fu, Y. Liu, Adv Mater 2021, 33, e2105083.

[141]   Y. Dong, X. Dong, D. Lu, M. Chen, N. Zheng, R. Wang, Q. Li, Z. Xie, Y. Liu, Adv Mater 2023, 35, e2205258.

[142]   M. K. Jana, S. M. Janke, D. J. Dirkes, S. Dovletgeldi, C. Liu, X. Qin, K. Gundogdu, W. You, V. Blum, D. B. Mitzi, J Am Chem Soc 2019, 141, 7955.

[143]   X.-H. Zhu, N. Mercier, P. Frère, P. Blanchard, J. Roncali, M. Allain, C. Pasquier, A. Riou, Inorg. Chem. 2003, 42, 5330.

[144]   D. B. Mitzi, K. Chondroudis, C. R. Kagan, Inorg. Chem. 1999, 38, 6246.

[145]   C. Liu, Z. Fang, J. Sun, M. Shang, K. Zheng, W. Yang, Z. Ge, Nano Energy 2022, 93.

[146]   a) G. Wu, T. Liu, M. Hu, Z. Zhang, S. Li, L. Xiao, J. Guo, Y. Wang, A. Zhu, W. Li, H. Zhou, Y. Zhang, R. Chen, G. Xing, Adv Mater 2023, e2303061; b) X. Jiang, J. Zhang, S. Ahmad, D. Tu, X. Liu, G. Jia, X. Guo, C. Li, Nano Energy 2020, 75.

[147]   P. Huang, S. Kazim, M. Wang, S. Ahmad, ACS Energy Lett. 2019, 4, 2960.

[148]   D. B. Straus, C. R. Kagan, J Phys Chem Lett 2018, 9, 1434.

[149]   a) J. Gong, M. Hao, Y. Zhang, M. Liu, Y. Zhou, Angew. Chem. Int. Ed. 2022, 61, e202112022; b) N. Fathalizadeh, S. Shojaei, S. Ahmadi-Kandjani, Opt. Quantum Electron. 2023, 55; c) H. Xiang, P. Liu, R. Ran, W. Wang, W. Zhou, Z. Shao, Renewable Sustainable Energy Rev. 2022, 166.

[150]   C. M. M. Soe, C. C. Stoumpos, M. Kepenekian, B. Traoré, H. Tsai, W. Nie, B. Wang, C. Katan, R. Seshadri, A. D. Mohite, J. Even, T. J. Marks, M. G. Kanatzidis, J. Am. Chem. Soc. 2017, 139, 16297.

[151]   a) P.-P. Sun, X. Zhang, S. Yuan, W. Chi, G. Cai, Sol. RRL 2023, 7, 2300441; b) P. Yan, W. Zhang, C. Wang, Z. Wu, M. Zhu, H. Li, C. Sheng, J. Alloys Compd. 2024, 977, 173298; c) P. Li, C. Liang, X.-L. Liu, F. Li, Y. Zhang, X.-T. Liu, H. Gu, X. Hu, G. Xing, X. Tao, Y. Song, Adv. Mater. 2019, 31, 1901966.

[152]   J. Yang, T. Yang, D. Liu, Y. Zhang, T. Luo, J. Lu, J. Fang, J. Wen, Z. Deng, S. Liu, L. Chen, K. Zhao, Sol. RRL 2021, 5, 2100286.

[153]   Y. Zhang, J. Chen, X. Lian, M. Qin, J. Li, T. R. Andersen, X. Lu, G. Wu, H. Li, H. Chen, Small Methods 2019, 3, 1900375.

[154]   Z. Lu, X. Xu, Y. Gao, Z. Wu, A. Li, Z. Zhan, Y. Qu, Y. Cai, X. Huang, J. Huang, Z. Zhang, T. Luo, L. Peng, P. Liu, T. Shi, W. Xie, Surf. Interfaces 2022, 34, 102343.

[155]   F. Arabpour Roghabadi, M. Alidaei, S. M. Mousavi, T. Ashjari, A. S. Tehrani, V. Ahmadi, S. M. Sadrameli, J. Mater. Chem. A 2019, 7, 5898.

[156]   Q. Cheng, B. Wang, G. Huang, Y. Li, X. Li, J. Chen, S. Yue, K. Li, H. Zhang, Y. Zhang, H. Zhou, Angew Chem Int Ed Engl 2022, 61, e202208264.

[157]   A. M. Ulatowski, K. A. Elmestekawy, J. B. Patel, N. K. Noel, S. Yan, H. Kraus, P. G. Huggard, M. B. Johnston, L. M. Herz, Adv. Funct. Mater. 2023, 33, 2305283.

[158]   I. Metcalf, S. Sidhik, H. Zhang, A. Agrawal, J. Persaud, J. Hou, J. Even, A. D. Mohite, Chem. Rev. 2023, 123, 9565.

[159]   D. Gui, L. Ji, A. Muhammad, W. Li, W. Cai, Y. Li, X. Li, X. Wu, P. Lu, J Phys Chem Lett 2018, 9, 751.

[160]   a) L. Gao, F. Zhang, C. Xiao, X. Chen, B. W. Larson, J. J. Berry, K. Zhu, Adv. Funct. Mater. 2019, 29, 1901652; b) H. Tsai, W. Nie, J. C. Blancon, C. C. Stoumpos, R. Asadpour, B.

Harutyunyan, A. J. Neukirch, R. Verduzco, J. J. Crochet, S. Tretiak, L. Pedesseau, J. Even, M. A. Alam, G. Gupta, J. Lou, P. M. Ajayan, M. J. Bedzyk, M. G. Kanatzidis, Nature 2016, 536, 312.

[161]   a) E. Lafalce, E. Amerling, Z. G. Yu, P. C. Sercel, L. Whittaker-Brooks, Z. V. Vardeny, Nat Commun 2022, 13, 483; b) Y. Zhai, S. Baniya, C. Zhang, J. Li, P. Haney, C.-X. Sheng, E. Ehrenfreund, Z. V. Vardeny, Sci. Adv. 2017, 3, e1700704; c) I. H. Park, Q. Zhang, K. C. Kwon, Z. Zhu, W. Yu, K. Leng, D. Giovanni, H. S. Choi, I. Abdelwahab, Q. H. Xu, T. C. Sum, K. P. Loh, J Am Chem Soc 2019, 141, 15972.

[162]   I. W. H. Oswald, A. A. Koegel, J. R. Neilson, Chem. Mater. 2018, 30, 8606.

[163]   D. G. Billing, A. Lemmerer, Acta Crystallogr B 2007, 63, 735.

[164]   N. Mercier, CrystEngComm 2005, 7.

[165]   D. G. Billing, Acta Crystallogr., Sect. E: Struct. Rep. Online 2002, 58, m669.

[166]   T. Schmitt, S. Bourelle, N. Tye, G. Soavi, A. D. Bond, S. Feldmann, B. Traore, C. Katan, J. Even, S. E. Dutton, F. Deschler, J Am Chem Soc 2020, 142, 5060.

[167]   D. B. Straus, N. Iotov, M. R. Gau, Q. Zhao, P. J. Carroll, C. R. Kagan, J Phys Chem Lett 2019, 10, 1198.

[168]   H. Pan, X. Zhao, X. Gong, Y. Shen, M. Wang, J Phys Chem Lett 2019, 10, 1813.

[169]   D. B. Straus, S. Hurtado Parra, N. Iotov, Q. Zhao, M. R. Gau, P. J. Carroll, J. M. Kikkawa, C. R. Kagan, ACS Nano 2020, 14, 3621.

[170]   J. H. Fan, Y. Qin, M. Azeem, Z. Z. Zhang, Z. G. Li, N. Sun, Z. Q. Yao, W. Li, Dalton Trans 2021, 50, 2648.

[171]   X. H. Zhu, N. Mercier, A. Riou, P. Blanchard, P. Frere, Chem Commun (Camb) 2002, 2160.

[172]   K. Wang, L. Jin, Y. Gao, A. Liang, B. P. Finkenauer, W. Zhao, Z. Wei, C. Zhu, T. F. Guo, L. Huang, L. Dou, ACS Nano 2021, 15, 6316.

[173]   M. K. Rayner, D. G. Billing, Acta Crystallogr Sect E Struct Rep Online 2010, 66, 660.

[174]   K. Xu, L. He, Y. Z. Wang, X. Meng, P. P. Shi, Q. Ye, Inorg Chem 2021, 60, 10642.

[175]   A. Ummadisingu, A. Mishra, D. J. Kubicki, T. LaGrange, A. Ducinskas, M. Siczek, W. Bury, J. V. Milic, M. Gratzel, L. Emsley, Small 2022, 18, e2104287.

[176]   C. Lermer, A. Senocrate, I. Moudrakovski, T. Seewald, A.-K. Hatz, P. Mayer, F. Pielnhofer, J. A. Jaser, L. Schmidt-Mende, J. Maier, B. V. Lotsch, Chem. Mater. 2018, 30, 6289.

[177]   E. Amerling, H. Lu, B. W. Larson, A. E. Maughan, A. Phillips, E. Lafalce, L. Whittaker-Brooks, J. J. Berry, M. C. Beard, Z. V. Vardeny, J. L. Blackburn, ACS Energy Lett. 2021, 6, 1104.

[178]   F. Zhang, D. H. Kim, H. Lu, J. S. Park, B. W. Larson, J. Hu, L. Gao, C. Xiao, O. G. Reid, X. Chen, Q. Zhao, P. F. Ndione, J. J. Berry, W. You, A. Walsh, M. C. Beard, K. Zhu, J Am Chem Soc 2019, 141, 5972.

[179]   R. L. Milot, R. J. Sutton, G. E. Eperon, A. A. Haghighirad, J. Martinez Hardigree, L. Miranda, H. J. Snaith, M. B. Johnston, L. M. Herz, Nano Lett. 2016, 16, 7001.

[180]   X. Chen, H. Lu, K. Wang, Y. Zhai, V. Lunin, P. C. Sercel, M. C. Beard, J. Am. Chem. Soc. 2021, 143, 19438.

[181]   a) Y. Gao, M. Zhang, X. Zhang, G. Lu, The Journal of Physical Chemistry Letters 2019, 10, 3820; b) D. Feldstein, R. Perea-Causín, S. Wang, M. Dyksik, K. Watanabe, T. Taniguchi, P. Plochocka, E. Malic, The Journal of Physical Chemistry Letters 2020, 11, 9975.

[182]   O. Yaffe, A. Chernikov, Z. M. Norman, Y. Zhong, A. Velauthapillai, A. van der Zande, J. S. Owen, T. F. Heinz, Physical Review B 2015, 92, 045414.

[183]   M. C. Gélvez-Rueda, M. B. Fridriksson, R. K. Dubey, W. F. Jager, W. van der Stam, F. C. Grozema, Nat. Commun. 2020, 11, 1901.

[184]   J. C. Blancon, A. V. Stier, H. Tsai, W. Nie, C. C. Stoumpos, B. Traoré, L. Pedesseau, M. Kepenekian, F. Katsutani, G. T. Noe, J. Kono, S. Tretiak, S. A. Crooker, C. Katan, M. G. Kanatzidis, J. J. Crochet, J. Even, A. D. Mohite, Nat. Commun. 2018, 9, 2254.

[185]   H. Zhang, R. Wang, L. Yang, Z. Hu, H. Liu, Y. Liu, Angew Chem Int Ed Engl 2024, e202318206.

[186]   Y. Wu, B. Chang, L. Wang, H. Li, L. Pan, Z. Liu, L. Yin, Adv Mater 2023, 35, e2300174.

[187]   a) J. Yin, P. Maity, R. Naphade, B. Cheng, J.-H. He, O. M. Bakr, J.-L. Brédas, O. F. Mohammed, ACS Nano 2019, 13, 12621; b) R. Chakraborty, A. Nag, The Journal of Physical Chemistry C 2020, 124, 16177.

[188]   A. D. Belogur, D. A. Baghdasaryan, I. V. Iorsh, I. A. Shelykh, V. Shahnazaryan, Phys. Rev. Appl. 2022, 17, 044048.

[189]   M. Xia, Z. Xie, H. Wang, T. Jin, L. Liu, J. Kang, Z. Sang, X. Yan, B. Wu, H. Hu, J. Tang, G. Niu, Adv. Mater. 2023, 35, 2211769.

[190]   J.-T. Lin, C.-C. Liao, C.-S. Hsu, D.-G. Chen, H.-M. Chen, M.-K. Tsai, P.-T. Chou, C.-W. Chiu, J. Am. Chem. Soc. 2019, 141, 10324.

[191]   J. Quan, S. Yu, B. Xing, X. He, L. Zhang, Phys. Rev. Mater. 2022, 6, 065405.

[192]   E. A. Muljarov, S. G. Tikhodeev, N. A. Gippius, T. Ishihara, Physical Review B 1995, 51, 14370.

[193]   R. Zheng, X. Gan, K. Li, S. Zhang, M. Xiang, L. Guo, H. Liu, Opt. Mater. 2024, 147, 114566.

[194]   B. Cheng, T.-Y. Li, P. Maity, P.-C. Wei, D. Nordlund, K.-T. Ho, D.-H. Lien, C.-H. Lin, R.-Z. Liang, X. Miao, I. A. Ajia, J. Yin, D. Sokaras, A. Javey, I. S. Roqan, O. F. Mohammed, J.-H. He, Commun. Phys. 2018, 1, 80.

[195]   X. Zhu, Z. Xu, S. Zuo, J. Feng, Z. Wang, X. Zhang, K. Zhao, J. Zhang, H. Liu, S. Priya, S. F. Liu, D. Yang, Energy Environ. Sci. 2018, 11, 3349.

[196]   a) P. Darman, A. Yaghoobi, S. Darbari, Pin hole free 2D Ruddlesden-Popper Perovskite layer with closed packed large crystalline grains, suitable for fast response and high sensitive MSM photodetection, 2023; b) L. Pedesseau, M. Kepenekian, D. Sapori, Y. Huang, A. Rolland, A. Beck, C. Cornet, O. Durand, S. Wang, C. Katan, J. Even, Dielectric properties of hybrid perovskites and drift-diffusion modeling of perovskite cells, Vol. 9743, SPIE, 2016; c) D. Sapori, M. Kepenekian, L. Pedesseau, C. Katan, J. Even, Nanoscale 2016, 8, 6369; d) C. C. Stoumpos, C. M. M. Soe, H. Tsai, W. Nie, J.-C. Blancon, D. H. Cao, F. Liu, B. Traoré, C. Katan, J. Even, A. D. Mohite, M. G. Kanatzidis, Chem 2017, 2, 427.

[197]   H. Zahra, A. Hichri, S. Jaziri, 2017.

[198]   B. Traore, L. Pedesseau, L. Assam, X. Che, J.-C. Blancon, H. Tsai, W. Nie, C. C. Stoumpos, M. G. Kanatzidis, S. Tretiak, A. D. Mohite, J. Even, M. Kepenekian, C. Katan, ACS Nano 2018, 12, 3321.

[199]   B. Liu, C. M. M. Soe, C. C. Stoumpos, W. Nie, H. Tsai, K. Lim, A. D. Mohite, M. G. Kanatzidis, T. J. Marks, K. D. Singer, Sol. RRL 2017, 1, 1700062.

[200]   K. Shibuya, M. Koshimizu, Y. Takeoka, K. Asai, Nucl. Instrum. Methods Phys. Res., Sect. B 2002, 194, 207.

[201]   M. D. Smith, L. Pedesseau, M. Kepenekian, I. C. Smith, C. Katan, J. Even, H. I. Karunadasa, Chem. Sci. 2017, 8, 1960.

[202]   L. Pedesseau, D. Sapori, B. Traore, R. Robles, H.-H. Fang, M. A. Loi, H. Tsai, W. Nie, J.-C. Blancon, A. Neukirch, S. Tretiak, A. D. Mohite, C. Katan, J. Even, M. Kepenekian, ACS Nano 2016, 10, 9776.

[203]   X. Hong, T. Ishihara, A. V. Nurmikko, Physical Review B 1992, 45, 6961.

[204]   T. He, S. Li, Y. Jiang, C. Qin, M. Cui, L. Qiao, H. Xu, J. Yang, R. Long, H. Wang, M. Yuan, Nat. Commun. 2020, 11, 1672.

[205]   C. Katan, N. Mercier, J. Even, Chem Rev 2019, 119, 3140.

[206]   X. Zhang, G. Wu, W. Fu, M. Qin, W. Yang, J. Yan, Z. Zhang, X. Lu, H. Chen, Adv. Energy Mater. 2018, 8.

[207]   C. Ma, D. Shen, T.-W. Ng, M.-F. Lo, C.-S. Lee, Adv. Mater. 2018, 30, 1800710.

[208] E. A. Duijnstee, J. M. Ball, V. M. Le Corre, L. J. A. Koster, H. J. Snaith, J. Lim, ACS Energy Lett. 2020, 5, 376.

[209] F. Yao, Q. Lin, ACS Photonics 2022, 9, 3165.

[210] S. G. Motti, M. Kober‑Czerny, M. Righetto, P. Holzhey, J. Smith, H. Kraus, H. J. Snaith, M. B. Johnston, L. M. Herz, Adv. Funct. Mater. 2023, 33.

[211] J. C. Blakesley, F. A. Castro, W. Kylberg, G. F. A. Dibb, C. Arantes, R. Valaski, M. Cremona, J. S. Kim, J.-S. Kim, Org. Electron. 2014, 15, 1263.

[212] a) M. Sajedi Alvar, P. W. M. Blom, G. A. H. Wetzelaer, Nat Commun 2020, 11, 4023; b) V. M. Le Corre, E. A. Duijnstee, O. El Tambouli, J. M. Ball, H. J. Snaith, J. Lim, L. J. A. Koster, ACS Energy Lett 2021, 6, 1087.

[213] Y. Zhang, M. Sun, N. Zhou, B. Huang, H. Zhou, J Phys Chem Lett 2020, 11, 7610.

[214] C. Li, J. Yang, F. Su, J. Tan, Y. Luo, S. Ye, Nat Commun 2020, 11, 5481.

[215] L. Zhang, G. Qi, Y. Zhang, H. Wu, X. Xu, G. Zhou, H. Zhu, X. Li, G. Wu, H. Chen, Chem. Eng. J. 2023, 451, 138654.

[216] C. S. Ponseca, Jr., T. J. Savenije, M. Abdellah, K. Zheng, A. Yartsev, T. Pascher, T. Harlang, P. Chabera, T. Pullerits, A. Stepanov, J.-P. Wolf, V. Sundström, J. Am. Chem. Soc. 2014, 136, 5189.

[217] R. L. Milot, G. E. Eperon, H. J. Snaith, M. B. Johnston, L. M. Herz, Adv. Funct. Mater. 2015, 25, 6218.

[218] Y. Song, W. Bi, A. Wang, X. Liu, Y. Kang, Q. Dong, Nat. Commun. 2020, 11, 274.

[219] M. Bari, H. Wu, A. A. Bokov, R. F. Ali, H. N. Tailor, B. D. Gates, Z.-G. Ye, CrystEngComm 2021, 23, 3326.

[220] M. I. Saidaminov, A. L. Abdelhady, B. Murali, E. Alarousu, V. M. Burlakov, W. Peng, I. Dursun, L. Wang, Y. He, G. Maculan, A. Goriely, T. Wu, O. F. Mohammed, O. M. Bakr, Nat. Commun. 2015, 6, 7586.

[221] A. Shpatz Dayan, L. Etgar, ACS Appl. Energy Mater. 2023, 6, 11005.

[222] W. Rehman, R. L. Milot, G. E. Eperon, C. Wehrenfennig, J. L. Boland, H. J. Snaith, M. B. Johnston, L. M. Herz, Adv. Mater. 2015, 27, 7938.

[223] A. A. Zhumekenov, M. I. Saidaminov, M. A. Haque, E. Alarousu, S. P. Sarmah, B. Murali, I. Dursun, X.-H. Miao, A. L. Abdelhady, T. Wu, O. F. Mohammed, O. M. Bakr, ACS Energy Lett. 2016, 1, 32.

[224] Q. Han, S.-H. Bae, P. Sun, Y.-T. Hsieh, Y. Yang, Y. S. Rim, H. Zhao, Q. Chen, W. Shi, G. Li, Y. Yang, Adv. Mater. 2016, 28, 2253.

[225] K. Wang, C. Wu, D. Yang, Y. Jiang, S. Priya, ACS Nano 2018, 12, 4919.

[226] C. Li, J. Yang, F. Su, J. Tan, Y. Luo, S. Ye, Nat. Commun. 2020, 11, 5481.

[227] F. Zhang, D. H. Kim, H. Lu, J.-S. Park, B. W. Larson, J. Hu, L. Gao, C. Xiao, O. G. Reid, X. Chen, Q. Zhao, P. F. Ndione, J. J. Berry, W. You, A. Walsh, M. C. Beard, K. Zhu, J. Am. Chem. Soc. 2019, 141, 5972.

[228] A. Burgos-Caminal, E. Socie, M. E. F. Bouduban, J.-E. Moser, The Journal of Physical Chemistry Letters 2020, 11, 7692.

[229] Y. Shen, Y. Liu, H. Ye, Y. Zheng, Q. Wei, Y. Xia, Y. Chen, K. Zhao, W. Huang, S. Liu, Angew. Chem. Int. Ed. 2020, 59, 14896.

[230] N. Liu, P. Liu, H. Zhou, Y. Bai, Q. Chen, The Journal of Physical Chemistry Letters 2020, 11, 3521.

[231] N. Liu, P. Liu, H. Ren, H. Xie, N. Zhou, Y. Gao, Y. Li, H. Zhou, Y. Bai, Q. Chen, ACS Appl. Mater. Interfaces 2020, 12, 3127.

[232] Y. Chen, Y. Sun, J. Peng, W. Zhang, X. Su, K. Zheng, T. Pullerits, Z. Liang, Adv. Energy Mater. 2017, 7, 1700162.

[233] Y. Zhang, M. Sun, N. Zhou, B. Huang, H. Zhou, The Journal of Physical Chemistry Letters 2020, 11, 7610.

[234] T. Huang, Z. Zhu, C. Zhao, W. Kong, X. Chen, R. Li, Z. Yu, Z. Shi, D. Li, B. Yang, W. Yu, J. Mater. Chem. A 2022, 10, 21044.

[235] Y. Yang, C. Liu, O. A. Syzgantseva, M. A. Syzgantseva, S. Ma, Y. Ding, M. Cai, X. Liu, S. Dai, M. K. Nazeeruddin, Adv. Energy Mater. 2021, 11, 2002966.

[236] Y. Fu, X. Jiang, X. Li, B. Traore, I. Spanopoulos, C. Katan, J. Even, M. G. Kanatzidis, E. Harel, J. Am. Chem. Soc. 2020, 142, 4008.

[237] Z. Gozukara Karabag, A. Karabag, U. Gunes, X. X. Gao, O. A. Syzgantseva, M. A. Syzgantseva, F. Varlioglu Yaylali, N. Shibayama, H. Kanda, A. I. Rafieh, R. C. Turnell‑Ritson, P. J. Dyson, S. Yerci, M. K. Nazeeruddin, G. Gunbas, Adv. Energy Mater. 2023, 13.

[238] L. Gan, J. Li, Z. Fang, H. He, Z. Ye, J Phys Chem Lett 2017, 8, 5177.

[239] F. Li, Y. Xie, Y. Hu, M. Long, Y. Zhang, J. Xu, M. Qin, X. Lu, M. Liu, ACS Energy Lett. 2020, 5, 1422.

[240] F. Zeng, W. Kong, Y. Liang, F. Li, Y. Lvtao, Z. Su, T. Wang, B. Peng, L. Ye, Z. Chen, X. Gao, J. Huang, R. Zheng, X. Yang, Adv Mater 2023, e2306051.

[241] W. Paritmongkol, N. S. Dahod, A. Stollmann, N. Mao, C. Settens, S.-L. Zheng, W. A. Tisdale, Chem. Mater. 2019, 31, 5592.

[242] F. Hao, C. C. Stoumpos, R. P. Chang, M. G. Kanatzidis, J Am Chem Soc 2014, 136, 8094.

[243]   P. Cheng, T. Wu, J. Liu, W. Q. Deng, K. Han, J Phys Chem Lett 2018, 9, 2518.

[244]   F. Wang, M. G. Ju, L. Ma, Mater. Today Phys. 2022, 27.

[245]   L. Mao, Y. Wu, C. C. Stoumpos, B. Traore, C. Katan, J. Even, M. R. Wasielewski, M. G. Kanatzidis, J Am Chem Soc 2017, 139, 11956.

[246]   A. Yangui, S. Pillet, A. Lusson, E.-E. Bendeif, S. Triki, Y. Abid, K. Boukheddaden, J. Alloys Compd. 2017, 699, 1122.

[247]   X. Li, P. Guo, M. Kepenekian, I. Hadar, C. Katan, J. Even, C. C. Stoumpos, R. D. Schaller, M. G. Kanatzidis, Chem. Mater. 2019, 31, 3582.

[248]   a) W. Guo, Z. Yang, J. Dang, M. Wang, Nano Energy 2021, 86; b) G. Grancini, M. K. Nazeeruddin, Nat. Rev. Mater. 2018, 4, 4.

[249]   E. S. Vasileiadou, B. Wang, I. Spanopoulos, I. Hadar, A. Navrotsky, M. G. Kanatzidis, J Am Chem Soc 2021, 143, 2523.

[250]   S. Wang, Y. Liu, J. Zou, J. Jin, Y. Jiang, T. Zeng, W. Zhao, R.-X. He, B. Chen, Y. Chen, S. Jin, H.-X. Li, Z. Xie, C.-A. Wang, W. Sun, Q. Cao, X.-Z. Zhao, InfoMat 2023, 5, e12396.

[251]   M. P. Hautzinger, D. Pan, A. K. Pigg, Y. Fu, D. J. Morrow, M. Leng, M.-Y. Kuo, N. Spitha, D. P. Lafayette, D. D. Kohler, J. C. Wright, S. Jin, ACS Energy Lett. 2020, 5, 1430.

[252]   W. Ke, L. Mao, C. C. Stoumpos, J. Hoffman, I. Spanopoulos, A. D. Mohite, M. G. Kanatzidis, Adv. Energy Mater. 2019, 9.

[253]   O. Nazarenko, M. R. Kotyrba, S. Yakunin, M. Aebli, G. Rainò, B. M. Benin, M. Wörle, M. V. Kovalenko, J. Am. Chem. Soc. 2018, 140, 3850.

[254]   N. Zhou, Y. Shen, L. Li, S. Tan, N. Liu, G. Zheng, Q. Chen, H. Zhou, J Am Chem Soc 2018, 140, 459.

[255]   a) L. M. Herz, ACS Energy Lett. 2017, 2, 1539; b) C. Ran, J. Xu, W. Gao, C. Huang, S. Dou, Chem Soc Rev 2018, 47, 4581.

[256]   a) X. Jiang, J. Zhang, S. Ahmad, D. Tu, X. Liu, G. Jia, X. Guo, C. Li, Nano Energy 2020, 75, 104892; b) P. Chen, Y. Bai, S. Wang, M. Lyu, J.-H. Yun, L. Wang, Adv. Funct. Mater. 2018, 28, 1706923; c) A. A. Sutanto, P. Caprioglio, N. Drigo, Y. J. Hofstetter, I. Garcia-Benito, V. I. E. Queloz, D. Neher, M. K. Nazeeruddin, M. Stolterfoht, Y. Vaynzof, G. Grancini, Chem 2021, 7, 1903; d) Q. Yao, Q. Xue, Z. Li, K. Zhang, T. Zhang, N. Li, S. Yang, C. J. Brabec, H.-L. Yip, Y. Cao, Adv. Mater. 2020, 32, 2000571; e) J. Tong, Z. Song, D. H. Kim, X. Chen, C. Chen, A. F. Palmstrom, P. F. Ndione, M. O. Reese, S. P. Dunfield, O. G. Reid, J. Liu, F. Zhang, S. P. Harvey, Z. Li, S. T. Christensen, G. Teeter, D. Zhao, M. M. Al-Jassim, M. F. A. M. van Hest, M. C. Beard, S. E. Shaheen, J. J. Berry, Y. Yan, K. Zhu, Science 2019, 364, 475.

[257] a) G. Grancini, C. Roldán-Carmona, I. Zimmermann, E. Mosconi, X. Lee, D. Martineau, S. Narbey, F. Oswald, F. De Angelis, M. Graetzel, M. K. Nazeeruddin, Nat. Commun. 2017, 8, 15684; b) G. Uzurano, N. Kuwahara, T. Saito, A. Fujii, M. Ozaki, ACS Mater. Lett. 2022, 4, 378.

[258] J. Tong, Q. Jiang, A. J. Ferguson, A. F. Palmstrom, X. Wang, J. Hao, S. P. Dunfield, A. E. Louks, S. P. Harvey, C. Li, H. Lu, R. M. France, S. A. Johnson, F. Zhang, M. Yang, J. F. Geisz, M. D. McGehee, M. C. Beard, Y. Yan, D. Kuciauskas, J. J. Berry, K. Zhu, Nat. Energy 2022, 7, 642.

[259] a) L. Cheng, T. Jiang, Y. Cao, C. Yi, N. Wang, W. Huang, J. Wang, Adv. Mater. 2020, 32, 1904163; b) Y. Fu, D. Zhang, H. Zhan, C. Zhao, Y. Cheng, C. Qin, L. Wang, The Journal of Physical Chemistry Letters 2021, 12, 11645.

[260] F. Zhang, B. Cai, J. Song, B. Han, B. Zhang, H. Zeng, Adv. Funct. Mater. 2020, 30, 2001732.

[261] Y. Pan, H. Wang, X. Li, X. Zhang, F. Liu, M. Peng, Z. Shi, C. Li, H. Zhang, Z. Weng, M. Gusain, H. Long, D. Li, J. Wang, Y. Zhan, L. Zheng, J. Mater. Chem. C 2020, 8, 3359.

[262] J. Li, J. Wang, J. Ma, H. Shen, L. Li, X. Duan, D. Li, Nat. Commun. 2019, 10, 806.

Yixin Zhang is a Master's student in applied chemistry under the supervision of Prof. Fei Zhang at Tianjin University. He received his Bachelor's degree from the School of Chemical Engineering and Technology at Tianjin University in 2022. His current research focuses on the charge transport properties of 2D perovskites.

Mojtaba Abdi-Jalebi is an Associate Professor in Energy Materials at the Institute for Materials Discovery, the Mathematical and Physical Sciences faculty at the University College London (UCL). He received his BSc (2012) at Sharif University of Technology, MSc (2014) at École Polytechnique Fédérale de Lausanne (EPFL), and Ph. D. degree (2018) at Cavendish Laboratory, University of Cambridge. From 2018 to 2020, he served as a Junior Research Fellow at Cambridge University and Wolfson College. He currently focuses on emerging semiconductors' material and electronic properties, including halide perovskites, small molecules, and organic semiconductors for optoelectronic and electrochemical devices.

Bryon W. Larson is a Principal Scientist at the National Renewable Energy Laboratory. After his earning a PhD in inorganic chemistry from Colorado State University (2013), he worked as a postdoctoral researcher with Nikos Kopidakis at NREL, and joined NREL's staff in 2016.

Currently, he leads efforts to study charge-carrier generation, transport, and decay dynamics in emergent PV materials, including organic semiconductors, perovskites, and novel composites using a broad range of contactless and electrode-based spectroscopies under steady-state and transient conditions. His work extends to solution processed PV technology development, including lab-to-fab device design, scalable printing techniques, and laser-interconnected module fabrication.

Fei Zhang is a Professor at the School of Chemical Engineering and Technology at Tianjin University. He received his B.Eng. (2011) and Ph. D. degree (2017) under the supervision of Prof. Shirong Wang at Tianjin University. He was a visiting Ph.D. student in LPI at Ecole Polytechnique Fédérale de Lausanne (EPFL) under Prof. Michael Grätzel and Dr. Shaik Mohammed Zakeeruddin (2015–2017). Then, he worked as a postdoctoral researcher at the Chemistry and Nanoscience Center at the National Renewable Energy Laboratory under Dr. Kai Zhu's supervision (2017–2021). His interests concentrate on synthesizing low-dimensional perovskites, hole-transporting materials, and device engineering for perovskite optoelectrical devices.

This review first delves into a holistic analysis of the factors influencing the charge transport properties of 2D perovskites from four key aspects. It then consolidates and compares the standard transport testing methods for 2D perovskites, followed by exploring measures to enhance charge transport properties from a compositional approach.

Yixin Zhang, Mojtaba Abdi-Jalebi, Bryon W. Larson [*], Fei Zhang [*]

What Matters for the Charge Transport of Two-Dimensional Perovskites?